
THE AMPLITUDE DESCRIPTION OF
NONEQUILIBRIUM PATTERNS

Martin van Hecke



THE AMPLITUDE DESCRIPTION OF
NONEQUILIBRIUM PATTERNS

Proefschrift

ter verkrijging van de graad van Doctor
aan de Rijksuniversiteit te Leiden,
op gezag van de Rector Magnificus Dr. L. Leertouwer,
hoogleraar in de faculteit der Godgeleerdheid,
volgens besluit van het College van Dekanen
te verdedigen op dinsdag 3 september 1996
te klokke 16.15 uur

door

Martinus Leonardus van Hecke

geboren te Amsterdam op 18 juni 1967

Kast dissertaties

Promotiecommissie:

Promotor: Prof.dr. ir. W. van Saarloos
Referent: Prof.dr. ir. L. A. Peletier
Overige leden: Prof.dr. P. J. van Baal
Dr. T. Bohr (NBI)
Prof.dr. H. W. Capel (UVA)
Prof.dr. L. J. de Jongh
Prof.dr. J. M. J. van Leeuwen
Dr. W. van de Water (TUE)

Contents

1	Introduction.	5
1.1	Perspective.	5
1.2	Patterns.	7
1.2.1	The Rayleigh-Bénard instability.	8
1.3	Linear analysis.	10
1.3.1	Bifurcations.	12
1.4	Amplitude equations.	13
1.4.1	Comparison between the RGLE and CGLE.	19
1.4.2	Convective and absolute instabilities.	20
1.5	Phase winding solutions and secondary instabilities.	21
1.6	Beyond the phase-winding solutions.	23
1.6.1	Coherent structures.	25
1.6.2	Spatio-temporal chaos.	26
1.7	The validity of the amplitude approach.	28
2	Rayleigh-Bénard convection in a rotating annulus.	31
2.1	Introduction.	31
2.2	Equations of motion.	33
2.3	Linear stability analysis.	36
2.4	Amplitude expansion.	42
2.4.1	The adjoint solution.	46
2.4.2	Calculation of u_1 .	47
2.5	Results.	49
2.5.1	Stationary bifurcation.	50
2.5.2	The role of the Prandtl number.	51
2.5.3	Prandtl number $\sigma = 6.7$.	54
2.5.4	Prandtl number $\sigma = 0.15$.	57
2.6	Conclusion.	60
3	A domain-wall between single-mode and bimodal states.	63
3.1	Introduction.	63
3.2	The variational case.	65
3.3	The NLDE's with the group-velocity.	68
3.3.1	Phase-space analysis.	69
3.3.2	Numerical simulations.	74
3.4	The RGLE's with the group-velocity.	79
3.5	The CGLE's.	83
3.5.1	The case $c_2 = c_3$.	84

3.5.2	The case $c_2 \neq c_3$.	84
3.6	Conclusion and outlook.	87
4	The interactions between pulses and fronts.	89
4.1	Convection in binary liquids.	89
4.2	Pulses.	90
4.3	Fronts.	91
4.4	Coherent and incoherent drifting pulse dynamics.	93
4.5	Conclusion.	98
	Conclusion and outlook	99
	References	101
	Samenvatting	105
	List of publications	109
	Curriculum Vitae	111

1 Introduction.

1.1 Perspective.

Nature generates a bewildering variety of patterns. Consider for instance the formation of ripples in the sand on the beach [1], the flickering of a flame [2], the motion of milk in a milk-pan that is heated from below [3] or growth patterns of mould and bacteria on dirty dishes. These phenomena all have a basic mechanism in common, which can be stated as follows: many dissipative, spatially extended systems that are driven sufficiently far away from equilibrium form patterns in both space and time.

The weakly nonlinear description of such patterns is the central theme of this thesis. This means that we limit ourselves to the type of patterns that occur when systems are not too far from equilibrium. Such patterns typically occur via a bifurcation of a homogeneous state, and by linear stability analysis around this bifurcation point some information can be obtained. For any finite distance from the bifurcation point, nonlinear effects will play a role and a purely linear analysis is no longer sufficient. However, close to the bifurcation, a perturbation expansion is often able to describe the basic phenomenology of the patterns. An essential ingredient is the separation of scales that occurs near the bifurcation. On top of a small scale periodic structure that is governed by linear analysis there are deformations on long time and length scales that are governed by universal *amplitude equations* [4]. In this regime, the amplitude equations, although considerably simpler than the underlying equations of motion, yield an almost complete description of the patterns close to the bifurcation, with the exception of non-adiabatic effects [5] that we will discuss at the end of this chapter. In many cases, theory and experiment can be made in close contact [4].

In systems of only a few degrees of freedom, such as a double pendulum, the structure of phase-space can be studied in detail, and a description of the complicated temporal behavior of such systems had been developed over the past 20 years [4]. In spatially extended systems however, the behavior in both time and space can be equally complex, and a description of the spatial structures that occur is highly non-trivial [6]. One of the important steps towards a description of these patterns was the paper by Newell and Whitehead which started the amplitude equation description of patterns [7]. In subsequent years it became apparent that these amplitude equations are universal, in the sense that they occur under generic conditions for many different physical systems; the details of the underlying physical system are reflected in the coefficients of the amplitude equations [4]. As of this writing, many questions are still under debate or even completely open. We would like to mention two of these items here. First, for patterns in two or more dimensions that can not be viewed as distortions of quasi one-dimensional patterns, it is not clear what a correct amplitude description should be [4, 8]. In some cases, a description in terms of a small number of coupled equations may be used [9], but for truly higher dimensional phenomena it is not clear how to proceed. Second, both physical systems

and the amplitude equations show the occurrence of spatio-temporal chaos for suitable (system) parameters (see section 1.6.2). Although some progress in the understanding of this phenomena have been made over the last few years [10], we are yet still far from a comprehensive view on spatio-temporal chaos.

In this thesis we will concentrate on one-dimensional patterns, and only touch upon the issue of spatio-temporal chaos. In particular, we focus on patterns that occur via a finite wavelength instability. The amplitude equations that arise then are the so-called Ginzburg-Landau equations [4], and in the following, the terms "amplitude equations" and "Ginzburg-Landau equations" will be used interchangeably.

The remaining part of this first chapter introduces the amplitude equations and discusses the basic phenomenology of their solutions. On the experimental side, the emphasis is on convection systems. On the theoretical side, we explain the derivation of the amplitude equations and perform such derivation for a simple model system, the so-called Swift-Hohenberg equation (see section 1.4). Furthermore, we discuss the stability of phase-winding solutions, we introduce the concept of coherent structures and show the occurrence of spatio-temporal chaos when all phase-winding solutions are unstable. We conclude this chapter by a discussion of the validity of the amplitude approach.

In chapter 2 the coefficients of the (coupled) amplitude equations are calculated for a rotating convection system. It should be noted that only for a few experimental systems these coefficients have been calculated. The very laborious calculation carried out in chapter 2 is motivated by the following. On the one hand, the coefficients of the amplitude equation depend on the rotation-rate of this system. On the other hand, these coefficients determine the behavior of the patterns, and in particular whether the pattern is ordered or chaotic. We search for a realization of the convection system such that the rotation-rate tunes the coefficients of the amplitude equations through the various ordered and chaotic regimes that have been studied theoretically. Indeed we find that for a suitable chosen convection fluid, the rotation-rate is capable of this; to the best of our knowledge, this is the first experimental realization of the one-dimensional complex Ginzburg-Landau equation where the coefficients can be tuned so easily over such a wide range.

In chapter 3 we deal with two coupled amplitude equations. As a function of the coupling coefficient between the amplitude equations, either single or bimodal states are stable. We deal with the question what happens when this coupling coefficient is spatially dependent, such that a domain-wall between a single and a bimodal state occurs. Surprisingly, this domain-wall can be destabilized as a function of system parameters, and for a simple toy model we can show this analytically. For both a toy model and the real and complex Ginzburg-Landau equations we perform a numerical study of the behavior beyond this instability.

In the final chapter we deal with the interaction of pulses and fronts in models of binary liquid convection. We discuss the basic notion of coherent structures and give the standard picture of the interaction between pulses and fronts as given in [11]. However, this picture was developed for a standard Ginzburg-Landau equation, that does not describe the difference between velocity of the pulses and the group-velocity which is an essential feature of the experiments in binary liquid convection. We extend the amplitude equations

to account for this effect, and find a transition to irregular pulse motion, that can be understood in a simple analytical framework.

1.2 Patterns.

The starting point for the theoretical analysis of patterns consists of the equations of motion of the underlying physical system. These are often a deterministic set of nonlinear partial differential equations for the order parameter U :

$$\partial_t U(x, t) = G[U, \partial_x U, \dots; R], \quad (1.2.1)$$

where G is in general a nonlinear function of U and its spatial derivatives and of R , which is a control parameter. These equations sometimes need to be supplemented by stochastic terms describing noise, but for a large macroscopic pattern forming system the noise is rather small and can often be neglected [4]. A typical class of equations of interest are so-called reaction-diffusion equations of the form

$$\partial_t U = D \nabla^2 U + f(U, R), \quad (1.2.2)$$

which for $f \equiv 0$ is the diffusion equation with well known behavior (U is in general an n -component vector). A nonzero f models reaction in the system, and in that case, the behavior of the solutions of this equation can be highly complex. The aim of the theory is to describe the solutions which are likely to be reached starting from physical initial conditions and to persist for long times [4].

In general the nonlinear equations cannot be solved analytically, and one therefore aims to describe their solutions qualitatively or perturbatively. It will turn out that patterns typically emerge once a control parameter exceeds a certain critical value and that often the amplitude of the pattern grows continuously from zero when the control parameter is increased beyond its critical value. One then first constructs solutions of the linearized equations of motion. Then one takes into account the nonlinearities that start to play a role for nonzero amplitude, that is for control parameter above its critical value, by means of perturbation theory. The perturbation of the linear pattern is governed by the amplitude equations. In other words: *A large number of pattern forming phenomena can be analyzed perturbatively by using so-called amplitude equations, which describe slow modulations in space and time of a simple basic pattern that can be determined from the linear analysis of the equations of motion of the physical system.*

The form of the amplitude equation depends only on the nature of the linear instability, but not on other details of the system. The most important distinction is whether the basic pattern is stationary, leading to the real amplitude equation, or intrinsically time dependent, in which case an equation with complex coefficients describes the amplitude [4]. As noted before, the form of these equations is independent of details of the underlying system; only the coefficients in the amplitude equations reflect the physical details. The description in terms of amplitude equations therefore can be used to understand something

of the universal pattern forming behavior displayed by a number of different physical systems.

We will proceed by introducing convection systems and by elucidating some of the methods used to analyze their patterns.

1.2.1 The Rayleigh-Bénard instability.

Probably the most famous pattern-forming system is the Rayleigh-Bénard experiment, where a horizontal layer of fluid is heated from below [3, 4]. Since the hot fluid expands, the vertical temperature gradient across the fluid results in a density gradient. Therefore, we encounter a destabilizing force, the buoyancy force, since the colder, heavier fluid would like to fall down in order to minimize the gravitational energy. The viscosity of the fluid has a stabilizing effect, and for small temperature gradients the fluid remains at rest and there is only heat conduction in the system. Small perturbations of the stationary conducting state decay so the conducting state is linearly stable.

However, when the temperature gradient exceeds a certain critical value, the viscosity can no longer damp the tendency of the fluid to move due to the buoyancy force and the conductive state becomes unstable. It is useful to define the so-called Rayleigh number R , which measures the ratio of destabilizing buoyancy force to the viscous force, and is the important control parameter of the system. So when R increases above a certain critical value R_c , small perturbations of the basic state grow and a so-called convecting pattern emerges. Since not all the cold fluid can fall down simultaneously, the fluid will start to move up and down in a certain pattern, and the onset of convection therefore breaks the homogeneity of the basic conducting state. The simplest ordering of such a convective pattern consists of parallel rolls, as shown in figure 1-1. The hydrodynamic equations describing this system are the Navier-Stokes equation supplemented with the heat equation and the mass conservation law. We are interested in the situation where a temperature difference is maintained between two horizontal plates. In general the parameters of the Navier-Stokes equation like viscosity and thermal conductivity depend on temperature and density, and taking this coupling into account makes the equations very complicated. However, in the weakly nonlinear regime the temperature difference is typically of the order of 1K, so this coupling is not very important. The Boussinesq approximation [3] only includes the temperature dependence in the all important buoyancy force term, and otherwise assumes an incompressible fluid with constant material parameters. In this approximation the fluid equations are:

$$(\partial_t + \vec{v} \cdot \vec{\nabla})\vec{v} = -\vec{\nabla}(P/\rho) + \nu \nabla^2 \vec{v} - g\alpha T \hat{z}, \quad (1.2.3a)$$

$$(\partial_t + \vec{v} \cdot \vec{\nabla})T = \kappa \nabla^2 T, \quad (1.2.3b)$$

$$\vec{\nabla} \cdot \vec{v} = 0, \quad (1.2.3c)$$

where g is the acceleration of gravity, ν is the viscous diffusivity, κ is the thermal diffusivity, α is the thermal expansion coefficient, ρ is the density at some properly chosen mean temperature and \vec{v} , P and T denote fluid-velocity, pressure and temperature. These equations in principle should be supplemented by stochastic noise terms, reflecting the

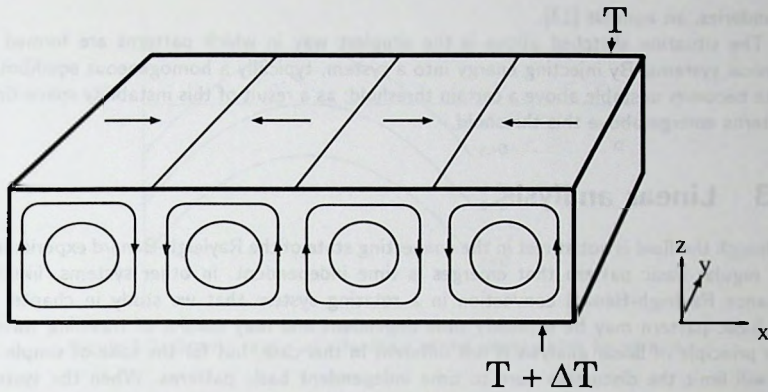


Figure 1-1. Sketch of parallel convecting rolls in a Rayleigh-Bénard experiment. The vertical temperature gradient causes the fluid to move in a roll-like pattern as indicated.

small scale degrees of freedom of the molecular constituents of the fluid. These terms are however very small; for ordinary Rayleigh-Bénard convection they typically turn out to be of relative order 10^{-9} [4], and we shall neglect the stochastic forcing here.

To treat the onset of convection, we write down perturbation equations, perturbing around a state of steady conduction. When we denote the temperature difference between top and bottom plate by ΔT , and the height of the layer by d , the temperature profile of the steady state is given by $T = T_0 - z\Delta T/d$, where z is the vertical coordinate and T_0 is the temperature of the top plate at $z = 0$. The deviation of the temperature from this steady profile is denoted by θ , and scaling length by d , time by the thermal diffusion length d^2/κ and the temperature by $\kappa\nu/\alpha g d^3$, we obtain the hydrodynamic equations in the Boussinesq approximation (1.2.3a) - (1.2.3c) in dimensionless units,

$$\left(\frac{1}{\sigma}\partial_t - \nabla^2\right)\vec{v} + \vec{\nabla}P - \theta\vec{z} = -\frac{1}{\sigma}(\vec{v} \cdot \vec{\nabla})\vec{v}, \quad (1.2.4a)$$

$$(\partial_t - \nabla^2)\theta - Rv_z = -(\vec{v} \cdot \vec{\nabla})\theta, \quad (1.2.4b)$$

$$\vec{\nabla} \cdot \vec{v} = 0, \quad (1.2.4c)$$

where $R := g\alpha\Delta T d^3/\kappa\nu$ denotes the Rayleigh number, and $\sigma := \nu/\kappa$ is the Prandtl number which measures the ratio of thermal and viscous diffusivities. When R is increased above R_c , a pattern of parallel rolls emerges in simple cases. In many experiments the horizontal layer of fluid extends in both x and y directions, so modulations close to onset can not be described by the one-dimensional amplitude equations that we study here [4]. To study patterns that are essentially one-dimensional, the geometry of the convection cell can be chosen a long straight channel [12], or to minimize the effect of the lateral

boundaries, an annulus [13].

The situation sketched above is the simplest way in which patterns are formed in physical systems. By injecting energy into a system, typically a homogeneous equilibrium state becomes unstable above a certain threshold; as a result of this instability space-time patterns emerge above this threshold.

1.3 Linear analysis.

Although the fluid is not at rest in the convecting state of the Rayleigh-Bénard experiment, the regular basic pattern that emerges is time independent. In other systems, like for instance Rayleigh-Bénard convection in a rotating system that we study in chapter 2, the basic pattern may be explicitly time dependent and may consist of traveling waves. The principle of linear analysis is not different in this case, but for the sake of simplicity we will limit the discussion here to time independent basic patterns. When the system is rotationally invariant in the plane, the direction of the wave-vector is immaterial, and we can for simplicity take the wave-vector parallel to the x -direction. We shall neglect all y -variation, i.e., we consider one-dimensional patterns. We take the system infinitely long in the x -direction, so as to avoid studying the between the left- and right-traveling waves, effects of lateral boundaries, and we assume left-right reflection symmetry. In this case we may look for Fourier-mode-like solutions for the linearized equations of motion of the form

$$U(x, y, z, t) = F(z)e^{st+iqx} + c.c., \quad (1.3.1)$$

where $c.c.$ denotes the complex conjugate, U is a vector describing the physical fields such as velocity and temperature and $F(z)$ is some basic mode in the vertical direction whose details are not of interest to us now; the growth-rate s is a real number for the present case and q is the wavenumber of the mode. Substituting the ansatz (1.3.1) into the linearized equations of motion of the fluid, we find the dispersion relation $s(q)$. This dependence of the growth-rate on q is sketched for three values of the reduced control parameter $\varepsilon = (R - R_c)/R_c$ in figure 1-2.

The homogeneous basic state is stable if there is no q such that the growth-rate is positive, and this is clearly the case for $\varepsilon < 0$. If the control parameter passes through zero, there starts to emerge a small band of wavenumbers around q_c that correspond to growing modes, therefore the homogeneous state becomes unstable and a pattern with wavenumbers inside the band around q_c emerges.

Since the fluid-equations are relatively complicated, it is useful to introduce a simple model equation which illustrates the linear instability sketched above. When we demand that the linear growth-rate of plane-wave solutions of the form e^{iqx} is quadratic around a certain wavenumber q_c , as sketched in figure 1-2, and further require a $x \rightarrow -x$ symmetry, the linear part of such model equation follows immediately, and so we find an equation of the form $\partial_t u = \varepsilon u - D(\partial_x^2 + q_c^2)^2 u + f(u)$, where f is some nonlinear function. It is easy to check that when the ansatz $u(x, t) = e^{st+iqx} + c.c.$ is substituted into this equation,

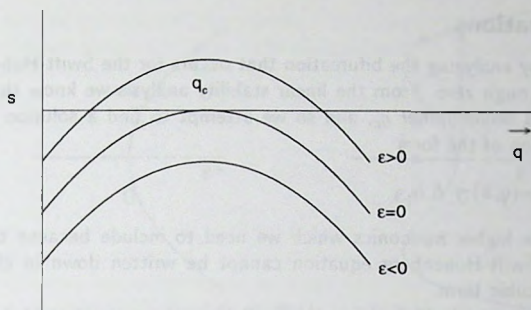


Figure 1-2. Growth rate s as a function of the wavenumber for various ϵ .

we find that $s = \epsilon - D(q_c^2 - q^2)^2$, so indeed the growth-rate behaves qualitatively as sketched in figure 1-2 for $q \approx \pm q_c$.

Let us require that this model equation be invariant under a change of sign of u , then the simplest nonlinearity is a cubic one. If we include a cubic term of the form $-u^3$, we find the so-called Swift-Hohenberg equation [14]:

$$\partial_t u = \epsilon u - (\partial_x^2 + q_c^2)^2 u - u^3. \quad (1.3.2)$$

Here we have used the fact that with a proper rescaling of space D can be put equal to one; by rescaling u the pre-factor of the term u^3 , provided that it is negative, can always be put equal to -1 . Note that this equation is much simpler than the fluid-equations. For instance u is meant to be a single real function of x and t , whereas in the equations of motion for the Rayleigh-Bénard experiment we have a vector velocity and temperature field depending on x, y, z and t .

Now that we have a simple model to describe the instability of the homogeneous state in a one-dimensional Rayleigh-Bénard experiment, we can ask ourselves whether this model also describes the birth of the convecting state. In the next section we will show that when the homogeneous $u = 0$ state becomes unstable, a new periodic state emerges which describes the periodic pattern found in the Rayleigh-Bénard experiment.

It should be noted that since one in general cannot define a free energy for pattern forming systems and since there is usually no thermodynamic limit involved, the transition to convection is not a phase transition, but is associated with a qualitative change in the behavior of solutions of a set of equations, which occurs when a control parameter is varied. This is called a bifurcation. Above threshold, i.e., for $\epsilon > 0$, it turns out that generally there exists a continuous family of solutions, e.g., periodic roll patterns with wavelengths in a band. This is another difference between the bifurcations found in pattern forming systems and phase transitions, where the transition is between *two* phases.

1.3.1 Bifurcations.

We will proceed by analyzing the bifurcation that occurs for the Swift-Hohenberg model when ε passes through zero. From the linear stability analysis we know that the fastest growing mode has wavenumber q_c , and so we attempt to find a solution of the Swift-Hohenberg equation of the form

$$u(x, t) \sim \cos(q_c x) + h.h. , \quad (1.3.3)$$

where *h.h.* denote higher harmonics which we need to include because the non-trivial solutions of the Swift-Hohenberg equation cannot be written down in closed analytic form, due to the cubic term.

If we substitute equation (1.3.3) into the Swift-Hohenberg equation (1.3.2), it is found that for small ε we can construct a solution of the form

$$u(x, t) \sim \sqrt{\varepsilon} \cos(q_c x + \phi) + \mathcal{O}(\varepsilon) , \quad (1.3.4)$$

with ϕ arbitrary. This arbitrariness of ϕ reflects the translational symmetry of the Swift-Hohenberg equation, since a change of ϕ can be incorporated in a shift of x . It can be shown that this solution is stable for small ε . We will interpret this periodic state as the analogue of the convecting state in the Rayleigh-Bénard experiment. If we now sketch the amplitude of the "conducting" $u = 0$ and "convecting" $u \sim \cos(q_c x)$ solutions as a function of the control parameter and denote the linear stability of these solutions by continuous (stable) and dashed (unstable) curves, we obtain a so-called bifurcation diagram [15]. The "convecting" $u \sim \cos(q_c x)$ solution is seen to bifurcate from the "conducting" $u = 0$ solution. Note that we are usually interested in the absolute value of the amplitude, and in that case only the upper part of figure 1.3.4 is relevant.

We now focus on the types of bifurcations that are important in the study of patterns. In figure 1-3 we sketch the bifurcation diagrams of a supercritical (forward) pitchfork bifurcation as found in the Swift-Hohenberg equation and in the Rayleigh-Bénard experiment, and of a subcritical (backward) bifurcation as found for instance in the Rayleigh-Bénard experiment in binary fluid-mixtures.

In the supercritical case, when we increase ε through zero, we find that the homogeneous $u = 0$ state becomes linearly unstable at $\varepsilon = 0$ and a new solution bifurcates from the $u = 0$ state. For $\varepsilon > 0$ the system will be pushed from the unstable "conducting" state (by small perturbations such as noise) and end up in this "convecting" $u \neq 0$ state. Note that for this supercritical bifurcation the amplitude of the "convecting" pattern grows like a square root above onset, and when we let the control parameter pass through zero, the amplitude of the stable and therefore experimentally observed mode varies continuously. In that sense the supercritical bifurcation is reminiscent of a second order phase transition.

The subcritical bifurcation diagram, on the other hand, describes a different situation. If ε is increased through zero, the $u = 0$ state loses stability and the system will jump and end up on some $u \neq 0$ branch. If we now decrease ε again, the system will remain on this branch until $\varepsilon < \varepsilon_1$ and then jump back to the $u = 0$ state. This hysteresis

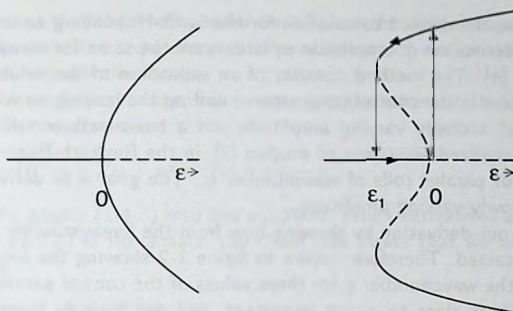


Figure 1-3. Supercritical and subcritical bifurcations. Solid lines refer to stable solutions, dashed lines to unstable ones. The vertical axis represents the order parameter that we are interested in; for equation (1.3.4) this is u .

and discontinuous change of the amplitude is similar to a first order phase transition. Subcritical bifurcations occur for instance in Rayleigh-Bénard experiments in binary fluid-mixtures or directional solidification [4], and considerably complicate the analysis, because one in general cannot make an expansion for small ε and u , as can and will be done below for the supercritical case.

Having introduced the distinction between supercritical and subcritical bifurcations, we will add another concept; a bifurcation is called stationary if the resulting basic pattern is time independent as in the Swift-Hohenberg equation, and it is called oscillatory (also known as Hopf bifurcation [4, 15]) if the critical mode is time-dependent. For oscillatory instabilities with nonzero wave-vector the basic pattern is a traveling wave mode of the form $\exp[i(qx - \omega t)]$. Note that the distinction between these two types is independent of the bifurcation being sub- or supercritical. Although as mentioned above the fluid is in motion in the Rayleigh-Bénard experiment, the basic roll pattern is stationary just above threshold, and the onset of convection occurs via a stationary supercritical (pitchfork) bifurcation [3]. We will later see examples of equations and physical systems with Hopf bifurcations.

1.4 Amplitude equations.

In this section we will explicitly demonstrate how an amplitude equation is derived from a given set of starting equations showing a finite wavelength instability. We follow the "classical" multiple scale analysis [4, 7], but it should be noted that recently a derivation based on renormalization theory was put forward [16]. To fix the ideas, one could think of Rayleigh-Bénard convection restricted to patterns of parallel rolls, therefore only allowing for modulations in one direction, so that the amplitude equation is one-dimensional. We will indicate how such a derivation is performed, but to minimize technical details we will

only illustrate here the explicit calculation for the Swift-Hohenberg equation (1.3.2). The principles of the derivation of amplitude equations are the same for many types of pattern forming systems [4]. The method consists of an expansion of the solution U of the full equations of motion in the control parameter ε , writing the leading term of this expansion as the product of a slowly varying amplitude and a basic pattern which is the critical solution of the linearized equations of motion [7]; in the Rayleigh-Bénard case this basic pattern consists of parallel rolls of wavenumber q_c . The goal is to derive an equation of motion for the slowly varying amplitude.

We will start our derivation by showing how from the linear stability analysis the slow scales can be obtained. Therefore, return to figure 1-2 showing the linear growth-rate s as a function of the wavenumber q for three values of the control parameter ε . For small ε , only wavenumbers close to q_c are important, and one finds to lowest order in ε and $(q - q_c)$ that

$$s = \left(\frac{\partial s}{\partial \varepsilon} \right)_0 \varepsilon + \frac{1}{2} \left(\frac{\partial^2 s}{\partial q^2} \right)_{q_c} (q - q_c)^2 + \dots, \quad (1.4.1)$$

so, according to linear theory, only modes with wave-vectors in a band around q_c of width $\approx \sqrt{\varepsilon}$ are growing. These are the modes which play the dominant role in the long time behavior of the full nonlinear equations of motion. The following trivial observation explains why this long time behavior can be described by slow modulations of the critical mode, at least in the bulk of the system: If a solution of the full equations of motion contains a mode with x -dependence e^{iqx} , we can write this as $e^{i(q-q_c)x} e^{iq_c x}$, and since all dominant modes have $|q - q_c| \leq \varepsilon^{1/2}$, the x -dependence of the full solution can indeed be approximated as the product of a slow spatial modulation $e^{i(q-q_c)x}$ and the critical mode $e^{iq_c x}$. When for these dominant modes the phase factor $(q - q_c)x$ changes by an amount of order unity, the spatial scale on which this happens goes like $1/(q - q_c) \sim \varepsilon^{-1/2}$. We therefore expect the length scale of the modulations to scale as $\varepsilon^{-1/2}$.

The growth-rate of the relevant modes varies linearly in ε , and from an analogous argument it is found that the characteristic time scale of the modulations is proportional to ε^{-1} . Finally, from the shape of the bifurcation curve (figure 1-3a) it follows that the amplitude grows as $\varepsilon^{1/2}$. We therefore expect solutions of the fully nonlinear equations to be of the form

$$U = \varepsilon^{1/2} A(X, T) U_{lin} + c.c. + h.o.t., \quad (1.4.2)$$

where $X := \varepsilon^{1/2} x$ and $T := \varepsilon t$ are the explicit slow scales, U_{lin} is the critical solution of the linearized equations of motion and $h.o.t.$ denotes higher order terms. We confine ourselves to one spatial dimension. Our task is to find an equation for the amplitude A . As we shall see, the higher order terms arise naturally in this expansion as well, but their amplitude is driven by the amplitude A ; this is called *slaving*.

To derive the amplitude equation, we construct a weakly nonlinear expansion of the full equations of motion, by assuming

$$U = \varepsilon^{1/2} U_0 + \varepsilon U_1 + \varepsilon^{3/2} U_2 + \dots, \quad (1.4.3)$$

where it will turn out that the leading order term U_0 can be written as $A(X, T)U_{lin}$ as in (1.4.2). If we substitute this expansion into the equations of motion, we naturally arrive at a separation of fast and slow scales.

To see how this works in practice, let us now apply the scheme to the Swift-Hohenberg equation (1.3.2) in one dimension:

$$\partial_t u = \varepsilon u - (\partial_x^2 + q_c^2)^2 u - u^3 =: \varepsilon u - \mathcal{L}u - u^3, \quad (1.4.4)$$

by substituting the ansatz (1.4.3) into this equation. When derivatives are taken of products of the form (1.4.2) in the ansatz, the chain rule shows that we need to replace ∂_t and ∂_x as follows:

$$\partial_t \rightarrow \varepsilon \partial_T, \quad \partial_x \rightarrow \partial_x + \varepsilon^{1/2} \partial_X, \quad (1.4.5)$$

where in the expression for ∂_x , the x on the left-hand side acts on spatial dependence on all length scales, and on the right-hand side x *only* acts on the fast spatial dependence of the $e^{\pm iq_c x}$ terms, while ∂_X acts on the slow spatial variable. Carrying out this separation of scales we find for the linear operator \mathcal{L}

$$\begin{aligned} \mathcal{L} &= (\partial_x^2 + q_c^2)^2 \rightarrow \underbrace{(\partial_x^2 + q_c^2)^2}_{L} + 2\varepsilon^{1/2} \partial_x \partial_X + \varepsilon \partial_X^2 \\ &= L^2 + 4\varepsilon^{1/2} L \partial_x \partial_X + \varepsilon (2L + 4\partial_x^2) \partial_X^2 + \mathcal{O}(\varepsilon^{3/2}), \end{aligned} \quad (1.4.6)$$

where for notational convenience, L is defined as $\partial_x^2 + q_c^2$. If we now substitute this together with the ansatz for u into the Swift-Hohenberg equation, we find

$$\begin{aligned} \{L^2 + 4\varepsilon^{1/2} L \partial_x \partial_X + \varepsilon (\partial_T - 1 + (2L + 4\partial_x^2) \partial_X^2) + \mathcal{O}(\varepsilon^{3/2})\} \times \\ \{(\varepsilon^{1/2} u_0 + \varepsilon u_1 + \varepsilon^{3/2} u_2 + \mathcal{O}(\varepsilon^2))\} + \varepsilon^{3/2} u_0^3 + \mathcal{O}(\varepsilon^2) = 0. \end{aligned} \quad (1.4.7)$$

When we collect orders in ε this leads to a hierarchy of equations of which the lowest is

$$\mathcal{O}(\varepsilon^{1/2}): (\partial_x^2 + q_c^2)^2 u_0 = 0, \quad (1.4.8)$$

so at leading order we find an equation which determines the linearized solution

$$u_0 = e^{iq_c x} A_0(X, T) + e^{-iq_c x} A_0^*(X, T), \quad (1.4.9)$$

where it should be noted that the complex amplitude function A_0 can be completely arbitrary at this level, since the linear operator $(\partial_x^2 + q_c^2)^2$ only acts on the fast scales. At the next order we find

$$\mathcal{O}(\varepsilon): \underbrace{4(\partial_x^2 + q_c^2) \partial_x \partial_X u_0}_{=0} + (\partial_x^2 + q_c^2)^2 u_1 = 0, \quad (1.4.10)$$

where the first term is zero because $L u_0 = 0$. Analogous to the previous order, it therefore follows that

$$u_1 = e^{iq_c x} A_1(X, T) + c.c., \quad (1.4.11)$$

where A_1 also can be chosen arbitrarily at this level. It can however be determined from higher equations in the hierarchy. This equation does not help us, but at the next order we will find an equation of motion for A_0 , the leading slow amplitude. We find

$$\mathcal{O}(\varepsilon^{3/2}) : L^2 u_2 + \underbrace{4L\partial_x \partial_X u_1}_{=0} + (\partial_T - 1 + \underbrace{2L\partial_X^2}_{\rightarrow 0} + 4\partial_x^2 \partial_X^2 + u_0^2) u_0 = 0, \quad (1.4.12)$$

which by eliminating the zero terms and expanding the nonlinear term leads to

$$L^2 u_2 + [e^{iq_c x} (\partial_T - 1 - 4q_c^2 \partial_X^2 + 3|A_0|^2) A_0 + c.c.] + (e^{3iq_c x} A_0^3 + c.c.) = 0. \quad (1.4.13)$$

From this it follows that u_2 is of the form $e^{iq_c x} A_2 + e^{3iq_c x} B_2 + c.c.$, where A_2 and B_2 are slow amplitudes which are not determined at this level. However, the crucial point is the following: $L^2 u_2$ does not contain any $e^{iq_c x}$ dependence, since $LAe^{iq_c x} = 0$ for all slow amplitudes A . So, in order to satisfy equation (1.4.13), the coefficient of $e^{iq_c x}$ in (1.4.13) must vanish. This so-called solvability condition is the way in which the amplitude equation arises in general. In this case, we find that A_0 must satisfy

$$\partial_T A_0 = A_0 + 4q_c^2 \partial_X^2 A_0 - 3|A_0|^2 A_0. \quad (1.4.14)$$

This is the amplitude equation we wanted to derive. By a simple rescaling of X and A_0 , we can eliminate the constants $4q_c^2$ and 3. The fact that this form of the amplitude equation is independent of ε shows that we have chosen the scales of space, time and amplitude correctly.

The calculation of amplitude equations for more complicated systems with a forward stationary bifurcation is technically more involved, but the principles are the same: by separating in the equations of motions all derivatives into a slow and a fast part (i.e. $\partial_x \rightarrow \partial_x + \varepsilon^{1/2} \partial_X$) and assuming for U an expansion of the form (1.4.3), a systematic expansion of the equations of motion is obtained. The first equation in this hierarchy corresponds to the linearized equation of motion and therefore does not tell us anything about the amplitude A_0 . The second equation is also of no help, but the third equation is in general of the form

$$\mathcal{L}_f U_2 = RHS[A], \quad (1.4.15)$$

where \mathcal{L}_f is the fast part of the linear operator of the starting equation. Just as for the derivation of the amplitude equation carried out above, we find a solvability condition: equation (1.4.15) has, according to the Fredholm theorem [4], a solution if and only if the RHS is orthogonal to the zero space of the linear operator \mathcal{L}_f and this condition gives us the general amplitude equation:

$$\tau_0 \partial_t A = \varepsilon A + \xi_0^2 \partial_x^2 A - g_0 |A|^2 A, \quad (1.4.16)$$

which now is written down for the fast scales x and t .

The coefficients τ_0 , ξ_0 and g_0 can be calculated from the full equations describing the physical problem under study (for instance, from the equation for the linear growth-rate (1.4.1) it follows that $\tau_0^{-1} = \partial s / \partial \varepsilon$ and $\xi_0^2 \tau_0^{-1} = -(1/2) \partial^2 s / \partial q^2$). For convenience we can scale these coefficients out by a suitable choice of space, time and amplitude scales. Note that we cannot scale away the sign of g_0 , because for positive g_0 the nonlinear term is stabilizing and we have a supercritical bifurcation, while a negative g_0 gives rise to a destabilizing effect on the amplitude and the bifurcation is subcritical; higher order stabilizing nonlinearities are then necessary to obtain a stationary solution. We now assume a supercritical bifurcation as in ordinary Rayleigh-Bénard convection, and after the aforementioned scaling we obtain

$$\partial_t A = \varepsilon A + \partial_x^2 A - |A|^2 A. \quad (1.4.17)$$

We prefer to keep ε explicit in (1.4.17), so as to avoid a control parameter dependent rescaling. This will make it easier to consider what happens when ε goes through zero.

Equation (1.4.17) arises naturally near any stationary supercritical bifurcation when the system is translationally invariant and reflection symmetric ($x \rightarrow -x$). The latter symmetry dictates that the second order term $\partial^2 / \partial x^2$ arises as the lowest order spatial derivative, while the form of the cubic term is prescribed by the requirement that the equation be invariant upon multiplying A by an arbitrary phase factor $\exp(i\phi)$: this corresponds to translating the pattern by a distance ϕ/q_c , so translational invariance implies that the equation for A has to be invariant under $A \rightarrow A e^{i\phi}$ [4].

Equation (1.4.17) has the form of the Ginzburg-Landau equation for superconductivity in the absence of a magnetic field [17] and is often referred to as the Ginzburg-Landau equation. To distinguish it from the amplitude equation for traveling waves given below, we will refer to it as the real Ginzburg-Landau equation (RGLE), since the coefficients in this equation are real; the amplitude itself is a complex valued function.

If the instability is to traveling waves, i.e. if the pattern which emerges is intrinsically time-dependent, the resulting amplitude equation generalizes to the complex Ginzburg-Landau equation (CGLE) [4]. Still the principle of derivation is the same, but since the solutions of the linearized equations of motion are traveling waves of the form $e^{i(q_c x - \omega_c t)}$, where ω_c is the critical frequency, we write the lowest order solution as $U_0 = e^{i(q_c x - \omega_c t)} A_0(X, T) + c.c.$ Since there is now both fast and slow time dependence, ∂_t transforms to $\partial_t + \varepsilon \partial_T$. Performing the ε expansion and scaling away superfluous constants, we find as amplitude equation the CGLE:

$$\partial_t A + v_g \partial_x A = \varepsilon A + (1 + ic_1) \partial_x^2 A - (1 - ic_3) |A|^2 A, \quad (1.4.18)$$

where c_1 and c_3 are real coefficients, and v_g is the group-velocity. Naively, one would expect $(1 + ic_0)$ in front of the εA term, but unlike c_1 and c_3 , c_0 can be transformed away by going to a phase-rotating frame, i.e., by setting $\tilde{A} = e^{-ic_0 t} A$. Solutions of the CGLE are qualitatively different for different values of c_1 and c_3 . These coefficients can be calculated from the basic equations of motion by performing the same expansion as in the real case. An explicit example of such calculation will be given in chapter 2.

We have written only one CGLE for a single amplitude, i.e., we have broken the symmetry under reflection ($x \rightarrow -x$). If the starting system is itself symmetric both left- and right-moving traveling waves can exist. For such systems, one actually obtains two coupled CGLE's, one for the amplitude A of the right-moving waves and one for the amplitude B of the left-moving waves:

$$\begin{aligned} \partial_t A + v_g \partial_x A &= \varepsilon A + (1 + ic_1) \partial_x^2 A - (1 - ic_3) |A|^2 A \\ &\quad - g_2 (1 - ic_2) |B|^2 A, \end{aligned} \quad (1.4.19a)$$

$$\begin{aligned} \partial_t B - v_g \partial_x B &= \varepsilon B + (1 + ic_1) \partial_x^2 B - (1 - ic_3) |B|^2 B \\ &\quad - g_2 (1 - ic_2) |A|^2 B. \end{aligned} \quad (1.4.19b)$$

The coefficients of both equations are equal on grounds of the left-right symmetry. When the cross-coupling constant g_2 is larger than one, the two modes suppress each other, and the system ends up in patches where either A or B is zero. Within such a patch, one may use a single CGLE to describe the dynamics. The border regions between two patches should be described by at least two coupled amplitude equations, but non-adiabatic effects, that escape an amplitude expansion, seem to play a role here (see section 1.7). In experiments one can try to manipulate the system to be in a single-mode state, where either A or B is zero, and a single amplitude is sufficient.

When g_2 is smaller than one, A and B are both nonzero, and for spatially homogenous states one even finds that $|A| = |B|$ (provided that the wavenumbers of both modes are equal).

Note that we can not scale away the group-velocity terms, and this presents us with a serious problem: only when the group-velocity is of order $\varepsilon^{1/2}$, the amplitude equations are self-consistent. In general this is not true, and when the states are not homogeneous, this represents in our view a serious problem with the CGLE (see section 1.7).

When the cross-coupling constant is larger than one and one of the modes is completely suppressed, one can effectively use a single CGLE like (1.4.18) and the $v_g \partial_x A$ term can be eliminated by a Galilean transformation; we then end up with:

$$\partial_t A = \varepsilon A + (1 + ic_1) \partial_x^2 A - (1 - ic_3) |A|^2 A, \quad (1.4.20)$$

which is the form of the CGLE which is used most often in theoretical studies. In the limit $c_1, c_3 \rightarrow 0$ we recover the RGLE.

To derive these amplitude equations, the only essential assumption we used was that there is a supercritical bifurcation with wavenumber unequal to zero. If this is the case, the amplitude equations are generically the real or the complex one, depending on whether the bifurcation is stationary or oscillatory. Therefore, these equations describe the weak nonlinear regime of many physical systems, and are in a sense universal.

When the bifurcation in the underlying physical system is subcritical, the amplitude equations should reflect this. However, as one sees immediately from figure 1-3b, in the vicinity of the bifurcation, the amplitude $|A|$ is not necessarily small. As a consequence, one can not, with the exception of a so-called weakly subcritical bifurcations, derive an amplitude expansion in a systematic way. In such a situation, the nonlinear term of the

amplitude equation is usually modified in order to mimic the subcritical bifurcation. One may hope this, at least qualitatively, reproduces the essential features of the physical system that one tries to describe. One should realize that in this case one does not deal with a systematic expansion of the underlying equations of motion, but with a model equation [4].

The RGLE for a subcritical bifurcation, sometimes referred to as the quintic RGLE is

$$\partial_t A = \varepsilon A + \partial_x^2 A + |A|^2 A - |A|^4 A, \quad (1.4.21)$$

where we have chosen appropriate scales for time, length and amplitude. Apart from being a toy model for subcritical bifurcations in spatially extended systems, this equation has not received much attention. However, for the CGLE the quintic extension

$$\partial_t A = \varepsilon A + (1 + ic_1)\partial_x^2 A + (1 + ic_3)|A|^2 A - (1 - ic_5)|A|^4 A, \quad (1.4.22)$$

has been studied extensively in the context of binary fluid convection (see chapter 4) and coherent structures (see below). The case of two coupled quintic CGLE's has not been studied as far as we are aware.

When the instability occurs for $q_c = 0$, then the form of the amplitude equations is different, but for supercritical bifurcations an amplitude description can still be given [2, 4].

1.4.1 Comparison between the RGLE and CGLE.

At first glance the real and the complex equation look rather similar, but it turns out that the behavior of solutions of these equations is very different. In order to explain this, we will now introduce the notion of a Lyapunov functional $F[u]$ [18]. This is a map from the state space u of the dynamical system to the real numbers, which behaves like a free energy; this F will not increase during the time evolution of the equation, and the dynamics tends to drive the solutions toward a local minimum of F . As an example, the Swift-Hohenberg equation (1.3.2) can be written as

$$\partial_t u = -\frac{\delta F}{\delta u}, \quad (1.4.23)$$

where

$$F[u] := \frac{1}{2} \int dx \left\{ [(\partial_x^2 + q_c^2)u]^2 - \varepsilon u^2 + \frac{1}{2}u^4 \right\}. \quad (1.4.24)$$

From this it follows that the dynamics decreases F , because

$$\frac{dF}{dt} = \int dx \frac{\delta F}{\delta u} \frac{\partial u}{\partial t} = - \int dx \left(\frac{\delta F}{\delta u} \right)^2 \leq 0. \quad (1.4.25)$$

Therefore the dynamics is "downhill" and is sometimes called gradient dynamics. For more general systems possessing a Lyapunov function, the precise time evolution may not be

determined from this Lyapunov function because there may be dynamical behavior which leaves F invariant (the evolution equation is then not of the form (1.4.23)) [19]. The importance of F is that final states, being either stationary or dynamic, can be obtained by finding minima of F . We should stress again that this sort of gradient dynamics is the exception, not the rule. For a more extensive discussion we refer to a paper by Montagne *et al.* [19]. In chapter 3 the notion of a Lyapunov functional will be important.

It is easy to check that the RGLE (1.4.17) can be written in the form

$$\frac{\partial A}{\partial t} = -\frac{\delta \mathcal{F}}{\delta A^*}, \quad \text{with } \mathcal{F} = \int dx \left[\left| \frac{\partial A}{\partial x} \right|^2 - \varepsilon |A|^2 + \frac{1}{2} |A|^4 \right], \quad (1.4.26)$$

from which it follows that $d\mathcal{F}/dt \leq 0$. Thus, \mathcal{F} is here the Lyapunov function, and many aspects of the dynamics of patterns can be simply understood in terms of the tendency of patterns to evolve towards the lowest free-energy state [4]. In this sense, the dynamics of (1.4.17) is very thermodynamic-like and is called relaxational. The inclusion of quintic terms into the RGLE does not break the variational structure.

When $c_1 = -c_3$, the CGLE can, after going to a rotating frame, by setting $\bar{A} = e^{ic_1 t} A$, be written as $\partial_t \bar{A} = (1 + ic_1)(\partial_x^2 \bar{A} + \varepsilon \bar{A} - |\bar{A}|^2 \bar{A}) = -(1 + ic_1) \frac{\delta \mathcal{F}}{\delta \bar{A}^*}$ [19]. For $c_1, c_3 \neq 0$, the CGLE has *not* been derived from a Lyapunov function and it displays a much richer variety of dynamical behavior than the real equation (1.4.17). There have been attempts to construct Lyapunov functions for the CGLE, but these are not exact and only work for relative simple behavior of the CGLE [19, 20].

In the limit $c_1, c_3 \rightarrow \infty$ the equation reduces to the Nonlinear Schrödinger equation, which is not only Hamiltonian but also integrable (it has the well-known soliton solutions) [11, 21]. The fact that the CGLE reduces to an equation possessing a Lyapunov function in one limit and to a Hamiltonian equation in another limit makes it very interesting from a theoretical point of view. In addition, these two limits have been exploited as starting points for perturbation expansions [4, 22].

1.4.2 Convective and absolute instabilities.

The question of linear stability is slightly more complicated if there is a mean flow in the system. Suppose we are looking at the flow of a liquid through a pipe. The simple homogeneous state then corresponds to laminar flow. Now suppose that this flow becomes unstable, because we increase the velocity of the fluid. Thus, small perturbations of the laminar state will grow in time. However, when perturbations are advected away by the overall fluid-velocity faster than they grow, then at a *fixed* position the perturbations will eventually die out. In this case the instability is called *convective*. When perturbations grow faster than they are advected away, or more precisely, if there exists a position in the lab frame such that some infinitesimal perturbations do not decay, then the instability is called *absolute* [4].

Note that the definition of convective and absolute instability is frame-dependent.

1.5 Phase winding solutions and secondary instabilities.

We now proceed to discuss simple solutions of the real and complex Ginzburg-Landau equations. We will encounter more complicated solutions in chapter 3 and 4, but in general these cannot be written down in closed, analytic form. To get a grip on these solutions, we first discuss the so-called phase-winding solutions which can be found easily. We restrict ourselves to the cubic equations.

The RGLE admits plane-waves in space of the form $A = ae^{iqx}$. These phase-winding solutions describe steady state periodic patterns with total wavenumber slightly bigger ($q > 0$) or slightly smaller ($q < 0$) than q_c .

For the CGLE, there exists a band of traveling wave solutions $A = ae^{-i\omega t + iqx}$. Just as q measures the difference between the wavenumber of the pattern and the critical wavenumber, ω measures the difference between the frequency of the pattern and the frequency of the critical mode, ω_c . Note that the RGLE does not permit these traveling wave solutions.

When we substitute the ansatz $A = ae^{-i\omega t + iqx}$ into equation (1.4.20), we obtain

$$\omega = c_1 q^2 - c_3 a^2, \quad q^2 = \varepsilon - a^2. \quad (1.5.1)$$

The expression for ω illustrates that c_1 is the coefficient which measures the strength of the linear dispersion, i.e. the dependence of the frequency of the waves on the wavenumber, while c_3 is a measure of the nonlinear dispersion.

So, the RGLE admits spatially periodic solutions e^{iqx} with wave-vector $-\varepsilon^{1/2} < q < \varepsilon^{1/2}$, and the CGLE admits traveling waves $e^{-i\omega t + iqx}$ with condition (1.5.1). What is the stability of these solutions? The linear stability analysis is quite straightforward but especially for the CGLE algebraically involved [23]. The stability analysis consists of simply substituting a trial function which is the sum of the phase-winding solution and a suitable periodic perturbation into the corresponding amplitude equation and linearizing the response to the small perturbation. This results in a growth-rate for the perturbation, which determines whether the phase-winding solution is linearly stable or unstable.

When a phase-winding solution becomes unstable, this is called a *secondary instability* since the solution itself emerged via an instability of the homogeneous $A = 0$ state. These secondary instabilities tend to make the patterns more complex and account for some of the complexity found in real experiments. For the real case the qualitative answer is well-known; consider the left part of figure 1-4. For a given $\varepsilon > 0$, the values of q for which steady state solutions exist fall within the solid line. However, only the solutions within the dashed lines are stable — solutions corresponding to values of q in the dotted region, close to the edge of the band, are linearly unstable. The dashed line is given by $q^2 = \varepsilon/3$ and this instability is called the Eckhaus instability [24]. Intuitively, one may understand it as follows. A wavenumber q close to the left edge of the band corresponds to a smaller total wavenumber of the pattern, and hence a larger wavelength. When the wave-vector is too small, the pattern is unstable because a roll is so wide that it will split into three. Likewise, a q near the right edge amounts to a pattern which is unstable because three narrow rolls

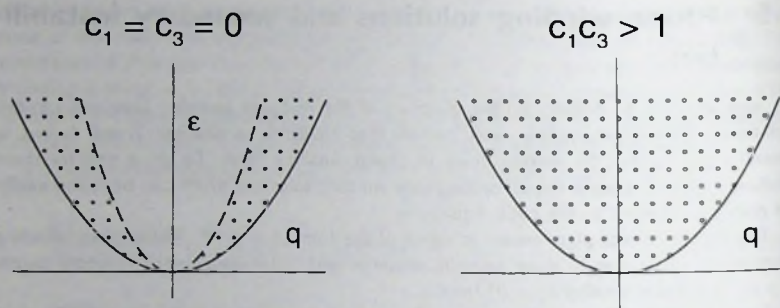


Figure 1-4. Illustration of the stability of phase-winding solutions of the one-dimensional real and complex Ginzburg-Landau equations. The stability diagram for $c_1 = c_3 = 0$ (left) and for $c_1 c_3 > 1$ (right), where the dotted areas indicate that the phase-winding solutions are linearly unstable there.

merge into one. So only patterns with wavelength close enough to the critical one are stable. This can also be understood as follows. When $q^2 \rightarrow \epsilon$, i.e. when we approach the edge of the band of allowed wavenumbers, the amplitude of the corresponding plane-wave goes to zero. When this amplitude is small enough, the linear analysis for $A = 0$ becomes more and more valid, and so at a certain point, some mode with small q , will attain a positive growth-rate. In this way the wavenumber of an Eckhaus-unstable mode relaxes to a value within the stability band, as illustrated in figure 1-5.

In the Rayleigh-Bénard system, the phase difference of Ae^{iqx} between two points, divided by 2π , is equal to the number of pairs of rolls between these two points. Thus when three rolls merge into one or when one roll splits into three, the number of phase-windings of A over a certain distance changes by one. But since the phase of A is well defined and continuous whenever $|A|$ is nonzero, the only way the number of phase-windings can change discontinuously in a localized region is if at some point in time and space $|A| = 0$. At that point the phase is undefined, and so can "slip" by 2π [25]. These points are called phase slip centers. figure 1-5 illustrates the rapid variation of the phase and the decrease in modulus $|A|$ which lead to such behavior.

For the CGLE, the stability analysis is more complicated, since one has two free parameters (c_1 and c_3) which can be adjusted. Just as in the Eckhaus instability it is found that within the range of possible phase-winding solutions, a smaller band of solutions is stable; if one leaves this band, one encounters the so-called Benjamin-Feir instability [23], which corresponds to a wave becoming unstable by resonant excitation of sidebands. This instability is analogous to the Eckhaus instability of the RGLE, but in the context of the CGLE it is usually referred to as the Benjamin-Feir instability [23]. The size of the stable band is a complicated function of c_1 and c_3 , but one important feature can be caught in

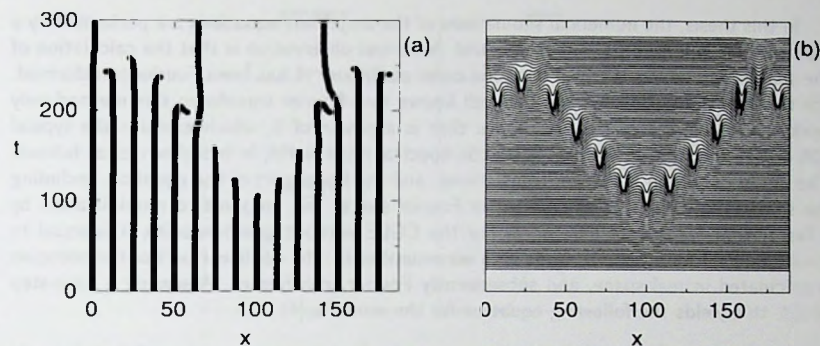


Figure 1-5. Illustration of the dynamical process by which phase-winding solutions with $|q|$ outside the Eckhaus stability band go unstable. In this example, we have taken the cubic RGLE with $\varepsilon = 0.5$ and follow the evolution of a plane-wave with wavenumber $q = 0.5$ and amplitude 0.5. A small perturbation was applied to the initial condition in order to trigger the instability. In (a) the curves in (x, t) space where the phase of A is equal to zero are traced out, while in (b) the absolute value of the amplitude is plotted. Every end of a curve in (a) corresponds to the vanishing of 2π in the total number of phase-windings of the plane-wave, and all these phase-slips clearly correspond to the occurrence of zeroes of $|A|$. In the final state, the wavenumber is decreased to 0.1.

a simple formula: If the so-called Newell criterion

$$c_1 c_3 > 1 \quad (1.5.2)$$

is valid, *all* phase-winding solutions are linearly unstable [4]! The most spectacular consequence of this will be discussed in section 1.6.2.

1.6 Beyond the phase-winding solutions.

Now that we have discussed the simple phase-winding solutions, that can be studied in an analytical framework, we should stress that, in general, solutions to the amplitude equations can not be obtained in a closed analytic form. In fact, with the exception of a few analytic solutions that have been found [11, 26], one in general has to develop other methods to gain some insight into the behavior of the amplitude equations. The derivation of an amplitude equation to describe a pattern is only one step towards the understanding of non-equilibrium patterns.

A frequently used method is, of course, the numerical simulation. In particular for the CGLE such simulations have yielded much information [4], but it should be realized that since one has at least two (c_1 and c_3) parameters and an infinity of initial conditions, such numerical explorations can never fully classify the behavior of this equation.

In this thesis, the numerical simulations of the amplitude equations are performed by a method that is known as pseudo-spectral. A central observation is that the calculation of the spatial derivatives is trivial once the order parameter A has been Fourier transformed. For this transformation, we use the well known fast Fourier transform; this method only works for a number of Fourier modes that is a power of 2, which explains the typical 256 or 512 modes that we use. A pseudo-spectral code works, in broad terms, as follows. The initial condition is Fourier transformed, and the linear part of the equation, including the spatial derivatives, is calculated; in Fourier space, this amounts to multiplication by a factor that we denote here as λ . For the CGLE without group-velocity, λ is equal to $\varepsilon - k^2(1 + ic_1)$ for a Fourier mode with wavenumber k . The nonlinear part of the equation is calculated in real space, and subsequently Fourier transformed. Assuming a time-step of Δt , this yields the following equation for the mode $u_k(t)$

$$u_k(t + \Delta t) - u_k(t) = \int_t^{t+\Delta t} ds (\lambda u_k(s) + N_k[u(s)]), \quad (1.6.1)$$

where $N_k[u(s)]$ denotes the k -th component of the Fourier transform of the nonlinear term. The integral $\int_t^{t+\Delta t} ds \lambda u_k(s)$ is approximated by $u_k(t)(e^{\lambda \Delta t} - 1)$. This approximation neglects variations of u in the time interval of the integration step due to the nonlinearity; when N is zero, it is exact. Then, the second integral $\int_t^{t+\Delta t} ds N_k[u_k(s)]$, is approximated by $\Delta t N[u_k(t + \Delta t/2)] \approx \Delta t (3/2 N_k[u_k(t)] - 1/2 N_k[u_k(t - \Delta t)])$. With this approximations, u_k can be stepped forward in time, and this procedure (that is known as semi-implicit) can be shown to have second order accuracy in Δt .

The study of non-equilibrium patterns and amplitude equations is a combination of exact and perturbation theories, numerical exploration and intuition. Many aspects of the amplitude equation are known only in a mathematically non-rigorous sense. Typical examples of hybrid efforts to understand behavior of the amplitude equations are shown in chapter 3 and 4. In chapter 3, a simple exact result on the existence and stability of single and bimodal states in coupled amplitude equations inspires the question what happens when both these states are present and separated by a domain-wall. In a certain limit of a particular simplified model, an exact result on the existence of such a domain-wall is obtained. For a more complicated model, this result can not be proven to be correct, but under certain conditions we find, by numerical methods, that it is relevant. To study the effect of the coefficients on this domain-wall, we merely explore some areas of the parameter space of the coupled CGLE's, and our conclusions are in this case only qualitative.

In many dynamical states, we see the occurrence of more or less sharply defined local structures that seem to govern important aspects of the dynamics. In chapter 4 we explore the behavior of one of these local structures numerically in a model equation, and find that a transition between ordered and disordered behavior can be described by simple analytical terms for this model equation. In fact the transition should occur under general conditions, and so the study of a model equation can lead to insight of more general equations.

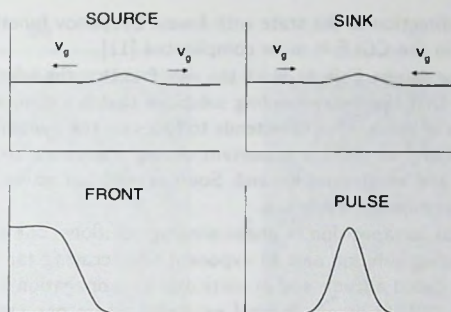


Figure 1-6. Schematic representation of coherent structures of the one-dimensional complex amplitude equation.

1.6.1 Coherent structures.

When $c_1 c_3 < 1$, one often finds that part of the dynamics of the CGLE is governed by well-defined regular solutions which we will refer to as coherent structures (some of them also exist in the RGLE). Coherent structures are solutions that are either themselves localized or that consist of domains of regular patterns connected by localized defects or interfaces. It is important to understand the existence and stability of these coherent structures as a first step towards an analysis of the dynamics of more complicated patterns. We shall now, for further reference, give a very brief overview of what kind of coherent structures do exist. All the solutions we shall discuss are uniformly translating, i.e., are solutions of the CGLE of the form

$$A(x, t) = e^{-i\omega t} \hat{A}(x - vt). \quad (1.6.2)$$

Let us first consider solutions which connect one phase-winding solution on the left to another one on the right. We will call them domain-wall or shock type solutions. Since a traveling wave has a nonzero group-velocity v_g , there are several possibilities depending on whether the group-velocity of each phase-winding solution points away from or towards the localized structure connecting the two asymptotic states. It is useful to use the group-velocity \tilde{v}_{gr} relative to the velocity v of the localized structure $\tilde{v}_g := v_g - v$. Thus \tilde{v}_{gr} is the velocity of a small perturbation of a phase-winding solution in the frame moving with the domain-wall. If the relative group-velocity points away from the localized structure on both sides, the latter has the properties of a *source*, while if \tilde{v}_{gr} points inwards on both sides, we will call the domain-wall a *sink* [11, 27]. In principle, solutions with the relative group-velocities pointing in the same direction on both sides of the wall might also be possible, but one can show [11] that such solutions do not exist in the cubic CGLE. They do, however, exist in higher-order extensions, such as the quintic CGLE. In the RGLE, most of the dynamics of domain-walls can be understood in terms of the tendency of

walls to move in the direction of the state with lowest Lyapunov functional. The behavior of sinks and sources in the CGLE is more complicated [11].

Sinks are in a sense passive objects, since the very fact that the relative group-velocities point inwards means that the phase-winding solutions that are connected must originate in some other regions of space. One then tends to focus on the dynamics in these regions. Nevertheless, the velocity of sinks is important during transients because it determines which regions shrink and which ones expand. Sources send out waves, and so may determine the large-time asymptotic dynamics.

Instead of a spatial juxtaposition of phase-winding solutions, one often has a juxtaposition of a phase-winding solution and an exponentially decaying tail, as shown in figure 1-6. This structure is called a front, and in particular its propagation has been the subject of intense study [28, 29]. In many physical examples where one state invades another state, a description in terms of fronts is appropriate. The behavior of fronts in the CGLE will be discussed in more detail in chapter 4.

Now that we have seen examples of coherent structures formed by the juxtaposition of infinite-size solutions, we should mention one other very important coherent structure, the so-called pulses, as shown in figure 1-6. Although at first glance these pulses look similar to solitons [21], it should be noted that the amplitude equations do not have a Hamiltonian structure in general. Pulses are connected to solitons in the sense that when an equation possessing solitons is perturbed, a usually smaller set of pulse-like solutions emerges. Pulses play an important part in the dynamics in the bistable regime around a subcritical bifurcation [11].

We postpone a further discussion on fronts and pulses to chapter 4, where we will study their interaction in an extension of the quintic CGLE.

1.6.2 Spatio-temporal chaos.

It was found by Shraiman *et al.* [30] that two, qualitatively different *spatio-temporally chaotic* states occur when the Newell criterion (1.5.2) $c_1 c_3 > 1$ is valid, and this discovery inspired many workers to investigate these so-called phase-chaos and defect-chaos states [10]. In contrast to the low dimensional temporal chaos, spatio-temporal chaos is far from being understood, despite a rapid growth of the literature over the last years [4]. In this thesis we will not go into any of the details of this fascinating subject. However, the fact that by merely changing the parameters of the CGLE one can get from purely variational to chaotic behavior, is one of the major motivations for the calculations carried out in chapter 2. Therefore, we will restrict ourselves to showing two examples of the beautiful and rich states that occur in the CGLE when the Newell criterion is valid.

These states were obtained by numerical simulations of the CGLE with a pseudo-spectral code. The number of Fourier-modes was 512, and we fixed the system size at 300. The linear growth-rate ε was fixed at a value of 1, and we use as initial condition a plane-wave state with a small, and slowly varying wavenumber: $A(x) = \exp(2i \sin(2\pi x/300))$.

As a first example, we take $c_1 = 3$ and $c_3 = 0.6$. For these values of the coefficients so-called phase-chaos (to be explained below) occurs [30], and this is shown in figure 1-7.

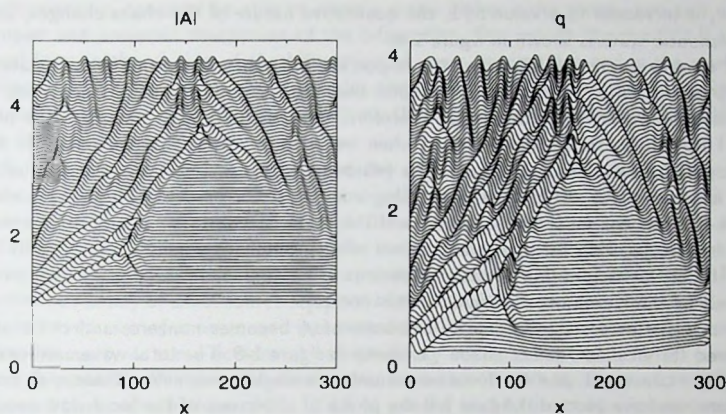


Figure 1-7. Amplitude and local wavenumber (see text) for a phase-chaos state of the CGLE. The total time duration of this simulation was 750. Subsequent snapshots have a time difference of 10, and where shifted upward over a distance of .05. Since the average value of A is of order one (see left panel), the fluctuations in A are small.

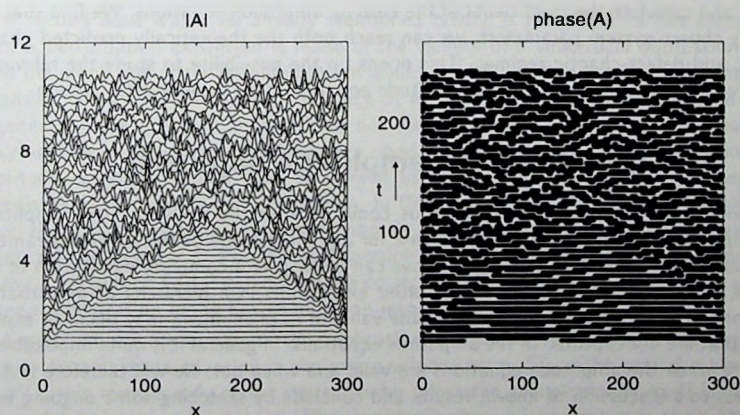


Figure 1-8. Amplitude and phase of A for a defect-chaos state of the CGLE. The total time duration of this simulation was 250, and subsequent snapshots have a time difference of 5. In the right panel, the phase of A is drawn in black when it is between 0 and π . Note that there are many phase-slips present.

When c_1 is increased to a value of 1, the qualitative nature of the chaos changes, and a typical chaotic state is shown in figure 1-8.

Let us now briefly explain what the important difference between the two states is. In the phase-chaotic regime, $|A|$ is bounded away from zero, and as a consequence, the total wavenumber of A is conserved. Therefore, the essential chaos occurs in the phase of A . This can be shown most clearly when we introduce the local wavenumber of A as the spatial derivative of its phase. The left panel of figure 1-7 shows the fluctuations in the absolute value of A , that are of the order of a few percent. The right panel of figure 1-7 shows the local wavenumber, and this state is seen to be clearly disordered. It should be stressed that this is not a transient effect; the chaos persists for arbitrarily long times. Under the assumption that the variations of $|A|$ are small, the phase-chaos can be described by the Kuramoto-Sivashinsky equation [4].

When c_1 is increased, the density of zeroes of A becomes nonzero, and the ensuing disordered state called "defect-chaos", is shown in figure 1-8. The total wavenumber of A is no longer conserved, and the local wavenumber is singular whenever phase-slips occur. Therefore, we have plotted in figure 1-8 the phase of A instead of the local wavenumber. Apart from the obvious difference in densities of defects, many properties of these states are unknown. For the one-dimensional CGLE, the location in parameter space where the transition between phase-chaos and defect-chaos occurs seems to depend on system-size; in fact, the question whether phase-chaos persists for asymptotically large system sizes and times is currently under debate [10].

In chapter 2 we will describe rotating Rayleigh-Bénard system that is described by the CGLE, and calculate the coefficients of the ensuing amplitude equations. We find that for suitably chosen system parameters, we can reach both the theoretically predicted phase-chaotic and defect-chaotic regimes. This opens up the possibility to study the relevance of the various chaotic states in the amplitude equation in an experimental system.

1.7 The validity of the amplitude approach.

In closing this introductory chapter let us come back to the validity of the amplitude equations. As with any perturbation theory, for any finite value of the control parameter ε , the amplitude equations as derived above can never give a complete description of the physics, since they are only the lowest order expressions in a hierarchy of perturbation equations. It is therefore clear that for some value of ε , phenomena may occur in experiments that are not captured in the amplitude equations. In general it is quite impossible to estimate when the amplitude equations are valid and when not; we will therefore restrict ourselves to a discussion of known results and conclude by sketching some ongoing work on the validity of coupled amplitude equations.

First of all, we remind the reader of the concept of normal forms [15], that is well known in the bifurcation theory of low dimensional dynamical systems. The basic idea is very simple. Suppose we have made an expansion around a bifurcation point, in which possibly many small, higher order terms arise. The choice of coordinates is of course immaterial for the nature of the bifurcation, so by performing a series of nonlinear coordinate

transformations, one may be able to remove many higher order terms, and end up with a simpler and universal description of the bifurcation. One would like the CGLE to be a normal form in the vicinity of the bifurcation. A more modest demand is the qualitative persistence of the dynamical behavior under perturbations of the amplitude equation [16]. This is not true as can be shown by studying the behavior of the so-called Nozaki-Bekki holes [31], as described below.

On the basis of an analysis of the ordinary differential equations that can be derived for the function \hat{A} in equation (1.6.2) one generically expects the existence of a $v = 0$ source, as well as a *discrete set* of $v \neq 0$ sources [11]. In other words, one expects that in addition to the $v = 0$ solutions there are only sources with particular values of the velocity and asymptotic wavenumbers. Surprisingly, however, Bekki and Nozaki [31] found a *continuous family* of exact source solutions of the CGLE. The existence of a family rather than a discrete set of sources was interpreted [11] as a hint that there might be some hidden symmetry or some accidental non-genericity in the cubic CGLE for all parameter values. Support for this point of view comes from recent work by Popp *et al.* [32], who discovered that perturbations of the CGLE in general lead to a monotonic acceleration or an oscillation of these holes. Recently, Lega *et al.* [33] observed holes reminiscent of the Bekki-Nozaki type solutions in a low Prandtl number convection experiment.

Although this issue is still not resolved to full satisfaction, it is a clear warning that small symmetry breaking terms can be important in the understanding of experimentally observed patterns that the bare CGLE can not account for. For a more extensive overview of results on the validity of the CGLE the reader may consult the papers by Eckhaus [34].

A second issue which we already mentioned briefly, is the problems one encounters when a perturbation expansion is made in the vicinity of a subcritical bifurcation. Only when the amplitude of the ensuing pattern would be of the right order in ε , and amplitude expansion could yield an equation in which at least all the terms are of the same order. In general this is not true, in particular not for the binary liquid convection where the subcritical Hopf bifurcation has been described by a quintic CGLE. In our opinion, the amplitude equations should then be viewed as toy-models, that capture the essential ingredients of the pattern forming system. In this case, the quintic CGLE is the simplest model that has the essential ingredients, namely a subcritical bifurcation towards traveling waves, with both linear and nonlinear dispersion present. For the binary liquid convection however, the quintic CGLE can not be the correct amplitude equation since in this system a low concentration mode has to be taken into account [35].

A problem one encounters in the application of the complex Ginzburg-Landau equations as an amplitude equation is the group-velocity term. Since the spatial scale scales like $\varepsilon^{1/2}$, this term is only of the correct order when the group-velocity itself is of order $\varepsilon^{1/2}$, which is in general not true. When we study plane-waves, one may argue that the group-velocity only works on the dispersion relation and reflects the dispersion relation of the underlying equations of motion. In this case, we tend to believe that the group-velocity terms does not pose a serious problem. For solutions where the absolute value of the amplitude is not constant, this no longer is true, and in our opinion the effect of the group-velocity is poorly understood. In this respect, it would be nice if experiments

could be conducted to verify whether the results of chapter 3, dealing with the effect of a group-velocity on inhomogeneous solutions of coupled amplitude equations, have any meaning for experimental systems.

Finally, we would like to briefly discuss an issue that we are currently interested in, but that falls beyond the scope of this thesis. This work was initiated by the desire to describe some experiments performed by Alvarez [36], concerning the motion of sinks in a background of traveling waves. The experimental setup consists of a thin wire, that is heated just below a fluid-surface, and this system favors single-mode states, and as a result, the system shows a juxtaposition of left- and right-traveling waves, connected by sinks. The wavenumber and frequency of the traveling waves occur within a band of values and the experimentally observed motion of the sinks is empirically given in terms of the traveling waves that lie on opposite sides of the hole. This propagation rule is that no phase-slips should occur; the phases of the right- and left-traveling waves are seen to cross over smoothly. This gives as a velocity for the sink $\Delta\omega/\Delta q$, where $\Delta\omega$ is the difference in frequencies and Δq is the difference in wavenumbers between the left- and right-traveling waves.

However, such a simple, experimentally relevant and intuitively clear rule *can not be implied in an amplitude approach!* The reason for this is simple; the aforementioned wavenumbers and frequencies are those of the *pattern* and not those of the waves that occur in the amplitude equations. Since the amplitude equations do not include information on the critical wavenumber and frequency of the underlying physical system, they can never implement the propagation rule. In the near future, we will try to see whether this problem with the amplitude approach can be solved by including non-adiabatic terms similar to those of the work of Bensimon *et al.* [5].

In a sense this problem is related to the problems with the group-velocity terms because in both cases the bare critical wavenumber and frequency of the underlying pattern play a role. However, since the group-velocity is equal to the derivative of critical frequency with respect to wavenumber, and the last problem is connected with the value of the critical wavenumber alone, these two problems can arise independently.

After all this criticism on the amplitude approach, it is not more than fair to remark that at this moment it is virtually the only means of description that we have for pattern forming systems. Without amplitude equations, it is quite unlikely that we could have ever gone beyond an essentially linear analysis of the patterns. Also, the similarities between the patterns and phenomena occurring in many different systems can only be understood in an amplitude equation framework. For an overview of many successful comparisons between experiments and amplitude descriptions, the reader may consult the review paper by Cross and Hohenberg [4]. However, whenever one studies a certain physical pattern forming system, one should bear in mind that an amplitude equation is more like a starting point than an end point of the analysis.

2 Rayleigh-Bénard convection in a rotating annulus.

The coefficients of the coupled cubic CGLE's that arise for Rayleigh-Bénard convection in a rotating annulus are calculated. This work is motivated by the observation that in the presence of vertical boundaries, a forward bifurcation towards traveling waves occurs in rotating Rayleigh-Bénard convection [37, 38]. Therefore the amplitude equations are cubic CGLE's, and they should give a precise description of patterns just above onset, in contrast to the much studied case of convection in binary liquids where the bifurcation is subcritical [4, 39] (see chapter 1 and 4). The coefficients of the amplitude equations depend, in principle, on the rotation-rate of the convection cell, such that this system is an experimental realization of the cubic CGLE with tunable coefficients [40]. This is an additional advantage over binary liquid convection, where the coefficients can be changed by a change of the convection fluid [41], but where the adjusted in the coefficients is difficult to predict. We calculate the coefficients for the amplitude equations and search for system parameters such that in a single experiment one can, by adjusting the rotation-rate, scan from a regime of essentially coherent patterns to a regime of spatio-temporal chaos. For a suitable chosen convection fluid with Prandtl number (see chapter 1) of the order of 0.15, our calculations show that this is possible.

2.1 Introduction.

When a Rayleigh-Bénard convection-cell is rotated along a vertical axis, the Coriolis force introduces new phenomena. In an infinite layer, this can easily be seen from the dispersion relation [3]. When the Prandtl number is sufficiently small, the initial bifurcation is towards traveling waves, in contrast to the stationary patterns observed in ordinary Rayleigh-Bénard convection, and this has been attributed to a symmetry breaking that is induced by the rotation [42]. Rayleigh-Bénard convection in *finite* rotating systems has recently been the focus of several studies [37, 38, 40, 43]. It was discovered that in rotating cylinders an oscillatory bifurcation towards a traveling wall-mode can occur *for arbitrary values of the Prandtl number* σ . The traveling waves that may occur for sufficiently small Prandtl numbers in infinitely large rotating fluid-layers are extended throughout the system [3], and we will refer to these modes as bulk-modes. When vertical boundaries are introduced, wall-modes do occur, that have their wavenumber parallel to the side-wall and that decay exponentially perpendicular to the side-wall [40, 43]. In a rotating annulus, there are two of these quasi one-dimensional wall-modes, localized, respectively, near its inner and outer side-walls. Apart from these wall-modes, finite size modifications of the aforementioned bulk-modes play a role for sufficiently small values of σ [43].

The first experiments that we are aware of that showed the existence of these wall-

modes were performed by Zhong *et al.* [37]. Their main focus was on the strong nonlinear states that occurred for high Rayleigh numbers. Ning and Ecke [38] then performed experiments in a cell of aspect ratio 1 and for moderate Rayleigh numbers, and measured the critical Rayleigh number, frequency and wave-vector of the wall-modes for a range of rotation-rates. Buell and Catton [44] had performed calculations for such a system, but they had assumed the bifurcation to be stationary, so their results were inconsistent with the experiments. Therefore, Goldstein *et al.* [43] performed a correct linear stability analysis and it was found that they could reproduce the results of the measurements on the wall-modes well. The wall-modes are generated via a forward bifurcation, and so in the vicinity of this bifurcation the modulations of the wall-mode can be described by a single one-dimensional complex Ginzburg-Landau equation. Since the rotation-rate can be easily adjusted in experiments, this could in principle give an experimental realization of the CGLE where the coefficients can be tuned along a one-dimensional sub-manifold of parameter-space, as desired. In particular, it was expected that for low rotation-rates, one essentially has the RGLE, whereas for higher rotation-rates one would tune away from this dissipative limit.

Kuo and Cross [40] calculated the coefficients for such a CGLE, in the limit that the radius of the cylinder goes to infinity. Their system can be viewed as a semi-infinite rectangular cell with a Coriolis force added to account for the rotation. The single boundary is sufficient to break the translational invariance and to generate the wall-mode. The large radius limit has as an advantage over finite size cylinders that the analysis in a rectangular system is technically less involved than in a cylindrical geometry. Moreover, the wavenumbers are not discretized, as is the case in a cylindrical geometry. Kuo and Cross found that the coefficients of the CGLE show only a weak dependence on the rotation-rate, in particular for high rotation-rates, and that the c 's of the CGLE are close to the relaxational limit ($c_1 \approx -c_3$).

It should be noted that all of the papers cited above, with the exception of the papers by Goldstein *et al.* [43], focus on convection in water, which has a high Prandtl number ($6 \sim 7$). We recover for the annulus the result of Kuo and Cross [40], that for such Prandtl numbers the coefficients of the CGLE have only a weak dependence of the rotation-rate, and are in the relaxational regime. In order to move away from this rather dull behavior, we extend the previous work in two directions. First of all, we include calculations for lower Prandtl numbers. Secondly, we take an annulus of large radius as our geometry. The width of the annulus is an extra adjustable parameter, besides the Prandtl number and the rotation-rate. This geometry has the advantage over the half plane geometry of Kuo and Cross that bulk-modes are quasi one-dimensional and can be described by the same amplitude equations as the wall-modes. The disadvantage is that because of the boundary conditions that need to be satisfied at both the inner and outer vertical side-wall, the calculations become technically more involved.

We calculate the linear onset values for the various modes, concentrating on the relevant ones, i.e., the ones with lowest critical Rayleigh number. The critical Rayleigh numbers of the bulk- and wall-modes are in general sufficiently different, so the amplitude equations describing slow modulations of the relevant modes in the co-rotating reference

frame are two coupled complex Ginzburg-Landau equations [4], one for the left- and one for the right-traveling waves. For the bulk-mode, the cross-coupling coefficient g_2 is sufficiently large to render the bimodal states unstable, and in this case a single amplitude equation description suffices (see chapter 1). If the width of the channel is large, the two wall-modes are almost indistinguishable from the single wall-modes of Kuo and Cross. When the width of the channel is decreased, the interaction between these two wall-modes increases. The coupling strength between the two CGLE's for the wall-modes depends on the width of the channel. We calculate the coefficients of the amplitude equations for this system, for various Prandtl number, rotation-rate and width of the annulus. For $\sigma \geq 0.2$, the wall-modes have the lowest critical Rayleigh number, but their coefficients show only a weak dependence on the system parameters and since $c_1 \approx -c_3$, their behavior is almost relaxational (see Chapter 1). For Prandtl number in the range of $0.1 \sim 0.2$, the bulk-mode has lowest critical Rayleigh number, and in this case the coefficients of the amplitude equations can be tuned over a wide range as a function of the rotation-rate.

This chapter is organized as follows. First of all, we describe the equations of motion for this system and the methods to derive the linear onset values and the coefficients of the amplitude equations. Then we present the various sets of data that are obtained by these methods. The first part of this presentation concerns a Prandtl number of 6.7 and the second part concerns a Prandtl number of 0.15. The range over which the coefficients c_1 and c_3 vary as a function of the rotation-rate is shown for this two Prandtl numbers in figure 2-4.

2.2 Equations of motion.

The hydrodynamic equations describing a rotating fluid-system are the Navier-Stokes equation supplemented with the heat equation and the mass conservation law as discussed in Chapter 1, supplemented with the centrifugal force due to the rotation. Of course we write the equations in the co-rotating frame and this yields an additional Coriolis force [3]. The centrifugal force is given by $\vec{\nabla}^2 \frac{1}{2} |\vec{\Omega}_D \times \vec{r}|^2$ and effectively tilts the gravity vector. This gives a coupling term between the temperature dependent density and the effective gravity of the form $-g\alpha T \hat{z} + \alpha T \vec{\nabla}^2 \frac{1}{2} |\vec{\Omega}_D \times \vec{r}|^2$, where the first term is the standard buoyancy term of the Boussinesq approximation (see section 1.2.1). We would like to neglect the second term, and we therefore assume that the centrifugal force can be neglected with respect to the gravitational force, i.e., $|\vec{\Omega}_D^2 \tau / g| \ll 1$. In a strict infinite annulus, where $\tau \rightarrow \infty$, this can not be true, so an experimental setup should be a compromise between the requirement that the centrifugal force can be neglected in comparison to the gravitational force, and the demand that the radius of the annulus τ is large to make finite size curvature corrections as small as possible. In practice, Ω_D is of the order of 1 rad/s, and the radius τ is of the order of a few cm's [37], so the centrifugal forces can usually be neglected. Assuming this to be the case, the equations of motion for the velocity v , temperature T

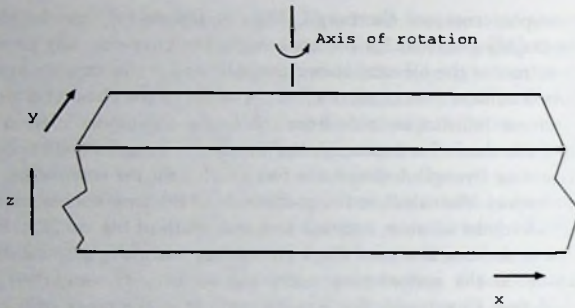


Figure 2-1. The geometry of the physical system. Please note, that because we neglect centrifugal forces, the location of the center of rotation is arbitrary.

and pressure P in the Boussinesq approximation are:

$$(\partial_t + \vec{v} \cdot \vec{\nabla})\vec{v} = -\vec{\nabla} \frac{P}{\rho} + \nu \nabla^2 \vec{v} - g\alpha T \hat{z} + \vec{\nabla} \cdot \frac{1}{2} |\vec{\Omega}_D \times \vec{r}|^2 + 2\vec{v} \times \vec{\Omega}_D, \quad (2.2.1a)$$

$$(\partial_t + \vec{v} \cdot \vec{\nabla})T = \kappa \nabla^2 T, \quad (2.2.1b)$$

$$\vec{\nabla} \cdot \vec{v} = 0. \quad (2.2.1c)$$

As before, ρ is the mean fluid-density, ν the kinematic viscosity, g the gravity, α the thermal expansion coefficient, Ω_D the angular velocity and κ the thermal conduction coefficient. The Coriolis force density is given by $2\vec{v} \times \vec{\Omega}_D$. We will denote the vertical coordinate by z , the coordinate along the circumference of the annulus x , and the coordinate in the radial direction by y as indicated in figure 2-1.

When there is no fluid motion, $\vec{v} = 0$ and $T = T_0 - z/(d\Delta T)$, where T_0 is the temperature of the bottom plate at $z = 0$, ΔT the temperature difference between lower and upper plates of the convection cell and d the height of the fluid-layer. When we denote perturbations of the temperature from this homogenous, quiescent state by θ , we obtain:

$$(\partial_t + \vec{v} \cdot \vec{\nabla})\vec{v} = -\vec{\nabla} \left(\frac{P}{\rho} - \frac{1}{2} |\vec{\Omega}_D \times \vec{r}|^2 \right) + \nu \nabla^2 \vec{v} - g\alpha \theta \hat{z} + 2\vec{v} \times \vec{\Omega}_D, \quad (2.2.2a)$$

$$(\partial_t + \vec{v} \cdot \vec{\nabla})\theta = \kappa \nabla^2 \theta + \frac{\Delta T v_z}{d}, \quad (2.2.2b)$$

$$\vec{\nabla} \cdot \vec{v} = 0, \quad (2.2.2c)$$

where we absorbed the buoyancy force that results from the quiescent solution into the pressure.

Taking the rotation of equation (2.2.2a) to eliminate the pressure and centrifugal force, and scaling length by d , time by d^2/κ and temperature by ΔT (note that this

scaling is different from the one used in chapter 1), we obtain the non-dimensionalized equations of motion we will use in the following:

$$\vec{\nabla} \times \left(\left(\frac{1}{\sigma} \partial_t - \nabla^2 \right) \vec{v} - R\theta \hat{z} - 2\Omega \vec{v} \times \hat{z} \right) = \vec{\nabla} \times \left(-\frac{1}{\sigma} (\vec{v} \cdot \vec{\nabla}) \vec{v} \right), \quad (2.2.3a)$$

$$(\partial_t - \nabla^2) \theta - v_z = -(\vec{v} \cdot \vec{\nabla}) \theta, \quad (2.2.3b)$$

$$\vec{\nabla} \cdot \vec{v} = 0, \quad (2.2.3c)$$

where Ω is used as the dimensionless rotation-rate. The Rayleigh number R is given by $g\alpha\Delta T d^3/\kappa\nu$. Although equation (2.2.3a) has three components, only two of these components are required in subsequent calculations because of the rotation operator on the left- and right-hand side of this equation. As we will show below, our calculations are notably simplified if we drop the z -component of (2.2.3a). We rescale the width of the channel by the depth of the fluid-layer d , and refer to the ensuing aspect ratio as Γ_y . The physical fields \vec{v} and θ shall be represented by one vector quantity $U = (v_x, v_y, v_z, \theta)$ and $\vec{\nabla}$ represents $(\partial_x, \partial_y, \partial_z)$. We write the equations of motion, with instead of (2.2.3a) the x and y component of that equation as:

$$\mathcal{L} \cdot U = \mathcal{N}(U, U), \quad (2.2.4)$$

where \mathcal{L} is the linear part, and \mathcal{N} contains all the nonlinear terms. When we define $D := (\partial_t/\sigma - \nabla^2)$, then

$$\mathcal{L} = \begin{pmatrix} \partial_x & \partial_y & \partial_z & 0 \\ 0 & 0 & -1 & \partial_t - \nabla^2 \\ -2\Omega\partial_z & -D\partial_z & D\partial_y & -R\partial_y \\ D\partial_z & -2\Omega\partial_z & -D\partial_x & R\partial_x \end{pmatrix}, \quad (2.2.5)$$

$$\mathcal{N}(U, U) = \begin{pmatrix} 0 \\ -(\vec{U} \cdot \vec{\nabla})\theta' \\ -1/\sigma(\partial_y(\vec{U} \cdot \vec{\nabla})U'_z - \partial_z(\vec{U} \cdot \vec{\nabla})U'_y) \\ -1/\sigma(\partial_z(\vec{U} \cdot \vec{\nabla})U'_x - \partial_x(\vec{U} \cdot \vec{\nabla})U'_z) \end{pmatrix}. \quad (2.2.6)$$

Choosing appropriate boundary conditions is a key issue in many convection studies [3, 4, 45]. The boundary conditions should be as close as possible to the physical situation, which would imply the use of "stick" or rigid boundary conditions ($v = 0$) on both the horizontal and vertical boundaries. However, these boundary conditions force one to consider partial differential equations in the (y, z) -plane, that in general can only be solved by numerical procedures. Applying "slip" boundary conditions, i.e., requiring that both the normal components and the normal derivative of v are zero, allows one to separate the y and z part of the equations of motion [3], and therefore one only has to consider ordinary differential equations. In this problem, this separation can be carried out when the top and bottom plate have slip boundary conditions and the vertical side-walls have the rigid boundaries. This was the strategy followed by Kuo and Cross [40] and we will follow them, so our boundary conditions are:

$$v_x = v_y = v_z = \partial_y \theta = 0 \quad \text{on } y = 0, \quad \Gamma_y. \quad (2.2.7a)$$

$$\partial_x v_x = \partial_z v_y = v_z = \theta = 0 \quad \text{on } z = 0, \quad 1. \quad (2.2.7b)$$

Although the free slip conditions are not the physical conditions, it has been shown [43], in particular for large rotation-rates, that the critical Rayleigh number, frequency and wavenumber are not very different from their values in a system with rigid boundary conditions on the vertical plates. This is because for rigid boundary conditions and high rotation-rates, there exists a thin so-called Ekman boundary layer [40], outside of which the physical fields are close to the fields in the slip boundary case [45, 46]. The effect of the boundary conditions on the (nonlinear) coefficients of the amplitude equation is not known. If, in the future, large deviations between theory and experiment would occur for these coefficients, calculations with better implemented boundary conditions may be required. One should be warned, however, that these calculations are likely to be extremely laborious.

2.3 Linear stability analysis.

In this section we will describe, in considerable detail, how we extract the linear onset values from the equations of motion. In principle, this amounts to a straightforward stability analysis. In practice, one encounters a reasonable amount of details and (numerical) subtleties, and we discuss the most important of those below.

The invariance of the problem under translations in the x and t directions allows us to write a single mode solution of the linearized equations $\mathcal{L}u_0 = 0$ (see equation (2.2.6)) as

$$e^{i(-kx+\omega t)+st} \bar{U}(y, z) + \text{c.c.} \quad (2.3.1)$$

The linear stability of a certain mode is determined by the sign of the growth-rate s and the bifurcation from a conducting to a convecting state occurs when the first mode goes unstable upon increasing R . The free slip boundary conditions on $z = 0, 1$ allow for the separation of $\bar{U}(y, z)$ such that the z -dependence has a simple form:

$$u_0 = e^{i(-kx+\omega t)+st} \begin{pmatrix} \cos(\pi z) & W_1(y) \\ \cos(\pi z) & W_2(y) \\ \sin(\pi z) & W_3(y) \\ \sin(\pi z) & W_4(y) \end{pmatrix} + \text{c.c.} \quad (2.3.2)$$

By substituting this ansatz, which satisfies the boundary conditions (2.2.7b), into the linearized equations $\mathcal{L}u_0 = 0$, one finds that this z -dependence indeed allows for the separation of the linearized equations. This is the reason why slip boundary conditions are often used. In contrast, for stick boundary conditions, a simple ansatz will not be sufficient to satisfy both the boundary conditions and to separate the linearized equations of motion. As a final note on the form of the linear modes it should be noted that "harmonics" where the $\cos(\pi z)$ are replaced by $\cos(2\pi z)$ (similar for the \sin functions) also satisfy the boundary conditions and separate the linearized equations of motion. Such a mode corresponds to the vertical stacking of convection rolls, and based on experiments and physical intuition one expects these modes never to be relevant for the linear analysis

of the primary bifurcation from the conducting state. However, when we will perform the amplitude expansion for the full equations of motion (including nonlinearities), such a z -dependence will occur for the higher order terms that are slaved by the primary mode (see equation (2.4.25)).

Since the equations of motion are real valued, the existence of a solution with wavenumber k and frequency ω implies the existence of a complex conjugated solution that has wavenumber $-k$ and frequency $-\omega$. These two solutions together form only one convection mode. When ω and k have equal sign and u_0 is written in the form of equation (2.3.2), this corresponds to a right-traveling mode.

An important feature of the infinitely large rotating annulus is the symmetry that relates the left- and right-traveling waves. When the boundary conditions (2.2.7) are applied, the rotation symmetry present in the fluid-equations is broken and only an 180° rotation symmetry remains. Therefore, the convection modes come in pairs; apart from the right-traveling mode with wavenumber $\pm k$ and frequency $\pm\omega$ there is a left-traveling mode with wavenumber $\pm k$ and frequency $\mp\omega$. This mode has the same z -dependence as the right-traveling mode and a y -dependence \bar{W}_i that satisfies $\bar{W}_i(y) = W_i(d - y)$. This symmetry implies that left- and right-traveling modes have the same critical parameters. However, in an experiment where the convection cell is an annulus of finite radius, this symmetry is broken. In principle, one could carry out a perturbation theory to calculate the effect of a finite curvature, but we will not study this. One could conceive experiments in an rotating straight channel; as long as the centrifugal forces can be neglected, the center of rotation doesn't play a role. However, the extra boundary conditions can lead to other problems, and therefore an annular geometry is preferred.

The linear onset values ω_c , k_c and R_c follow from the lowest value of R for which equation (2.3.1) has solutions for which s goes from negative to positive values when R is increased. To obtain the linear onset values, one first calculates the $W_i(y)$ as follows. When we set s equal to zero and substitute ansatz (2.3.2) into the linearized equations of motion, we obtain an 8-th order ordinary differential equation for the functions $W_i(y)$, which can be rewritten as the ordinary differential equation $\partial_y w = Lw$. The vector w describes the physical fields W_i and is given by

$$w = \begin{pmatrix} \partial_y W_1(y) \\ W_2(y) \\ \partial_y W_2(y) \\ \partial_y^2 W_2(y) \\ W_3(y) \\ \partial_y W_3(y) \\ \partial_y^2 W_3(y) \\ W_4(y) \\ \partial_y W_4(y) \end{pmatrix}. \quad (2.3.3)$$

Note that $W_1(y)$ does not occur in this representation of the linearized equations of motion; however, the equation of continuity (2.2.1c) yields $-ikW_1 + \partial_y W_2 + \pi W_3 = 0$, and from this relation $W_1(y)$ can be obtained. The matrix L depends on σ , k , ω , Ω and

R , and its explicit form is:

$$\begin{pmatrix} 0 & -2\Omega & \frac{\beta}{ik} & \frac{\beta\pi}{ik} - \frac{\beta ik}{\pi} & 0 & \frac{ik}{\pi} & \frac{Rik}{\pi} & 0 \\ 0 & 0 & 1 & 0 & 0 & 0 & 0 & 0 \\ ik & 0 & 0 & 0 & -\pi & 0 & 0 & 0 \\ 0 & 0 & 0 & 0 & 1 & 0 & 0 & 0 \\ 0 & 0 & 0 & 0 & 0 & 1 & 0 & 0 \\ -ik\pi & \pi\beta & \frac{2\Omega\pi}{ik} & \frac{2\Omega\pi^2}{ik} & \pi^2 + \beta & 0 & 0 & -R \\ 0 & 0 & 0 & 0 & 0 & 0 & 0 & 1 \\ 0 & 0 & 0 & -1 & 0 & 0 & \alpha & 0 \end{pmatrix}, \quad (2.3.4)$$

where $\alpha := i\omega + k^2 + \pi^2$ and $\beta := i\omega/\sigma + k^2 + \pi^2$ (α should not be confused with the thermal expansion coefficient).

In terms of the components of w , the boundary conditions are

$$w_2 = w_3 = w_4 = w_8 \text{ on } y = 0, \Gamma_y. \quad (2.3.5)$$

The conditions on w_2, w_4 and w_8 follow directly from the boundary conditions (2.2.7b); the boundary condition on $W_1 = -1/(ik)(\partial_y W_2 + \pi W_3)$ yields the condition on $w_3 (= \partial_y W_2)$.

Let us first assume that the eigenvectors of L are non-degenerate. The set of ordinary differential equations then has solutions of the form

$$w^j = \sum_{i=1}^8 a_i h_i^j e^{\lambda_i y}, \quad (2.3.6)$$

where h_i^j is the j -th component of the i -th eigenvector of L and λ_i is the corresponding eigenvalue. The eigenvalues come in pairs $(-\lambda, \lambda)$ and this can be understood as follows. These eigenvalues are calculated before the boundary conditions on $y = 0, \Gamma_y$ are applied. Without these boundary conditions, the equations of motion are symmetric with respect to rotations in the (x, y) -plane, and so are their solutions. In such an infinite system, the $W_i(y)$ dependence is simply of the form $e^{\lambda y}$, where λ should be purely imaginary. The rotation symmetry dictates the dispersion relation to be a polynomial in $\lambda^2 - k^2$. When we apply the boundary conditions, the λ 's are no longer purely imaginary, but the secular equation of L is still a polynomial in $\lambda^2 - k^2$; for fixed k , the solutions to this equation, i.e., the eigenvalues, should come in pairs $(-\lambda, \lambda)$. Note that this is completely consistent with the symmetry between left- and right-traveling modes.

The coefficients a_i in equation (2.3.6) are determined by applying the boundary conditions on $y = 0, \Gamma_y$ to solutions of the form (2.3.6), which yields an equation of the



Figure 2-2. Illustration of the problem induced by the degeneracy of the eigenvectors h_i . For system parameters $\sigma = 0.5$, $\Omega = 100$ and $\Gamma_y = 1$ and wavenumber 5, we have plotted, from left to right, the absolute values of $\det(M)$, $\det(h)$ and $\chi := \det(M)/\det(h)$ respectively, as a function of R (horizontal axis) and ω (vertical axis). The grey-scale is such that dark values correspond to small values. The Rayleigh number is on a logarithmic scale and ranges from $5 \cdot 10^3$ to $5 \cdot 10^4$, while the frequency is on linear scale and ranges from 0 to 60. For further explanation, see the main text.

form

$$\begin{pmatrix} h_1^2 & h_2^2 & \dots & h_8^2 \\ h_1^3 & h_2^3 & \dots & h_8^3 \\ h_1^4 & h_2^4 & \dots & h_8^4 \\ h_1^8 & h_2^8 & \dots & h_8^8 \\ h_1^2 e^{\lambda_1 \Gamma_y} & h_2^2 e^{\lambda_2 \Gamma_y} & \dots & h_8^2 e^{\lambda_8 \Gamma_y} \\ h_1^3 e^{\lambda_1 \Gamma_y} & h_2^3 e^{\lambda_2 \Gamma_y} & \dots & h_8^3 e^{\lambda_8 \Gamma_y} \\ h_1^4 e^{\lambda_1 \Gamma_y} & h_2^4 e^{\lambda_2 \Gamma_y} & \dots & h_8^4 e^{\lambda_8 \Gamma_y} \\ h_1^8 e^{\lambda_1 \Gamma_y} & h_2^8 e^{\lambda_2 \Gamma_y} & \dots & h_8^8 e^{\lambda_8 \Gamma_y} \end{pmatrix} \begin{pmatrix} a_1 \\ a_2 \\ a_3 \\ a_4 \\ a_5 \\ a_6 \\ a_7 \\ a_8 \end{pmatrix} = 0, \quad (2.3.7)$$

where will refer to the matrix in this equation as M . Under the condition that the eigenvectors are not degenerate, i.e., when equation (2.3.6) is the correct form for a linear mode, a zero of $\det(M)$ corresponds to a linear mode with zero growth-rate. Since the determinant of M is complex valued, this gives two conditions on ω , R , Ω , σ , Γ_y and k . When we fix the system parameters σ , Γ_y and Ω , this gives ω and R as implicit functions of k . The wavenumber of the mode that goes unstable first determines k_c , so the minimum of $R(k)$ determines k_c , R_c and ω_c . Therefore, an algorithm for the determination of the linear onset values involves two steps; first one determines, for fixed k and system parameters, the location of a zero of $\det(M)$ in the (ω, R) -plane; secondly, this process is reiterated for other values of k in order to determine the minimum of $R(k)$.

This strategy presents us with several problems, and we will illustrate those with the help of plots of $\det(M)$ in the (ω, R) -plane. Note that zeroes of $\det(M)$, since this determinant is complex valued, generically correspond to isolated points in the (ω, R) -plane.

The mayor problem concerns the assumption that the eigenvectors are non-degenerate. It turns out that for this problem a degeneration of the eigenvalues (often) leads to a

degeneration of the eigenvectors (in general, this need not be the case). When such degeneracy occurs, the column-vectors of the matrix M are also degenerate, and so $\det(M) = 0$. However, such a zero *does not* correspond to a non-trivial solution of the equations of motion, since equation (2.3.6) is no longer correct when the eigenvectors h are degenerate. Since the eigenvalues are complex numbers, such degeneracies occur as isolated points in the (ω, R) -plane, i.e., with the same co-dimension as zeroes of $\det(M)$ that correspond with non-trivial solutions of the linearized equations of motion. In principle, when such a degeneracy occurs, one should replace the proper exponential parts $e^{\lambda y}$ of the ansatz (2.3.6) by functions of the form $ye^{\lambda y}$ and see whether one can construct a non-trivial solution that satisfies the boundary conditions. We expect that this is only possible in special cases, i.e., with higher co-dimension than the degeneracies, and therefore neglect this possibility. The problem with degenerate eigenvectors is illustrated in figure 2-2. A dark area in the left panel of figure 2-2 corresponds to a zero of $\det(M)$. An inspection of $\det(h)$, as shown in the middle panel, shows that two of these zeroes occur because the eigenvectors are degenerate and therefore not relevant for the linear stability analysis. To avoid the degeneracies, we define a function χ as follows.

$$\chi := \det(M) / \det(h) , \quad (2.3.8)$$

where h is the matrix which columns are the eigenvectors h_i of L . Simply dividing out these degeneracies yields the plot of χ on the right, that shows that there are only two relevant branches of solutions. The zero in the lower left corner corresponds to a mode that is born via a Hopf bifurcation, while the zero to the right, that occurs on the $\omega = 0$ axis, correspond to a stationary bifurcation.

The division of $\det(M)$ by $\det(h)$ solves an additional problem that one might encounter. Since M is built up from a combination of the eigenvalues and eigenvectors of L , the ordering of these eigenvalues affects the sign of $\det(M)$. Let us assume that we order these complex-valued eigenvalues by their real part. When ω and R are varied in order to determine zeroes of $\det(M)$, it often occurs that two eigenvalues interchange their ordering, which alternates the sign of $\det(M)$. Such change of sign has nothing to do with zeroes of $\det(M)$. However, $\det(h)$ also changes sign when two eigenvalues are interchanged, and therefore these irrelevant changes of the sign of $\det(M)$ are eliminated in χ .

In principle, one can use standard zero search routines to obtain the zeroes of χ . Due to subtle numerical issues, we have chosen to look for the minima of $|\chi|$, but this should be viewed as a minor technical point.

Obtaining from the zeroes of χ , for fixed system parameters Ω, σ and Γ_y , the Rayleigh number R as a function of k , the minimum of R can be calculated, and in principle the linear onset values (R_c, ω_c, k_c) follow. However, as is illustrated in figure 2-3 there are often multiple branches of solutions, and therefore many sets of linear onset values for fixed system parameters. Of course only the branch with lowest Rayleigh number is physically relevant, and so we are facing the question how to establish which branch of solutions has the lowest critical Rayleigh number. This is a global problem which in this case can be solved best on an ad-hoc basis. For fixed parameters and some reasonable chosen k , the

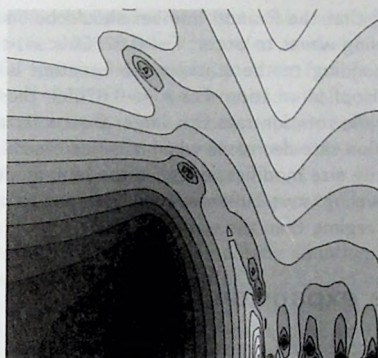


Figure 2-3. Plot of $|\chi|$ for wavenumber $k = 5$ and system parameters $\sigma = 0.15$, $\Omega = 1000$ and $\Gamma_y = 1$. The frequency ω ranges from 0 to 100 on the vertical scale, while the Rayleigh number R ranges from 10^4 to 10^6 on the horizontal (logarithmic) scale. The three minima with lowest R , i.e., the ones that are most to the left, can also be seen in figure 2-7 and are labeled branch 1, 2 and 3. Note that there are, for larger values of R , many branches of solutions, in particular on and near the $\omega = 0$ axis.

function $|\chi|$ is plotted as a function of ω and R (see figure 2-3). Such a plot shows that there are, in particular for small Prandtl number, many branches of solutions. One then picks out two or three candidates for the lowest Rayleigh number, calculates the critical wavenumber k_c and R_c and ω_c and at the end one then simply establishes which branch of solutions is relevant for the particular system parameters, i.e., selects the set of onset values with lowest R_c . The existence of these many branches has been investigated in considerable detail by Goldstein *et al.* [43], although not for an annulus. Below we will concentrate on a few branches that can have the lowest critical Rayleigh number, and they will correspond to a stationary bifurcation and a Hopf bifurcation to either a wall- or a bulk-mode. In particular, the situation becomes quite convoluted for small σ as we will discuss below.

Before we go on and describe the amplitude expansion, it is instructive to compare the linear stability analysis presented above with the stability analysis for an unbounded rotating layer with slip top and bottom plate, as given by Chandrasekhar [3]. When there are no vertical boundaries, the linear stability analysis is considerably simpler. Suppose we look for plane-wave solutions, then the ansatz for the linear modes (2.3.2) can be simplified by assuming the modes to be independent of y , i.e., choosing a coordinate frame such that the critical wave-vector is parallel to the x -axis. We no longer have to solve the ordinary differential equations for the W_i ; instead, one finds a simple dispersion relation that is a polynomial in s, k, ω, R and σ . From this dispersion relation, one can draw important conclusions for the bulk-modes, and this will be relevant for the annulus.

It has been shown [3] that the Prandtl number should be smaller than 1 for a Hopf bifurcation towards traveling waves to occur. For $0.67659 < \sigma < 1$ however, the critical Rayleigh number corresponding to the stationary bifurcation is lower than the critical Rayleigh number of the Hopf bifurcation. For $\sigma < 0.67659$, the Hopf bifurcation is the primary bifurcation when the rotation-rate Ω is larger than a certain critical rotation-rate Ω_c , and this critical rotation-rate decreases when σ is decreased.

We will encounter finite size modifications of these bulk-modes later, and the amplitude equations of the traveling wave bulk-mode will turn out to have their coefficients in a much more interesting regime than the wall-modes.

2.4 Amplitude expansion.

In this section we will describe the derivation of the amplitude equations and the calculation of their coefficients. This derivation of the amplitude equations is along the same lines as for the Swift-Hohenberg equation (1.3.2) as presented in chapter 1; however, mainly due to the higher dimensionality of the underlying fluid-equations and the inclusion of boundaries, the practical implementation is more complicated here. The amplitude equations describing the slow modulations of a right-traveling mode with x, t -dependence $e^{i(-k_c x + \omega_c t)}$ and amplitude A coupled to a left-traveling mode with x, t -dependence $e^{i(k_c x + \omega_c t)}$ and amplitude B are [4]

$$\begin{aligned} \tau_0(\partial_t + v_g \partial_x)A = & \quad \varepsilon(1 + ic_0)A + \xi_0^2(1 + ic_1)\partial_x^2 A - \\ & g_0(1 - ic_3)|A|^2 A - g_2(1 - ic_2)|B|^2 A, \end{aligned} \quad (2.4.1a)$$

$$\begin{aligned} \tau_0(\partial_t - v_g \partial_x)B = & \quad \varepsilon(1 + ic_0)B + \xi_0^2(1 + ic_1)\partial_x^2 B - \\ & g_0(1 - ic_3)|B|^2 B - g_2(1 - ic_2)|A|^2 B, \end{aligned} \quad (2.4.1b)$$

where $\varepsilon := (R - R_c)/R_c$, and the coefficients τ_0, \dots, c_2 are real numbers that depend on the details of the underlying physical system. The coefficients τ_0 and ξ_0^2 measure the temporal and spatial scales, and therefore they are usually scaled out in theoretical considerations (see equation (1.4.19)). We include them here, because they are necessary for making contact with experiments.

The first order spatial derivative terms are formally of lower order in ε than the other terms of the amplitude equations, but they arise because of the traveling wave nature of the linear modes. Strictly, v_g should go to zero for $\varepsilon \downarrow 0$ for equation (2.4.1) to hold (see chapter 1). The group-velocity can be calculated with relative ease from the linear dispersion relation, and will turn out to be of order one (see below).

In this section we show how to obtain the coefficients for the amplitude equations from the underlying equations of motion (2.2.4). The standard amplitude approach [7] is to perform a so-called ε -expansion by setting

$$U = \varepsilon^{1/2}U_0 + \varepsilon U_1 + \varepsilon^{3/2}U_2 + \mathcal{O}(\varepsilon^2) + c.c., \quad (2.4.2)$$

where U_0 is the product of a solution of the linearized equations of motion u_0 , and a slowly varying amplitude function A : $U_0 = A(X, T)u_0$ [7]. We will from now on adopt

the notation that large U 's contain slow and fast scales and small u 's only contain the fast scales; X and T are the slow scales $\varepsilon^{1/2}x$ and εt , and A is of order 1 here.

Below, we often split functions according to their fast (x, t) -dependence, and the part of u_0 that goes like $e^{i(-k_x x + \omega_c t)}$ will be denoted by $u_0|_{-1,1}$. To this x, t dependence corresponds the slow amplitude A , and similarly a $(1, -1)$ dependence corresponds to A^* , and a $(1, 1)$ dependence corresponds to B . In principle, u_0 may correspond to any combination of the left- and right-traveling modes, i.e., $U_0 = A u_0|_{-1,1} + B u_0|_{1,1} + c.c.$. We will later show how we use this freedom in the choice of U_0 to obtain the coefficients of both nonlinear terms.

Regardless of the precise form of u_0 , the amplitude equations are obtained as follows. First of all, we have to expand the linear operator \mathcal{L} (2.2.5) in orders of $\varepsilon^{1/2}$. The lowest order contribution at order 1 comes from $\mathcal{L}_0 := \mathcal{L}|_{R=R_c}$, where \mathcal{L}_0 only works on the fast scale, i.e., the u_i . The differential operators in \mathcal{L} have to be split in a fast and a slow part (see chapter 1), e.g., $\partial_x \rightarrow \partial_x + \varepsilon^{1/2} \partial_X$. This yields at order $\varepsilon^{1/2}$ an operator that we denote by \mathcal{L}_X , and that contains a first order derivative with respect to the slow scale X . At order ε , we obtain along similar lines the operator \mathcal{L}_{XX} and \mathcal{L}_T (2.4.9). And finally we have at order ε the difference between \mathcal{L} and \mathcal{L}_0 : $\Delta\mathcal{L} := (\mathcal{L}_f - \mathcal{L}_0)/\varepsilon$ (see equation (2.4.8)). This yields the following expansion for the linear operator:

$$\mathcal{L} = \mathcal{L}_0 + \varepsilon \Delta\mathcal{L} + \varepsilon^{1/2} \mathcal{L}_X + \varepsilon \mathcal{L}_{XX} + \varepsilon \mathcal{L}_T. \quad (2.4.3)$$

Substituting this and the expansion (2.4.2) into the equations of motion, and collecting subsequent orders in $\varepsilon^{1/2}$ yields:

$$\mathcal{L}_0 U_0 = 0, \quad (2.4.4a)$$

$$\mathcal{L}_0 U_1 = \mathcal{L}_X(U_0) + \mathcal{N}(U_0, U_0), \quad (2.4.4b)$$

$$\mathcal{L}_0 U_2 = \mathcal{L}_X(U_1) + (\mathcal{L}_T + \mathcal{L}_{XX} + \Delta\mathcal{L})(U_0) + \mathcal{N}_s(U_0, U_1), \quad (2.4.4c)$$

where $\mathcal{N}_s(U_0, U_1)$ is defined as $\mathcal{N}(U_0, U_1) + \mathcal{N}(U_1, U_0)$. The first equation of this so-called ε -expansion is equivalent to the linearized equations of motion that we solved in section 2.3. Since the nonlinearity \mathcal{N} (2.2.6) is strictly quadratic, in equation (2.4.4b) \mathcal{N} is applied to U_0 and in equation (2.4.4c) it is applied to a combination of U_0 and U_1 . In principle, equation (2.4.4b) can be solved, and when U_1 is found, the solvability condition of equation (2.4.4c) yields via the Fredholm theorem [4] the amplitude equation:

$$\langle u_0^\dagger, \mathcal{L}_X(U_1) + (\mathcal{L}_T + \mathcal{L}_{XX} + \Delta\mathcal{L})(U_0) + \mathcal{N}_s(U_0, U_1) \rangle = 0, \quad (2.4.5)$$

where u_0^\dagger is a zero mode of the adjoint linear operator (see sec. (2.4.1)). The inner-product $\langle f, g \rangle$ is defined as $\int d\vec{x} dt f^* g$, where the integral is taken over the volume of the convection cell.

Assume for the moment that we have calculated u_0^\dagger and u_1 . Then the integrals in the inner-product (2.4.5) could be evaluated and the coefficients of the CGLE could be obtained, but as pointed out by Schöpf and Zimmerman [41], this would be a tremendous and partly unnecessary task. The calculations become technically less involved, in particular for the coefficients ξ_0 and c_1 , when the linear and nonlinear coefficients are calculated separately.

To calculate the linear coefficients, a linear analysis of the equations of motion is sufficient. A traveling wave of the CGLE corresponds to a solution of the full equations of motion with wavenumber and frequency shifted from the critical values. Therefore when we obtain from the linear analysis the relations between R , ω , s and k around their critical values, we can determine the linear dispersion of the CGLE's. The precise relations for a wave with x, t -dependence $e^{i(-kx+\omega t)+st}$ are

$$v_g = \frac{\partial \omega}{\partial k} \Big|_{R=R_c}, \quad \tau_0^{-1} = R_c \frac{\partial s}{\partial R} \Big|_{k=k_c}, \quad \xi_0^2 = \frac{1}{2R_c} \frac{\partial^2 R_c}{\partial k^2} \Big|_{s=0}, \quad (2.4.6a)$$

$$c_0 = \tau_0 R_c \frac{\partial \omega}{\partial R} \Big|_{k=k_c}, \quad c_1 = -\frac{\tau_0}{2\xi_0^2} \frac{\partial^2 \omega}{\partial k^2} \Big|_{R=R_c}. \quad (2.4.6b)$$

The calculation of the nonlinear coefficients of the amplitude equations is simplified by taking A independent of X , since this dependence only leads to the calculation of the linear coefficients ξ_0^2 and c_1 of the CGLE. In the ε -expansion, this means that the operators \mathcal{L}_X and \mathcal{L}_{XX} are zero.

In principle, we could also take A independent of T , but including a T dependence is relatively easy, and so the coefficients for the temporal derivative of the CGLE are found either by performing the amplitude expansion or from the linear analysis, which can be used as a check.

When A only depends on T the ε -expansion becomes:

$$\mathcal{L}_0 U_0 = 0, \quad (2.4.7a)$$

$$\mathcal{L}_0 U_1 = \mathcal{N}(U_0, U_0), \quad (2.4.7b)$$

$$\mathcal{L}_0 U_2 = (\mathcal{L}_T + \Delta \mathcal{L})(U_0) + \mathcal{N}_s(U_0, U_1). \quad (2.4.7c)$$

The operators $\Delta \mathcal{L}$ and \mathcal{L}_T are obtained by extracting from the linear operator \mathcal{L} the part linear in ε

$$\Delta \mathcal{L} = \begin{pmatrix} 0 & 0 & 0 & 0 \\ 0 & 0 & 0 & 0 \\ 0 & 0 & 0 & -R_c \partial_y \\ 0 & 0 & 0 & R_c \partial_x \end{pmatrix}, \quad (2.4.8)$$

and the part containing a first order time derivative

$$\mathcal{L}_T = \begin{pmatrix} 0 & 0 & 0 & 0 \\ 0 & 0 & 0 & 1 \\ 0 & -\partial_z/\sigma & \partial_y/\sigma & 0 \\ \partial_z/\sigma & 0 & -\partial_x/\sigma & 0 \end{pmatrix} \partial_T. \quad (2.4.9)$$

The solvability condition for equation (2.4.7c) is

$$\langle u_0^\dagger, (\mathcal{L}_T + \Delta \mathcal{L})(U_0) + \mathcal{N}_s(U_0, U_1) \rangle = 0. \quad (2.4.10)$$

It is at this point of the calculation that it is instructive to inspect the x, t -dependencies of the various terms occurring in the solvability condition (2.4.10). Since \mathcal{N} is bilinear, its

x, t -dependencies follow directly from the x, t -dependencies of its arguments:

$\mathcal{N}(u_i|_{m_1, n_1}, u_j|_{m_2, n_2})$ has x, t -dependency $(m_1 + m_2, n_1 + n_2)$. Since the U_0 is of general form

$$U_0 = A(-1, 1) + B(1, 1) + c.c. , \quad (2.4.11)$$

it follows that U_1 is of the form

$$U_1 = (A^2(-2, 2) + B^2(2, 2) + AB(0, 2) + AB^*(2, 0)) + c.c. + |A|^2(0, 0) + |B|^2(0, 0) + H(\pm 1, \pm 1) . \quad (2.4.12)$$

H corresponds to a homogeneous solution of equation (2.4.7b) with x, t -dependence $(\pm 1, \pm 1)$; this part of U_1 does not contribute to the solvability condition and can therefore be omitted.

The inner product $\langle u_0^\dagger, f \rangle$ is defined as $\int dx dy dz dt u_0^\dagger f$, and the integrals over x and t yield that for a certain term to contribute to the solvability condition, it should be independent of x and t . Since u_0^\dagger has only parts going like $(\pm 1, \pm 1)$, only the following parts contribute to the solvability condition:

$$(-1, 1) : A_T, A, |A|^2 A, |B|^2 A , \quad (2.4.13a)$$

$$(1, 1) : B_T, B, |B|^2 B, |A|^2 B , \quad (2.4.13b)$$

$$(1, -1) : A_T^*, A^*, |A|^2 A^*, |B|^2 A^* , \quad (2.4.13c)$$

$$(-1, -1) : B_T^*, B^*, |B|^2 B^*, |A|^2 B^* . \quad (2.4.13d)$$

Since the solvability condition (2.4.10) should be true for any zero mode u_0^\dagger of the adjoint, in fact four solvability conditions follow, for the $(1, 1)$, $(1, -1)$, $(-1, 1)$ and $(-1, -1)$ part. This yields in principle 4 amplitude equations for A, B, A^* and B^* , but those of A and A^* are related by simple complex conjugation, and those of A and B are related by the 180° rotation symmetry. Therefore we only need the $(1, -1)$ part of u_0^\dagger and the $(-1, 1)$ part of $(\mathcal{L}_T + \Delta \mathcal{L})(U_0) + \mathcal{N}_s(U_0, U_1)$ to calculate the coefficients of the amplitude equations.

It is important to notice that when we choose u_0 to correspond to a single mode, say $B = 0$, the ensuing amplitude equation does not contain a cross-coupling term $|B|^2 A$, and the nonlinear term obtained from the solvability condition corresponds to $-g_0(1 - ic_3)|A|^2 A$. When u_0 is the sum of both left- and right-traveling waves with equal amplitude, we in fact have forced $A = B$, and the nonlinear term we obtain then is the sum of the $|A|^2 A$ and $|B|^2 A$ term, i.e., since $A = B$, $[-g_0(1 - ic_3) - g_2(1 - ic_2)]|A|^2 A$. Since g_0 and c_3 follow from a single mode amplitude expansion, g_2 and c_2 can thus be obtained from a double mode amplitude expansion [41].

As shown in equations (2.3.2) and (2.4.25), the z -dependencies are given explicitly by simple goniometrical functions, and so the integrals over x, t and z are performed explicitly. The y -dependencies will be more complicated, and the solvability condition (2.4.10) can be written as

$$\left(\int dy I_T \right) \partial_T A = - \left(\int dy I_\Delta \right) A + \left(\int dy I_N \right) |A|^2 A , \quad (2.4.14)$$

where the I 's denote functions of y that follow from equation (2.4.10). In particular, I_T comes from \mathcal{L}_T , I_Δ comes from $\Delta\mathcal{L}$ and I_N comes from \mathcal{N}_s . Note that this form of the amplitude equation is written for the slow scale T , and that no terms with spatial derivatives occur here. Bearing this in mind, taking u_0 to be a single mode (i.e., $B=0$) and comparing equation (2.4.14) to the amplitude equation (2.4.1a), we find the following expressions for the coefficients of this amplitude equation:

$$(1 + ic_0)/\tau_0 = \int dy I_\Delta / \int dy I_T, \quad (2.4.15)$$

$$g_0(1 - ic_3)/\tau_0 = \int dy I_N / \int dy I_T. \quad (2.4.16)$$

Using the expressions (2.4.9) and (2.4.8) to work out equation (2.4.15), we obtain

$$\frac{1 + ic_0}{\tau_0} = \frac{- \int dy dz (u_0^\dagger|_{1,-1}) \cdot \begin{pmatrix} 0 \\ 0 \\ -R_c \partial_y u_{0\theta}|_{-1,1} \\ R_c \partial_x u_{0\theta}|_{-1,1} \end{pmatrix}}{\int dy dz (u_0^\dagger|_{1,-1}) \cdot \begin{pmatrix} 0 \\ u_{0\theta}|_{-1,1} \\ \partial_y u_{0z}|_{-1,1} / \sigma - \partial_z u_{0y}|_{-1,1} / \sigma \\ \partial_z u_{0x}|_{-1,1} / \sigma - \partial_x u_{0z}|_{-1,1} / \sigma \end{pmatrix}}, \quad (2.4.17)$$

and this expression for τ_0 and c_0 has been used to check our numerics against the results obtained from the linear analysis (equations (2.4.6)).

Equation (2.4.16) can be worked out along similar lines and yields the nonlinear coefficients. Note that, without a choice of normalization, the value of g_0 is meaningless. We choose the norm of u_0 such that the ratio of convected to conducted heat is equal to $|A|^2$. In our units, the conducted heat density is equal to 1, while the convected heat density is given by $v_z \theta$. This yields as a normalization condition:

$$\frac{1}{2\Gamma_y} \int_0^{\Gamma_y} dy W_3 W_4^* + c.c. = 1. \quad (2.4.18)$$

We will now proceed by discussing the calculation of u_0^\dagger and u_1 .

2.4.1 The adjoint solution.

To obtain u_0^\dagger , we determine \mathcal{L}^\dagger , the adjoint of the operator \mathcal{L} , and the boundary conditions on u_0^\dagger from the requirement

$$\langle W^\dagger, \mathcal{L}\bar{W} \rangle = \langle \mathcal{L}^\dagger W^\dagger, \bar{W} \rangle, \quad (2.4.19)$$

where \bar{W} obeys the boundary conditions (2.2.7) and the boundary conditions on W^\dagger are to be established. The inner-product is defined as in section 2.4.

To go from the left- to the right-hand side of equation (2.4.19), we perform integrations by parts. We show how this works in practice for the matrix element $\mathcal{L}_{12} = \partial_y$

(see equation (2.2.5)). The requirement (2.4.19) yields on the left-hand side the expression $\int dy W_1^{\dagger*} \partial_y \bar{W}_2$ which can be integrated by parts and results in $\int dy (-\partial_y W_1^{\dagger*}) \bar{W}_2 + W_1^{\dagger*} \bar{W}_2|_0^1$. This results in $\mathcal{L}_{21}^\dagger = -\partial_y$ and since $\bar{W}_2 = 0$ on the y -boundaries, no additional boundary conditions; for other matrix elements, the boundary terms are non-trivial and this yields the boundary conditions below. The calculation of the other matrix elements of \mathcal{L}^\dagger can be carried out in a similar fashion, and so we find \mathcal{L}^\dagger

$$\mathcal{L}^\dagger = \begin{pmatrix} -\partial_x & 0 & 2\Omega\partial_z & -D^\dagger\partial_z \\ -\partial_y & 0 & D^\dagger\partial_z & 2\Omega\partial_z \\ -\partial_z & -1 & -D^\dagger\partial_y & D^\dagger\partial_x \\ 0 & -\partial_t - \nabla^2 & R\partial_y & -R\partial_x \end{pmatrix}, \quad (2.4.20)$$

where D_\perp is defined as $(-\partial_t/\sigma - \nabla^2)$. Requiring the boundary terms to vanish yields as boundary conditions for the adjoint:

$$\partial_y W_2^\dagger = W_3^\dagger = \partial_y W_3^\dagger = W_4^\dagger = 0 \quad \text{on } y = 0, \Gamma_y \quad (2.4.21)$$

$$W_2^\dagger = W_3^\dagger = \partial_z^2 W_3^\dagger = W_4^\dagger = \partial_z^2 W_4^\dagger = 0 \quad \text{on } z = 0, 1. \quad (2.4.22)$$

As discussed above, we only need the $(1, -1)$ part of $u_0^{\dagger*}$, or equivalently, the $(-1, 1)$ part of u_0^\dagger . The conditions on the z -boundary are satisfied by taking

$$u_0^\dagger = e^{i(-kx + \omega t)} \begin{pmatrix} \cos(\pi z) & W_1^\dagger \\ \sin(\pi z) & W_2^\dagger \\ \sin(\pi z) & W_3^\dagger \\ \sin(\pi z) & W_4^\dagger \end{pmatrix}, \quad (2.4.23)$$

and substituting this ansatz in the equations for u_0^\dagger , we end up with a set of linear, coupled ordinary differential equations for the W_i^\dagger , that can be solved in a similar fashion as the linearized equations of motion for U . As in the calculation of U_0 , the slip boundary conditions allow us to have a simple z -dependence that both separates the equations of motion and satisfies the boundary conditions.

2.4.2 Calculation of u_1 .

As explained above, u_1 is built up from many parts with different x, t -dependencies, and we have to calculate all these parts separately. For definiteness we will concentrate on $u_1|_{-2,2}$; the calculations for the other parts are completely analogous. For this particular x, t -dependence we have an equation of the form

$$\mathcal{L}_0 u_1|_{-2,2} = \mathcal{N}(u_0|_{-1,1}, u_0|_{-1,1}), \quad (2.4.24)$$

with \mathcal{N} defined by equation (2.2.6). The first step in calculating u_1 is the determination of $\mathcal{N}(u_0|_{-1,1}, u_0|_{-1,1})$. The nonlinear operator is quadratic and contains derivatives with respect to t, x, y and z up to third order. The x, t -dependence of the nonlinear term is readily obtained to be $e^{2i(-kx + \omega t)}$ as anticipated in equation (2.4.24). The z -dependence

of the nonlinear term is the same for all different x, t -dependences: the first component is zero, and the other components have z -dependence $\sin(2\pi z)$. As before, the y -dependence is more complicated. Taking u_1 of the form

$$u_1|_{-2,2} = e^{2i(-kx + \omega t)} \begin{pmatrix} \cos(2\pi z) & u_{1x}(y) \\ \cos(2\pi z) & u_{1y}(y) \\ \sin(2\pi z) & u_{1z}(y) \\ \sin(2\pi z) & u_{1\theta}(y) \end{pmatrix}, \quad (2.4.25)$$

satisfies the boundary conditions on $z = 0, 1$ and has the correct z -dependence to solve equation (2.4.24). Since the components of u_0 are sums over simple exponential functions (see equation (2.3.6)), the right-hand side of equation (2.4.24) can also be written as such a sum. Note that although this term is of considerable length, and the coefficients of these exponentials come out of the numerical procedure that determines u_0 , an exact expression can be found for u_1 once these coefficients are known.

We then perform the differentiations with respect to t, x and z on the left-hand side of equation (2.4.24) which yields a term of the form $(\mathcal{L}_y + M_1)u_1$, where \mathcal{L}_y represents the part of \mathcal{L} that contains derivatives with respect to y and M_1 is a constant matrix that should not be confused with M (2.3.7). Dropping the common x, z and t dependences on both sides of equation (2.4.24) yields a set of ordinary differential equations for the components of u_1 of the form $(\mathcal{L}_y + M_1)u_1(y) = N(y)$. Analogous to the calculation of the linear modes (see section 2.3), we rewrite these equations as a set of first order ordinary differential equations for the components of u and their derivatives, which we denote by the vector \bar{w} . After some rewriting this yields an equation of the form

$$(\partial_y + \bar{M}_1)\bar{w} = \bar{w} + N(y), \quad (2.4.26)$$

where \bar{M}_1 is a matrix depending on the system parameters, and $N(y)$ is the vector consisting of sums of exponential functions, that is obtained by calculating $N(u_0|_{-1,1}, u_0|_{-1,1})$ once u_0 has been obtained.

The vector $N(y)$ is of the form $\sum_n \alpha_n \exp(\gamma_n y)$, where the α_n 's are also vectors. A particular solution of equation (2.4.26) is of the form $\bar{w} = \sum_n \beta_n \exp(\gamma_n y)$, and the vectors β_n can be found from the matrix equation $\beta_n = (\gamma_n \mathbb{I} + \bar{M}_1)^{-1} \alpha_n$, where \mathbb{I} is the unit-matrix. To satisfy the boundary conditions for u_1 at $y = 0, d$, we calculate homogeneous solutions of (2.4.26) and then add to the particular solution the correct homogeneous solution such as to fulfill the boundary conditions. This also involves a simple numerical procedure; the form of u_1 is found analytically. It is at this point of the calculation that we benefit from dropping the z -part of the rotation of equation (2.2.3a), since it turns out that the corresponding nonlinear term is more complicated than the terms for the x and y -components of the rotation.

In the case of a single mode, u_1 has three parts with different x, t -dependence, so we have to solve equation (2.4.24) for the $(0, 0)$, $(-2, 2)$ and $(2, -2)$ part. These last two terms are a complex conjugated pair, so we only need to calculate one of them. Summing up the three parts, we obtain the solution to the equation $\mathcal{L}_0 u_1 = N(u_0, u_0)$.

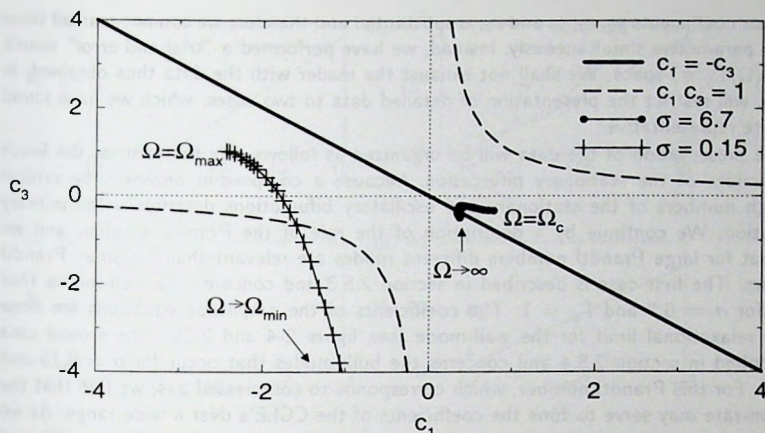


Figure 2-4. Overview of the dependence of the coefficients c_1 and c_3 on the rotation-rate Ω for an annulus of width 1 and Prandtl numbers 6.7 and 0.15. The fat curve $c_1 = -c_3$ indicates the relaxational limit of the CGLE's as discussed in chapter 1. The dashed curve $c_1 c_3 = 1$ corresponds to the Newell criterion (1.5.2), and outside of these hyperbolae all phase-winding solutions are unstable and spatio-temporal chaos occurs. The curve for $\sigma = 6.7$ shows that in this case the coefficients stay close to the relaxational limit. For $\sigma = 0.15$, the rotation-rate is able to tune the parameters from close to the relaxational limit to deep into the spatio-temporal chaotic regime. This is therefore an attractive experimental realization of the CGLE. The quantities Ω_{min} , Ω_{max} and Ω_c are discussed in section 2.5.4.

In the case of a double mode, $\mathcal{N}(u_0, u_0)$ has x, t -dependences (m, n) where both m and n can be $-2, 0$ or 2 . For the amplitude equation, we have to obtain $\mathcal{N}(u_1, u_0)|_{-1,1}$, and therefore we only need the parts of u_1 that go like $(-2, 2), (-2, 0), (0, 0)$ and $(0, 2)$.

2.5 Results.

With the tools described in the previous sections, we will determine both the linear onset values and the coefficients of the amplitude equations. The rotating annulus, in our straight channel approach, is parameterized by three parameters: the rotation-rate Ω , the width of the channel Γ_y , and the Prandtl number σ . In a typical experiment, the latter two are fixed, whereas Ω can be adjusted over a certain range. Our primary goal is obtaining system parameters σ and Γ_y such that the freedom in adjusting the rotation-rate can be used to scan the coefficients of the CGLE's from the dissipative ($c_1 \approx -c_3$) to the chaotic ($c_1 c_3 > 1$) regime.

The amount of computer time that is needed, in particular for the calculation of the

nonlinear coefficients g_0, c_3, g_2 and c_2 , is substantial and therefore we can not scan all three system parameters simultaneously. Instead, we have performed a "trial and error" search in the $(\Omega, \Gamma_y, \sigma)$ -space. We shall not exhaust the reader with the data thus obtained; in fact we will restrict the presentation of detailed data to two cases, which we have found are quite representative.

The presentation of the data will be organized as follows. We first discuss the linear onset values of the stationary bifurcation, because a comparison between the critical Rayleigh numbers of the stationary and oscillatory bifurcations determines the primary bifurcation. We continue by a description of the role of the Prandtl number, and we find that for large Prandtl numbers different modes are relevant than for small Prandtl numbers. The first case is described in section 2.5.3 and concerns the wall-modes that occur for $\sigma = 6.7$ and $\Gamma_y = 1$. The coefficients of the amplitude equations are close to the relaxational limit for the wall-mode (see figure 2-4 and 2-10). The second case is described in section 2.5.4 and concerns the bulk-modes that occur for $\sigma = 0.15$ and $\Gamma_y = 1$. For this Prandtl number, which corresponds to compressed gas, we find that the rotation-rate may serve to tune the coefficients of the CGLE's over a wide range. As we will discuss below, these two cases are representative for many values of the width and Prandtl number. The dependence of the coefficients c_1 and c_3 of the CGLE's for these two modes is illustrated in figure 2-4.

2.5.1 Stationary bifurcation.

Although we want to focus on the traveling wave, it may occur, for certain parameters, that the critical Rayleigh number of the stationary bifurcation is lower than that of the oscillatory bifurcation. When this is the case, the amplitude equation is a single RGLE and we do not want to focus on this case. We therefore present in figure 2-5 the linear onset values of the stationary bifurcation, in order to facilitate a comparison with the linear onset values of the oscillatory modes presented in sections 2.5.3 and 2.5.4. We found that there are two candidates for the primary stationary mode, and for $\Omega \approx 300$ the critical Rayleigh numbers of these two modes interchange their ordering. This is illustrated in figure 2-5a-b.

The stability analysis for the stationary waves does not depend on the value of σ . This follows directly from the expression for the linear operator \mathcal{L} (2.2.5), since the only occurrence of σ in \mathcal{L} is via terms of the form $\sigma^{-1}\partial_t$. For stationary modes, with growth-rate $s = 0$, the derivative with respect to t is equal to zero, and therefore the value of σ is immaterial in this case.

The crossover value where the Rayleigh number of the stationary and the Hopf bifurcation are equal, will be denoted by Ω_c (see figure 2-5c). For $\sigma = 6.7$ and $\Gamma_y = 1$, $\Omega_c \approx 27.5$, while for $\sigma = 0.15$ and $\Gamma_y = 1$, $\Omega_c \approx 16.5$ (see sections 2.5.3 and 2.5.4). The stationary bifurcation is therefore only relevant when Ω is close to Ω_0 where Ω_0 is the minimal value of the rotation-rate for which a Hopf bifurcation occurs (see figure 2-5). As a consequence, the divergencies of c_1 and v_y that occur because $\omega \sim \sqrt{\Omega - \Omega_0}$ (see below), can not be observed in experiments. For sufficiently large rotation-rates, the Hopf

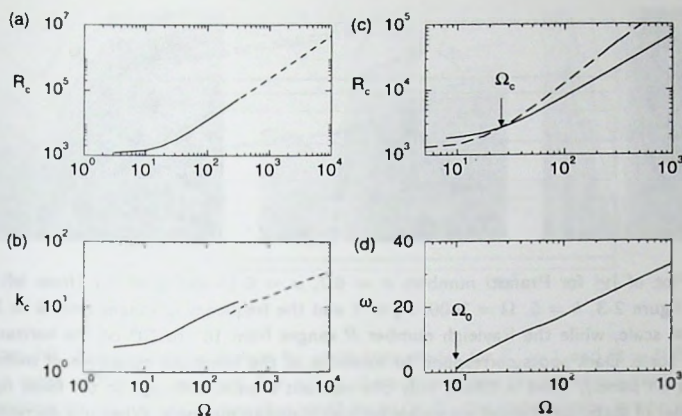


Figure 2-5. In panel (a) and (b) we show the critical Rayleigh number and wavenumber for the stationary mode in an annulus with $\Gamma_y = 1$. As explained in the main text, the value of the Prandtl number is immaterial for the stationary bifurcation. The stationary branch that is relevant for $\Omega < 300$ is different from the one that is relevant for $\Omega > 300$; these two branches are indicated by solid and dashed curves in (a) and (b). In panel (c) the critical Rayleigh numbers of both of these stationary modes are indicated by a dashed curve, while the critical Rayleigh numbers of the Hopf bifurcation that occurs for $\sigma = 6.7$ and $\Gamma_y = 1$ is indicated by a solid curve. For rotation-rates above a certain threshold Ω_c , the Hopf bifurcation is seen to be the primary bifurcation. In panel (d) we illustrate the definition of Ω_0 which is the minimum value of Ω for which a Hopf bifurcation occurs. For all the data that we present, $\Omega_c > \Omega_0$, and therefore the frequencies of the Hopf modes that can be observed in experiments are bound away from zero.

bifurcation is observed to have the lowest critical Rayleigh number.

2.5.2 The role of the Prandtl number.

In this section we discuss the effect of the Prandtl number on the linear onset values. Goldstein *et al.* [43] have shown that for an infinite cylinder, the bifurcation structure is quite complicated for small values of the Prandtl number. We found that something similar happens for the rotating annulus. In particular, the number of potentially relevant branches of solutions increases rapidly when σ is decreased to values of order 0.1 (see figure 2-6). The branch with the lowest critical Rayleigh number is relevant for the experiments, and as a function of the system parameters, different branches become relevant. We should stress that our focus is not on the whole bifurcation structure, but only on the relevant branches.

It is unlikely that one can make close contact with experiments for Prandtl numbers

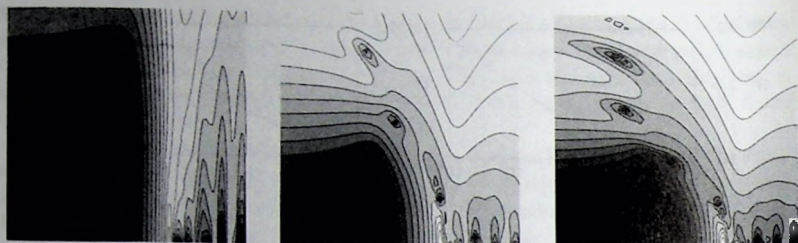


Figure 2-6. Plot of $|\chi|$ for Prandtl numbers $\sigma = 6.7$, $\sigma = 0.15$ and $\sigma = 0.1$ (from left to right). As in figure 2-3, $k = 5$, $\Omega = 1000$, $\Gamma_y = 1$ and the frequency ω ranges from 0 to 100 on the vertical scale, while the Rayleigh number R ranges from 10^4 to 10^6 on the horizontal (logarithmic) scale. Dark spots correspond to solutions of the linearized equations of motion. For $\sigma = 6.7$ (left panel), there is clearly only one relevant branch, although in the lower right corner a number of stationary modes are visible for high Rayleigh numbers. When σ is decreased, new oscillatory branches bifurcate from the $\omega = 0$ axis, and when $\sigma = 0.15$ (middle panel), the difference between the Rayleigh numbers of some of this branches is small and two or three modes are candidates for the primary bifurcation (see figure 2-7). When σ is decreased even further to a value of 0.1, the situation rapidly becomes more complicated, as shown in the right panel.

smaller than 0.1; when small changes of the system parameters lead to very different behavior of the system, one simply loses track. Besides, for liquids that have small Prandtl number, such as mercury ($\sigma \approx 0.025$) and liquid gallium ($\sigma \approx 0.005$), the visualization of the patterns is experimentally quite difficult, if not impossible. We therefore restrict ourselves to Prandtl numbers larger than 0.1 (see figure 2-7), and in fact only present detailed data for the cases $\sigma = 0.15$ and $\sigma = 6.7$; as we will explain below, these two cases cover the characteristic behavior for $\sigma > 0.1$.

An inspection of the linear operator \mathcal{L} yields the following, qualitative and intuitive picture for the dependence of the bifurcation structure on the Prandtl number. As discussed in the section on the stationary bifurcation, the dependence of \mathcal{L} on σ only occurs via terms of the form $\sigma^{-1}\partial_t$, so we can split this linear operator in a part independent of σ (\mathcal{L}_i) and a part that contains the explicit σ dependence ($1/\sigma \mathcal{L}_\sigma$):

$$\mathcal{L} = \mathcal{L}_i + 1/\sigma \mathcal{L}_\sigma. \quad (2.5.1)$$

This should in principle allow us to describe the behavior of large σ in perturbation theory around the limit $\sigma \rightarrow \infty$. Although we have not carried out such an expansion, we have observed that for all practical purposes, a value of σ of 6.7 results in linear onset values that are already very close to those in the limit $\sigma \rightarrow \infty$. In contrast, when σ is decreased, the operator \mathcal{L}_σ becomes more and more important, and new phenomena may occur.

As this is only an intuitive picture, we have calculated the relevant linear onset values for oscillatory modes for $\Gamma_y = 1$ and $\Omega = 1000$ as a function of the Prandtl number, as

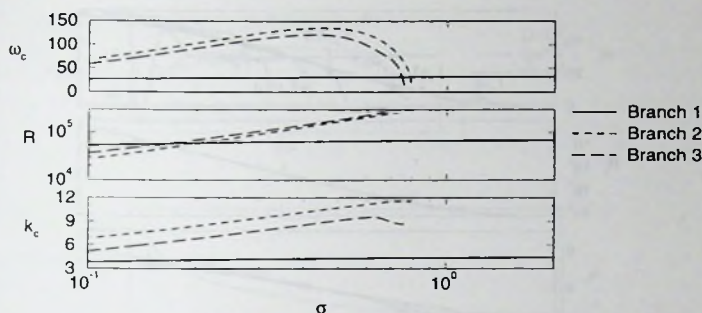


Figure 2-7. The linear onset values for oscillatory modes for $\Gamma_y = 1$ and $\Omega = 1000$ are plotted for a range of Prandtl numbers. For $\sigma > 1$ there is only one branch of solutions, that is quite insensitive to the precise value of σ , and for $\sigma > 2$, this dependence is not visible on the scale of the figure above. For lower values of the Prandtl number, new branches bifurcate from stationary modes, and below $\sigma \approx .2$ one of them becomes relevant. For further reference, the three branches of solutions are labeled branch 1, branch 2 and branch 3.

shown in figure 2-7. For a fixed rotation-rate, the branches 2 and 3 are seen to bifurcate from a stationary convection mode at $\omega = 0$ when σ is decreased. Note that this occurs for values of the Prandtl number that are comparable to those where the Hopf bifurcation in an infinite layer occurs first (see the discussion at the end of section 2.3). Indeed the branches 2 and 3 have a bulk-mode geometry (see figure 2-13).

The effect of the width of the annulus turns out not to be very interesting for the coefficients of the CGLE's, and below we therefore usually take $\Gamma_y = 1$. In contrast, the value of the rotation-rate does affect the relevance of the various branches substantially. To obtain a complete picture, a calculation of the critical Rayleigh numbers for a range of both σ and Ω is desirable. We have performed scans of Ω for many values of σ , and then it turns out that we may capture the essential features of our system in the σ -scan presented above, and in two scans of Ω for $\sigma = 6.7$ and $\sigma = 0.15$.

The most important properties of the branches 1, 2 and 3 that we will establish in section 2.5.3 and 2.5.4 are listed below.

- **branch 1:** This is the branch that is relevant for Prandtl numbers larger than 0.2. It is a wall-mode, i.e., the convection is localized near the y -boundaries. The coefficients c_1 and c_3 of the amplitude equations are near the $c_1 = -c_3$ line (see figures 2-4 and 2-10). For all system parameters that we investigated, $g_2 < g_0$ (see figure 2-10), and therefore the convection occurs in two counter-propagating traveling waves (see figure 2-9), that are localized near the opposite y -boundaries and which have only weak interaction.
- **branch 2:** This is the branch that is relevant for σ around 0.15 and rotation-rates

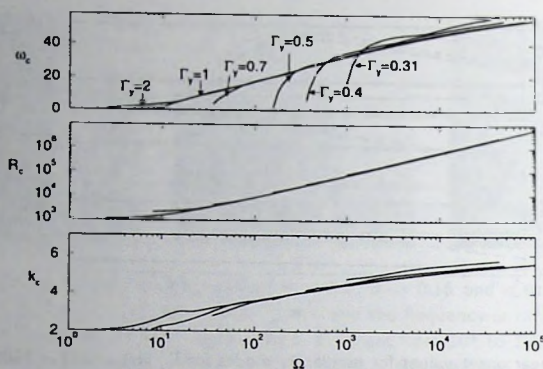


Figure 2-8. The linear onset values for branch 1 are plotted as a function of the rotation-rate Ω for $\sigma = 6.7$ and a number of values of the width Γ_y

around 1000. This mode extends throughout the convection cell (see figure 2-13) and can be seen as a finite size modification of the bulk-modes that occur in an infinite layer [3]. It constitutes the primary mode for $140 < \Omega < 5600$ (see figure 2-11). The coefficients c_1 and c_3 can be tuned over a wide range by the rotation-rate (see figures 2-4 and 2-12). For the system parameters that we considered, $g_2 > g_0$ (see figure 2-12) and the left- and right-traveling modes suppress each other. Under certain conditions, a description in terms of a single CGLE should be sufficient (see chapter 1).

- **branch 3:** This branch of solutions has similar properties as branch 2, but we did not find system parameters such that it has lower critical Rayleigh number than branch 2. Although this mode is not relevant for experiments, we include it here, since for fixed values of the Prandtl number, branch 2 and branch 3 are born together in a tangent bifurcation when Ω is increased (see below).

2.5.3 Prandtl number $\sigma = 6.7$.

For a Prandtl number of 6.7, which corresponds to water at room temperature, the primary mode is branch 1. The linear onset values for this mode are quite insensitive to the precise value of the Prandtl number, as shown in figure 2-8. In fact, we found that the results for all Prandtl numbers larger than 0.2 are similar, and the case studied here represents this.

The effect of the width of the annulus on the linear onset values is illustrated in figure 2-8. The most prominent feature here is the dependence on the width of the channel of the rotation-rate Ω_0 where $\omega_c \downarrow 0$. The value of Ω_0 is connected to the y -dependence of the linear modes (2.3.6) as we will show below. The y -dependence of the linear modes is given by $\sum_{i=1}^8 a_i h_i^j e^{\lambda_i y}$ and the eigenvalues come in pairs $(\lambda, -\lambda)$ (see section 2.3). A measure

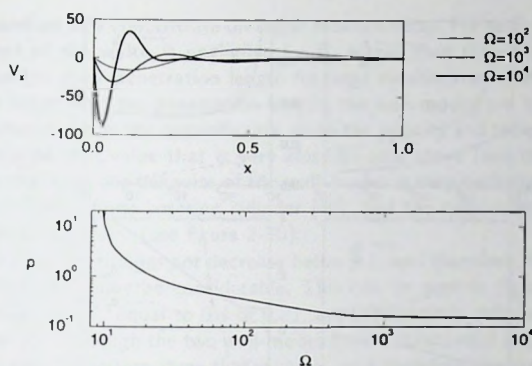


Figure 2-9. Upper panel: plots of v_x , at $x = t = z = 0$, as a function of y , for a channel of width 1, and Prandtl number 6.7. This plot concerns a single wall-mode; in the experiments, double modes will be observed. Note that the convection becomes more and more localized when the rotation-rate is increased. This can be seen more clearly from a plot of the penetration length as a function of Ω . At $\Omega \approx 600$, two pairs of eigenvalues have the same absolute values for their real parts, and one pair is relevant below, and the other is relevant above $\Omega \approx 600$; therefore, the curve of p around $\Omega \approx 600$ is non-smooth.

for the extension of the modes in the y -direction are the real parts of the eigenvalues λ . Defining λ_0 as the eigenvalue which real part is smallest in absolute value, we define the penetration length p as $1/\text{Re}(|\lambda_0|)$. Although the eigenvalues are determined *before* the boundary conditions on the vertical walls are applied, the penetration length of a linear mode depends implicitly on Γ_y via the dependence of the linear onset values on Γ_y . In figure 2-9 we have plotted the penetration length p as function of the rotation-rate for $\Gamma_y = 1$.

When the penetration length p of a certain mode diverges when Ω is decreased, as shown in the lower panel of figure 2-9, this has as a consequence that the frequency of that mode goes to zero. This can be understood as follows. When $p \rightarrow \infty$, by definition one pair of eigenvalues has its real parts going to zero. The eigenvalue equation is, as we have explained in section 2.3, a polynomial in $k^2 - \lambda^2$. When λ is purely imaginary, the eigenvalue equation is precisely the dispersion relation obtained by Chandrasekhar [3] for an infinite layer. This is not surprising, since bulk-modes have an infinite extension in the y -direction, and therefore in a sense have $p \rightarrow \infty$. The dispersion relation does not allow for the occurrence of oscillatory modes when $\sigma > 1$ (see the discussion at the end of section 2.3). Therefore, we conclude that when the penetration length diverges, ω has to go to zero when $\sigma > 1$. In other words, the value of Ω_0 is determined by the divergence of p .

For an infinitely large rotating cylinder, ω_c is approximately linear in $\Omega - \Omega_0$ for small

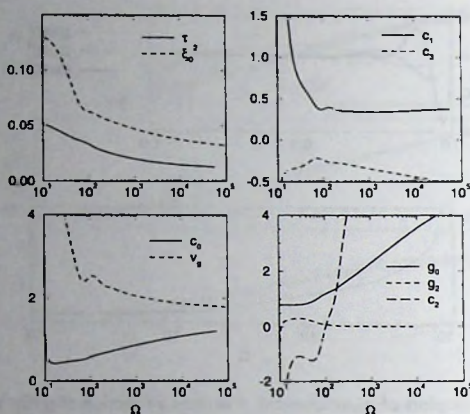


Figure 2-10. The coefficients of the coupled CGLE's (2.4.1) for a Prandtl number of 6.7 and width 1, as a function of the rotation-rate. The cross-coupling coefficients g_2 rapidly goes to zero when the rotation-rate is increased. The divergence of c_2 for increasing values of Ω is without consequences, since the product of g_2 and c_2 goes to zero there.

frequencies [40], while in the rotating annulus ω_c is approximately given by a square-root dependence, $(\Omega - \Omega_0)^{1/2}$. Note that when the width is sufficiently large, this square-root behavior only occurs over a very small range of rotation-rates; for $\Gamma_y > 0.5$ it is not visible in figure 2-8. The difference between linear and square-root behavior is a consequence of the difference in boundary conditions between the infinite rotating cylinder and annulus. For the annulus, the calculations for the linear onset values are completely smooth and arguments from general bifurcation theory yield that ω should have a square-root behavior around the bifurcation. For the infinitely large cylinder, however, only 4 of the 8 eigenvalues λ , i.e., only those with $\text{Re}(\lambda) < 0$, may occur to avoid divergencies when $y \rightarrow \infty$. When the real part of one of these eigenvalues goes through zero as a function of Ω , this eigenvalue is replaced by its opposite twin, and this is clearly a non-smooth process. Therefore, the bifurcation arguments can not be applied and as a consequence, ω may go to zero linearly as a function of the rotation-rate. It should be noted that for finite cylinders, traveling waves occur for any non-zero rotation-rate, i.e., $\Omega_0 = 0$, and the critical frequency ω_c is approximately linear in Ω [38, 43]. The effect of the finite curvature on the bifurcation structure is therefore considerable for small values of Ω , and we would not be surprised when it turns out that for a rotating annulus of finite radius, Ω_0 also goes to zero.

In conclusion: the behavior for small Ω has a strong dependence on the geometry of the convection system. However, as we have indicated in section 2.5.1, this regime is dominated by the stationary bifurcation.

We will therefore now concentrate on larger rotation-rates. For sufficiently large values of Ω , the effect of the width is negligible for Γ_y larger than 0.5, and this is a simple consequence of the short penetration length for large rotation-rates. When the width of the annulus is larger than the penetration length, the wall-modes are quite insensitive to the boundary conditions on the opposite side, since the velocity and temperature-deviation fields have decayed to a value that is very close to zero there (see the upper panel of figure 2-9). In that case the behavior of the wall-modes is very similar to the behavior of a single mode in the infinite rotating cylinder [40], and the cross-coupling between the two amplitudes goes to zero (see figure 2-10).

The penetration length does not decrease below 0.1, and therefore, for small channels, the effect of the width may be considerable. This can be seen in figure 2-8, where the linear onset values, for Γ_y equal to 0.4 or 0.31, are substantially different from the onset values for larger Γ_y . Although the two wall-modes have a substantial overlap for $\Gamma_y \leq 0.4$, calculations of the coefficients show that $g_0 > g_2$, and therefore the system is still in the bimodal regime. It is conceivable that when Γ_y is much smaller, we might enter the single mode regime (i.e., $g_0 < g_2$); from the data presented in figure 2-8 we expect that in such case the convection only occurs for very high rotation-rates and Rayleigh numbers.

The coefficients of the amplitude equations for $\sigma = 6.7$ and $\Gamma_y = 1$ are shown in figure 2-10. Note that the divergencies of the coefficients that occur when Ω is decreased, can not be observed in an experiment, since for $\Omega < \Omega_c \approx 27.5$ the stationary bifurcation is the primary bifurcation.

There are two main features of the coefficients that should be noted. The first feature that is clearly visible in figure 2-10 is the weak dependence of the coefficients on the rotation-rate for $\Omega > \Omega_c$. The only exception is formed by the logarithmic growth of g_0 with increasing Ω . Since $g_0 \gg g_2$, this has no qualitative consequences for the patterns formed in the experimental system; the value of g_0 only determines the ratio of conducted to convected heat, the so-called Nusselt number (see the discussion in section 2.4). The "tuning" of the coefficients by the rotation-rate is only marginal here.

The most important feature is that $c_1 \approx -c_3$ for all values of the rotation-rate. From the point of view of the amplitude equations, the wall-modes in an annulus with a fluid of Prandtl number 6.7 do not have many interesting features.

Of course, we have performed extensive searches in parameter space to search for more interesting behavior of the coefficients c_1 and c_3 , but it turns out that for all Prandtl numbers larger than 0.2, branch 1 is relevant, and the behavior of the coefficients of the CGLE's is very much like that shown in figure 2-10.

2.5.4 Prandtl number $\sigma = 0.15$.

As we have discussed in section 2.5.2, branch 2 becomes relevant for values of σ below 0.2, while for $\sigma < 0.1$ many branches may become relevant. Since we have seen in the previous section that branch 1 is not a very interesting from the point of view of the amplitude equations, we want to focus here on branch 2. We therefore fix σ at a value of 0.15, and, as before, take $\Gamma_y = 1$. For these values of the system parameters we will

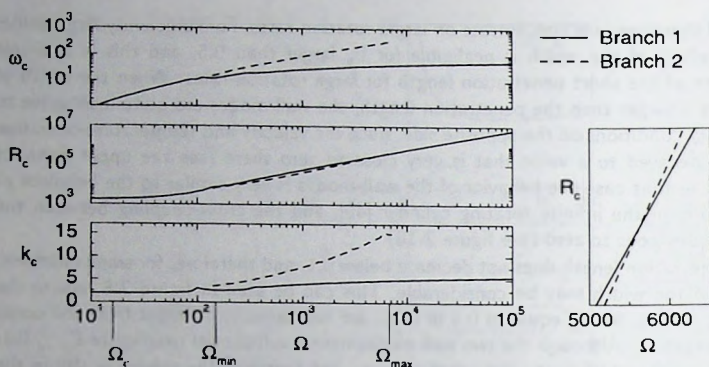


Figure 2-11. The linear onset values of branch 1 and branch 2 for a Prandtl number of 0.15 and a width of 1.

first discuss the competition between branch 1 and 2. Then we present the results of the calculations for the coefficients of the CGLE's. We discuss the geometry of the convection modes for values of Ω where branch 1 to branch 2 interchange to be the primary modes. We conclude by a discussion of the generality of these results.

From the results of the linear stability analysis, as shown figure 2-11, we conclude that for increasing Ω , four regimes of different primary bifurcations occur. Analogous to the case of higher Prandtl numbers, we first encounter a regime where the stationary bifurcation is the primary bifurcation; this is the case for $\Omega < \Omega_c \approx 16.5$. When we increase Ω beyond Ω_c , branch 1 is the relevant branch. At $\Omega = \Omega_{min} \approx 140$, branch 2 and 3 are born via a tangent bifurcation, and the critical Rayleigh number of branch 2 (which we refer to as R_2) is then immediately smaller than the critical Rayleigh number of branch 1, (R_1). For example, for $\Omega = 141$, $R_1 \approx 7400$, while $R_2 \approx 6500$. When Ω is increased further, the difference between R_1 and R_2 increases substantially; the logarithmic scale of figure 2-11 tends to obscure this, but for $\Omega = 1000$ for example, $R_1 = 5.8 \cdot 10^4$ while $R_2 = 4.2 \cdot 10^4$. Eventually, the difference between R_1 and R_2 decreases, and for $\Omega > \Omega_{max} \approx 5600$, R_1 is smaller than R_2 again, and branch 1 is the primary mode for all values of Ω above Ω_{max} .

The coefficients of the amplitude equations for branch 1 and $\Omega > \Omega_{max}$, are similar to the coefficients that we find for branch 1 for higher Prandtl numbers. The essential features are again that g_0 is much larger than g_2 and $c_1 \approx -c_3$. In the other regime where branch 1 is relevant, i.e., $\Omega_c < \Omega < \Omega_{min}$, there appears to be a tiny regime, close to Ω_{min} , where the coefficients c_1 and c_3 might move away from the dissipative limit; however, the numerics are not decisive here.

The coefficients of the amplitude equations for branch 2, are shown in figure 2-12. The first thing to note is that the cross-coupling g_2 is always larger than g_0 , which means

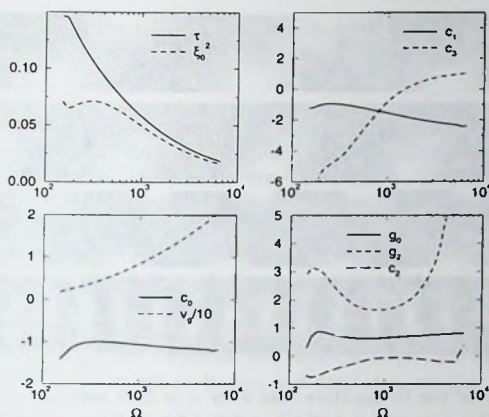


Figure 2-12. The coefficients of the CGLE's for a Prandtl number of 0.15 and a width of 1, as they occur for branch 2.

that the left- and right-traveling wave suppress each other. Note that for a single wave the value of c_2 is immaterial, since terms of the form $|A|^2B$ or $|B|^2A$ are zero. This is reminiscent of the binary fluid convection where the convection patterns consist of a juxtaposition of left- and right-traveling waves. By careful adjusting the initial conditions one may have the convection to be exclusively consisting of either left- or right traveling waves, which warrants a description with a single CGLE.

The right upper panel shows that the coefficients c_1 and in particular c_3 have a strong dependence of the rotation-rate. For $\Omega \rightarrow \Omega_{max}$, c_1 and c_3 are close to the relaxational limit. When the rotation-rate is decreased c_3 changes sign, and at $\Omega \approx 1050$, the Newell criterion is reached ($c_1c_3 = 1$). A further decrease of the rotation-rate pushes the coefficients deep into the spatio-temporal chaotic regime.

Note again, that for this system we have a supercritical bifurcation, while for the binary fluid convection one has a subcritical bifurcation (see chapter 1). To the best of our knowledge, our calculations predict the rotating annulus to be the first experimental realization of a supercritical CGLE with tunable coefficients.

Branch 2 is a bulk-mode in the sense that the convection is not localized near the y -boundaries, but occurs throughout the cell. This is indicated in figure 2-13, where we compare the geometry of branches 1 and 2 for rotation-rates around Ω_{min} and Ω_{max} . These geometries are quite different, in particular around Ω_{max} . The asymmetry of the bulk-mode that can be seen in the second panel of figure 2-13 decreases rapidly when the rotation-rate is increased.

We conclude this presentation of the data for branch 2 at $\sigma = 0.15$ and $\Gamma_y = 1$ with a discussion of its relevance for nearby values of the system parameters σ and Γ_y . The

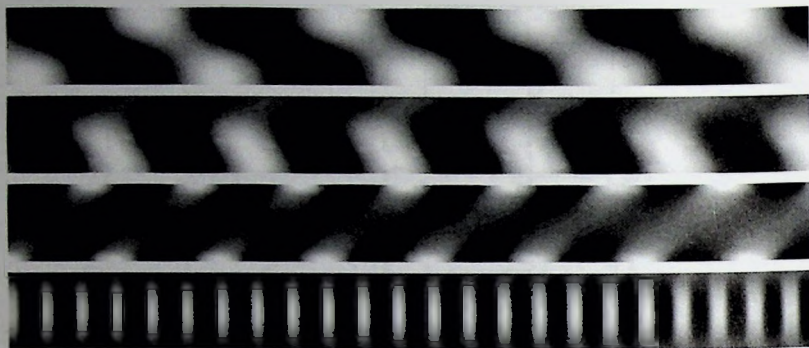


Figure 2-13. Topview of the temperature field θ for $\sigma = 0.15$ and $\Gamma_y = 1$ for four different cases. The value of the z -coordinate is fixed at $1/2$, while x (horizontal scale) ranges from 0 to 10 and y (vertical scale) ranges from 0 to 1. The upper two panels concern the geometry of branch 1 and branch 2 for $\Omega \approx \Omega_{min}$. The first panel shows the two counter-propagating wall-modes (branch 1) that occur for $\Omega < \Omega_{min}$. The wall-mode at $y = 1$, i.e., at the top of this plot, corresponds to the right-traveling wave, while the wall-mode at $y = 0$ (bottom of the plot) corresponds to the left-traveling wave. The second panel shows a left-traveling bulk-mode (branch 2) for $\Omega \approx \Omega_{min}$. Note that this mode is not completely symmetric in the y direction. The third and fourth panel show the wall-modes and bulk-mode for $\Omega \approx \Omega_{max}$ respectively. Note that the wall-modes are now very clearly localized near the y -boundaries, whereas the bulk-mode is now very symmetric as a function of y .

effect of the width of the annulus on both the linear onset values and the coefficients of the amplitude equations is marginal. In particular, we have checked that for larger values of the width, $g_2 > g_0$ for branch 2. The Prandtl number mainly determines Ω_{min} and Ω_{max} ; for instance at $\sigma = 0.175$, $\Omega_{min} \approx 200$ while $\Omega_{max} \approx 3000$. For σ below 0.15, Ω_{min} decreases and Ω_{max} increases, where the latter effect is most prominent. The coefficients of the amplitude equations change of course, but this change is not qualitative, in the sense that Ω still makes the coefficients vary over a wide range. When σ is of the order of 0.1, new branches appear to become relevant; we have not studied this in detail.

2.6 Conclusion.

As we have shown above, Rayleigh-Bénard convection in a rotating annulus has a unique combination of attractive properties. The most prominent features are summarized below.

- The underlying basic equations for this system, i.e., the Navier-Stokes equations, are considerably simpler than the basic equations for convection in binary liquids

or liquid crystals. In the latter case, the underlying basic equations are quite complicated, and one is often forced to use approximations to the full equations of motion.

- The qualitative and quantitative features of the convection modes depend on the Prandtl number of the fluid and the width of the annulus, which both are fixed in an experiment, and on the rotation-rate, which can be adjusted freely.
- The onset of convection can occur both via a stationary bifurcation towards stationary waves, or via a Hopf bifurcation towards traveling waves. For fixed Prandtl number and width of the channel, the rotation-rate determines which of these bifurcations is the primary bifurcation; when the rotation-rate is not too small, the Hopf bifurcation is relevant. In analogy to the study of the co-dimension-2 points that occur in binary liquid convection [41], one can adjust the rotation-rate to study the competition between the stationary and oscillatory modes.
- The onset of convection occurs via a forward bifurcation, which warrants a description with cubic amplitude equations. As we have discussed in chapter 1, for backward bifurcations, like those in binary liquids, amplitude equations can at most give a qualitative description of the patterns. In contrast, for the rotating annulus the amplitude equations should give a complete description of the patterns close to onset.
- The quasi one-dimensional geometry of the system warrants a description in terms of one-dimensional amplitude equations, for both the intrinsic one-dimensional wall-modes and the intrinsic two-dimensional bulk-mode. It should be noted that the annular geometry has been the preferred geometry for many convection experiments in binary liquids.
- When the primary mode is a Hopf mode, the amplitude equations are complex Ginzburg-Landau equations and the rotation-rate of the annulus can be adjusted to vary the all-important coefficients c_1 and c_3 .
- For small values of the Prandtl number, various branches of solutions compete, and the rotation-rate can be adjusted to study this.
- As a function of the rotation-rate, the coefficients of the amplitude equation range from almost dissipative to deep into the spatio-temporal regime, for suitable chosen Prandtl number.

In comparison, the much studied case of binary liquid convection has a backward bifurcation, and its coefficients can only be adjusted by a change of the convection fluid. Moreover, a single amplitude equation description can not account for some of the essential features in binary liquid convection since there is an additional slow mode [35] (see chapters 1 and 4).

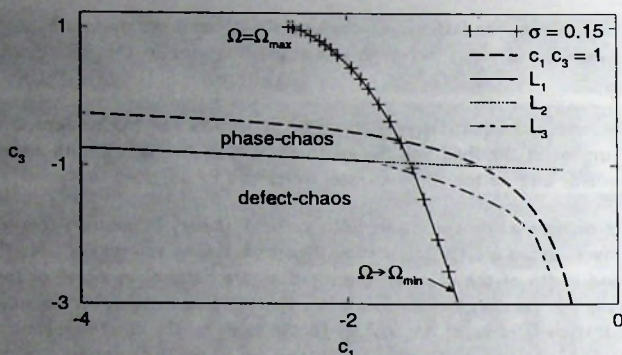


Figure 2-14. The coefficients c_1 and c_3 of the CGLE for $\Gamma_y = 1$ and $\sigma = 0.15$. The curves L_1, L_2 and L_3 indicate the location of various transitions that occur in the spatial-temporal chaotic states of the CGLE [10, 30] (see chapter 1). The regime bordered by L_2, L_3 and the Newell-curve $c_1 c_3 = 1$ is known as the bi-chaotic regime, where phase- and defect-chaos coexist. As a function of the rotation-rate, the coefficients of the CGLE traverse all the different regimes.

We would like to conclude by stressing again the fact that this system gives an experimental realization of the CGLE where the coefficients are deep in the spatio-temporally chaotic regime, as shown in figure 2-14. Despite considerable effort to understand spatio-temporal chaos [10, 30, 47], many aspects of this disordered states are still understood poorly (see chapter 1). Although many of the theoretical studies focus on a single cubic one-dimensional CGLE, there are, to the best of our knowledge, no well controlled experiments that can be described by this amplitude equation and for which the coefficients are calculated and attain values in the regime where spatio-temporal chaos occurs. For instance, for binary liquid convection, it is hard to decide which aspects of the experimentally observed chaos [47] can be described by the quintic CGLE, and which aspects are connected to physically relevant effects that are not captured in an amplitude description.

In conclusion, we wish to express our hope that the experimental study of chaotic convection, as it occurs in the rotating annulus, proves to be a valuable tool in the study of spatio-temporal chaos.

3 A domain-wall between single-mode and bimodal states.

The amplitude equations in the vicinity of a forward Hopf bifurcation are, in general, two coupled CGLE's (1.4.19) (see Chapter 1). Suppose that the linear growth-rate ε is positive. When the coupling coefficient g_2 is sufficiently large, the amplitudes A and B suppress each other, and the system evolves to a state that consists of patches where either A or B is zero (see Chapter 1). For small coupling coefficient however, both amplitudes are nonzero, and when both A and B are simple phase-winding solutions with equal wavenumber, $|A|$ and $|B|$ are equal; we refer to these states as bimodal states. The bifurcation from single mode to bimodal behavior occurs when g_2 is equal to one.

In this chapter, we consider the case that g_2 is a function of the spatial coordinate x . In particular, we focus on the case that $g_2(x)$ is slightly above 1 for $x \rightarrow -\infty$ and slightly below 1 for $x \rightarrow \infty$. The simplest state that can occur in this case is a spatial juxtaposition of a single and a bimodal state, separated by a so-called domain-wall. We study this domain-wall both in the CGLE's and in simplified models. We show that non-variational effects can destroy the stationary domain-wall and study the dynamical states that occur in this case. In particular we focus on the effect of the group-velocity terms in the coupled equations.

This chapter is organized as follows. First we introduce a simplified model for the occurrence of domain-walls. For stationary solutions of this model we derive a perturbation equation that allows us to predict the vanishing of stationary domain-walls when the group-velocity is sufficiently large. This is confirmed by numerical simulations of this model, and we describe the ensuing dynamical states. We study the relevance of this model for coupled RGLE's and CGLE's by performing numerical simulations. In particular for the CGLE, a broad spectrum of dynamical behavior is observed, including spatio-temporal chaos. It is very difficult to characterize these states, and we restrict ourself to a limited exploration of the possible dynamical states.

3.1 Introduction.

Some of the essential features of the CGLE's that are important in the study of the domain-wall, i.e., the stability of the single and bimodal states as a function of the coupling coefficient g_2 , can also be studied in simpler models. In the simplest approach, we take the coefficients c_i equal to zero and the amplitudes real-valued:

$$\partial_t A + v_g \partial_x A = A + \partial_x^2 A - (A^2 + g_2(x)B^2)A, \quad (3.1.1a)$$

$$\partial_t B - v_g \partial_x B = B + \partial_x^2 B - (B^2 + g_2(x)A^2)B, \quad (3.1.1b)$$

and we will refer to these equations as the NLDE's (nonlinear diffusion equations). These equations have no direct physical interpretation in terms of amplitude equations, but they have the advantage over more realistic models that the effect of the group-velocity terms on the domain-walls can be studied analytically. Since the group-velocity terms have opposite sign for the A and the B equation of the coupled CGLE's, we retain this property in the NLDE's. Without the cross-coupling, the group-velocity terms generate a counter propagation of the patterns in A and B . When the equations for A and B are coupled, the effect of the group-velocity terms can not be given in terms of a simple propagation rule. To study the consequences of the group-velocity, we derive, for stationary configurations, a single ordinary differential equation for the order parameter $\chi := \arctan(B/A)$. We will investigate the existence of a stationary domain-wall in this equation analytically.

In section 3.2 we consider the case that the group-velocity terms are absent. The equations are then variational, and, in the particular case that the coupling coefficient is proportional to $\tanh(\kappa x)$, an exact analytical solution for the domain-wall can be obtained. Next, we extend in section 3.3 the equation for χ to include the group-velocity terms and when we take the coupling coefficient to be a step function, an analytical solution can be constructed. Analyzing the latter solution, we find a bifurcation from a regime where the domain-wall is stationary to a regime where no stationary domain-wall exists. This transition, which we show to have a nice geometrical interpretation, occurs when the group-velocity v_g is equal to $\pm 2\sqrt{|g_2 - 1|}$. We will discuss the validity of this result for more general forms of $g_2(x)$. Direct simulations of the NLDE's show that there is a value of the group-velocity, v_i , where the stationary domain-wall loses its stability. This instability occurs because the position of the domain-wall diverges when v_g approaches v_{crit} . The difference between v_{crit} and v_i is of the order of a few percent. For a group-velocity just beyond v_i , the domain-wall is seen to perform small-amplitude disordered oscillations around a mean position, without essentially disturbing the shape of the domain-wall.

For the NLDE's (3.1.1) the bifurcation of the stationary domain-wall is predicted analytically and confirmed to exist numerically. The study of the coupled CGLE's is of a more explorative nature. As a first step towards the study of the full coupled CGLE's, we allow the amplitudes A and B to be complex valued. These equations are reminiscent of the RGLE, but it should be noted that in physical applications, the RGLE has no group-velocity terms; nevertheless we refer to this model as the coupled RGLE's. We explain that the main properties of the stationary domain-walls in this model can be described by the NLDE's. Simulations of coupled RGLE's, presented in section 3.4, show a transition between the stationary domain-walls and a dynamical state with the increase of the group-velocity that is similar to the NLDE-case. The role of wavenumbers of the initial conditions, which constitutes the main feature that is not present in the NLDE's, is discussed briefly.

For the coupled CGLE's, the numerical results presented in section 3.5 show that the nonlinear dispersion terms render the domain-walls unstable, including the case when the group-velocity terms are absent. Spatio-temporal disordered states often occur, even when the asymptotic plane-wave states are stable. This instability can be understood qualitatively to arise from the large gradients of $|A|$ and $|B|$ around the domain-wall.

It may be pertinent to note that both complex and real Ginzburg-Landau equations with the coefficients in front of the *linear* terms smoothly depending upon the spatial coordinates have been a subject of many studies [48, 49, 50]. It was found that a parameter ramp in the real or complex Ginzburg-Landau equation can perform wavenumber selection [48, 49]. In the case of the full complex equation, it can also render the single-mode traveling waves unstable, and can trap subcritical pulses [50]. However, to the best of our knowledge, there have been no studies aimed to consider effects of a spatial dependence in the coefficient in front of the nonlinear coupling term.

A spatially dependent coupling coefficient as considered here can be realized for instance in Rayleigh-Bénard convection in a large-aspect-ratio cell. In this case, the two modes are two orthogonal sets of parallel rolls. A single-mode state is stable provided that an effective coupling coefficient between the orthogonal rolls is larger than a certain minimum value, while in the opposite case a square-lattice pattern (the bimodal state obtained as a superposition of two orthogonal sets of rolls) is stable [51]. Usually, the actual value of the coupling coefficient is well above the above-mentioned minimum, so that the square lattice is unstable. However, in special cases, e.g., for the convection between horizontal surfaces with poor heat conductivity, the coupling coefficient may fall below the minimum [52]. One may construct a suitable inhomogeneous system, for example, by means of a variable-thickness lid put on top of the convection layer, such that the local coupling coefficient, being a function of the spatial coordinates, is passing through the minimum value. Then one may expect a stationary domain-wall separating the rolls and square lattice, which is impossible in the homogeneous system [53, 54]. The group-velocity terms are not present in the amplitude equations for this system.

The CGLE's that describe Rayleigh-Bénard convection in a rotating annulus (see chapter 2), can have a spatial modulation of the cross-coupling, by varying the width of the annulus. However, we have yet to find system parameters for which the cross-coupling is close to its critical value, which is a necessary condition for the occurrence of the domain-walls that we study here.

3.2 The variational case.

In this section we will focus on the NLDE's and RGLE's, which are the simplest sets of equations where a domain-wall between a single-mode and a bimodal state can occur. The dynamics without the group-velocity terms are relaxational in the sense that a Lyapunov functional \mathcal{L} exists for both of these models, which allows the prediction of final states by minimizing \mathcal{L} . We derive a perturbation theory for a weak inhomogeneity in the cross-coupling coefficients of the NLDE's, that allows us to find a closed-form expression for the domain-wall for a special choice of the inhomogeneity. This perturbation theory will be a starting point in the next subsection, where we will focus on the effect of the group-velocity terms that break the variational structure.

The equations that we consider in this section are

$$\partial_t A = A + \partial_x^2 A - (|A|^2 + g_2(x)|B|^2)A, \quad (3.2.1a)$$

$$\partial_t B = B + \partial_x^2 B - (|B|^2 + g_2(x)|A|^2)B, \quad (3.2.1b)$$

where A and B are real-valued for the nonlinear diffusion equations, and complex in the RGLE. The critical value of g_2 is 1: for $g_2 < 1$ the bimodal state $|A| = |B| = \sqrt{1/(1+g)}$ is stable, whereas for $g_2 > 1$ this bimodal state loses its stability and the single-mode state with $|A| = 1$ and $B = 0$ (or vice versa) becomes stable [55]. The coupling coefficient $g_2(x)$ is assumed to decrease monotonically from slightly above to slightly below its critical value as a function of the spatial coordinate x . We will set $g_2(x) := 1 + \gamma(x)$, where $\gamma(x)$ is a small monotonically decreasing function of the spatial coordinate x , such that $\gamma(x)$ is positive at $x < 0$ and negative at $x > 0$. We assume that $\gamma(x)$ saturates at $x \rightarrow \pm\infty$, i.e., it assumes certain asymptotic values $\gamma(-\infty) = \gamma_{max} > 0$, and $\gamma(+\infty) = \gamma_{min} < 0$. The solution that one expects for this choice of $g(x)$ is a stationary domain-wall located around $x = 0$ which matches the single-mode and bimodal states existing, respectively, for negative and positive x .

The coupled RGLE's can be derived from the Lyapunov functional

$$\mathcal{L} = \int dx (|\partial_x A|^2 + |\partial_x B|^2 - (|A|^2 + |B|^2) + \frac{1}{2}(|A|^4 + |B|^4) + (1 + \gamma(x))|A|^2|B|^2), \quad (3.2.2)$$

by setting $\partial_t A = -\delta\mathcal{L}/\delta A^*$ and $\partial_t B = -\delta\mathcal{L}/\delta B^*$. As discussed in chapter 1, the Lyapunov functional can only decrease in time, and, as it is bounded from below, a final state corresponds to a minimum of \mathcal{L} . The final state that corresponds to a global minimum of \mathcal{L} has a zero wavenumber, which suggests to consider also the particular case of real A and B . Thus one obtains the coupled nonlinear diffusion equations that we will refer to as the NLDE's. For finite systems with periodic boundary conditions, the RGLE's may evolve to stationary states with nonzero wavenumber. This is discussed in section 3.4.

We will now focus on the stationary solutions of the NLDE's, and set the derivatives with respect to time equal to zero in the NDLE's (3.1.1). The ensuing equations can be written as four coupled ordinary differential equations for A , $\partial_x A$, B and $\partial_x B$. When we identify A and B with position coordinates and their derivatives with generalized momentum coordinates, the equations for a stationary domain-wall can be written as the *Hamilton equations* corresponding to the Hamiltonian

$$H = \frac{1}{2}((\partial_x A)^2 + (\partial_x B)^2 + (A^2 + B^2) - \frac{1}{2}(A^2 + B^2)^2 - \gamma(x)A^2B^2), \quad (3.2.3)$$

where x is the "time" coordinate. Although the Hamiltonian is similar to the Lyapunov functional, the difference in the signs that occur in these expressions should be noted.

In general we can not solve the Hamilton equations for arbitrary $\gamma(x)$. To proceed we will develop a perturbation expansion by taking γ_{min} and γ_{max} small. We will complement this condition by the assumption that $A(x)$ and $B(x)$ are slowly varying functions of x ,

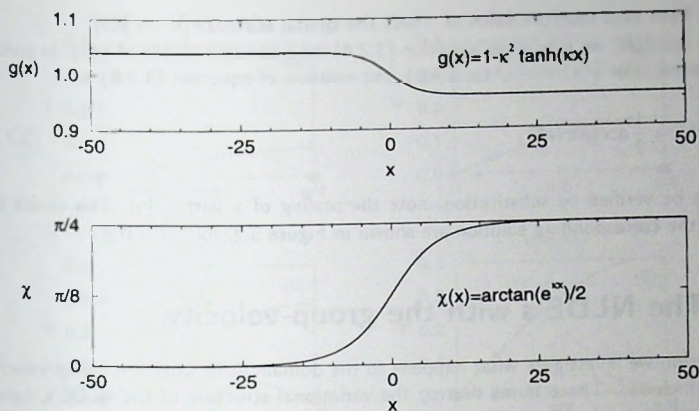


Figure 3-1. The exact domain-wall solution (3.2.7) to the reduced NLDE's without the group-velocity terms, when the inhomogeneity is chosen as $\gamma(x) = -\kappa^2 \tanh(\kappa x)$, with $\kappa = 0.2$.

so that the diffusive terms in equations (3.2.1) are small in comparison with the other terms. Below we will determine, in a self-consistent way, that the spatial scale L over which A and B vary is of order $1/\sqrt{|\gamma|}$.

When the diffusive terms and the coupling term $\gamma(x)A^2B^2$ of the Hamiltonian (3.2.3) are small, it follows that $(A^2 + B^2)$ is almost constant. This suggests the following representation for $A(x)$ and $B(x)$ [53]:

$$A(x) = R(x) \cos \chi(x); \quad B(x) = R(x) \sin \chi(x). \quad (3.2.4)$$

The single-mode states have $\chi = n\pi/2$, while the bimodal states have $\chi = \pi/4 + n\pi/2$ (throughout this chapter, n will represent an integer). When we substitute this representation into the Hamiltonian (3.2.3) we obtain

$$H = R^2 - \frac{1}{2}R^4 + R^2 + R^2\chi'^2 - 4RR'\chi' \cos(\chi) \sin(\chi) - \gamma(x)R^4 \cos^2(\chi)^2 \sin^2(\chi)^2, \quad (3.2.5)$$

where a prime denotes differentiation with respect to x . Stationary solutions of the coupled NLDE's are found by determining the minima of the Hamiltonian (3.2.3). Since we assumed that A and B are slowly varying, and that R is almost constant, $R' \ll \chi'$ and in the simplest non-trivial approximation we may set R equal to one. Differentiating the Hamiltonian (3.2.5) with respect to x and neglecting higher order terms, we obtain the following perturbation equation:

$$\chi''(x) = \frac{1}{4}\gamma(x) \sin(4\chi). \quad (3.2.6)$$

It follows from here that the value of γ sets the spatial scale: $L^{-2} \sim \gamma$ [53].

As an example, we may solve equation (3.2.6) for a suitable choice of $\gamma(x)$. In particular, when we take $\gamma(x) = -\kappa^2 \tanh(\kappa x)$, the solution of equation (3.2.6) is

$$\chi_0(x) = \frac{1}{2} \arctan(e^{\kappa x}), \quad (3.2.7)$$

which can be verified by substitution; note the scaling of x with $\sqrt{|\gamma|}$. This choice for $\gamma(x)$ and the corresponding solution are shown in Figure 3.2, for $|\gamma| = 0.2$.

3.3 The NLDE's with the group-velocity.

In this section we investigate what happens to the domain-walls when the group-velocity terms are included. These terms destroy the variational structure of the NLDE's, hence their final states need no longer be stationary. We will show that stationary domain-walls can not exist when the group-velocity is above a certain critical value. Numerical simulations of the NLDE's corroborate this prediction, and show that, beyond this threshold, time-periodic or disordered states occur.

The NLDE's with the group-velocity terms are

$$\partial_t A + v_g \partial_x A = A + \partial_x^2 A - (A^2 + g(x)B^2)A, \quad (3.3.1a)$$

$$\partial_t B - v_g \partial_x B = B + \partial_x^2 B - (B^2 + g(x)A^2)B, \quad (3.3.1b)$$

In analogy with the work by Malomed [56], we use a *balance equation* for the Hamiltonian (3.2.3) to treat effects of the small group-velocity terms on the stationary solutions. Differentiating (3.2.3) and making use of the stationary version of the NLDE's (3.1.1), one finds

$$\frac{dH}{dx} = v_g [(\partial_x A)^2 - (\partial_x B)^2]. \quad (3.3.2)$$

Similar to the derivation of equation (3.2.6), an perturbation expansion of this equation yields at lowest non-trivial order

$$\chi''(x) - \frac{1}{4}\gamma(x) \sin(4\chi) + v_g \chi' \cos(2\chi) = 0. \quad (3.3.3)$$

This equation is the basis for the perturbative analysis presented below. Note that the same equation, albeit for constant γ , was obtained in [56].

It should be noted that this equation is invariant under a scale transformation $\gamma \rightarrow \delta\gamma$, $x \rightarrow x/\sqrt{\delta}$ and $v_g \rightarrow \sqrt{\delta}v_g$. This freedom can in principle be used to scale out v_g , but we will not do this; this scale-invariance is reflected, however, in the formula for v_{crit} that is obtained below.

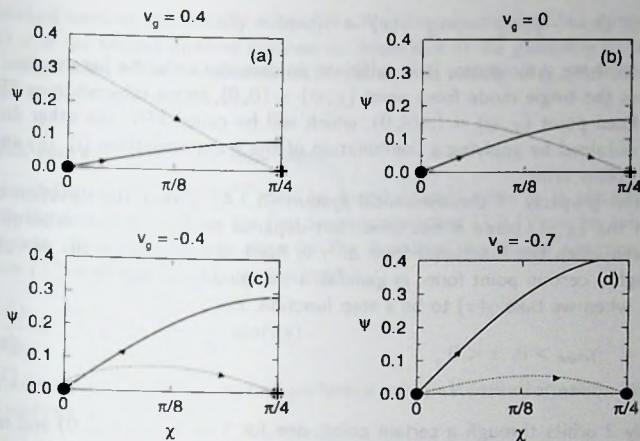


Figure 3-2. Trajectories of the two-dimensional dynamical system (3.3.4) for fixed γ . The fat dots represent the fixed points FP0 and FP1. The bold curve is the manifold $W_0^{(out)}$ that is calculated for $\gamma = \gamma_{max} = 0.1$, while the dashed curve is $W_1^{(in)}$ that is calculated for $\gamma = \gamma_{min} = -0.1$. To obtain the hetero-clinic orbit that arises when $\gamma(x)$ is a step function, start at FP0 and follow $W_0^{(out)}$ until it intersects $W_1^{(in)}$. At this intersection, $x = 0$ and so γ changes from γ_{max} to γ_{min} ; consequently, for $x > 0$, the hetero-clinic orbit follows $W_1^{(in)}$.

3.3.1 Phase-space analysis.

It will be convenient to rewrite equation (3.3.3) in the form of a two-dimensional *non-autonomous* dynamical system:

$$\frac{d\chi}{dx} = \psi, \quad (3.3.4a)$$

$$\frac{d\psi}{dx} = -v_g \psi \cos(2\chi) + \frac{1}{4} \gamma(x) \sin(4\chi). \quad (3.3.4b)$$

Fixed points of equations (3.3.4) are $(\chi = n\pi/4, \psi = 0)$, which correspond to single-mode stationary solutions of equations (3.3.1) at even n , and to bimodal solutions at odd n . Hetero-clinic orbits going from one fixed point at pseudo-time $x = -\infty$ to another fixed point at $x = \infty$ correspond to the domain-walls that we are interested in. Since we have chosen $\gamma(x)$ to be a decreasing function of x , these orbits go from a fixed point with even n to one with odd n .

The system (3.3.4) is invariant with respect to the following symmetry transformations:

(i) $\chi \rightarrow \chi + n\pi$,

(ii) $\chi \rightarrow \chi + \pi/2, v_g \rightarrow -v_g$.

$$(iii) \quad x \rightarrow -x, \psi \rightarrow -\psi, v_g \rightarrow -v_g, \gamma(x) \rightarrow \gamma(-x).$$

With regard to these symmetries, it is sufficient to consider only the hetero-clinic orbit that goes from the single mode fixed point $(\chi, \psi) = (0, 0)$, to be referred to as FP0, to the bimodal fixed point $(\chi, \psi) = (\pi/4, 0)$, which will be called FP1; the other domain-walls can be obtained by applying a combination of the transformations (i), (ii) and (iii) to this hetero-clinic orbit.

An essential property of the dynamical system (3.3.4) is that the direction of the phase-flow in the (χ, ψ) plane is not fixed, but depends on the current value of $\gamma(x)$. Therefore, even when the functional form of γ is fixed, the possible orbits of equation (3.3.4) through a certain point form, in general, a one-parameter family.

However, when we take $\gamma(x)$ to be a step function, i.e.,

$$\gamma(x) = \gamma_{max} > 0, \quad x < 0, \quad (3.3.5a)$$

$$\gamma(x) = \gamma_{min} < 0, \quad x > 0, \quad (3.3.5b)$$

there are only 2 orbits through a certain point; one for $\gamma = \gamma_{max}$ ($x < 0$) and one for $\gamma = \gamma_{min}$ ($x > 0$). Notice that the lack of continuity of $\gamma(x)$ does not contradict the assumption that the stationary solution for χ is a smooth function of x ; we will see below that solutions corresponding to this discontinuous $\gamma(x)$ are smooth indeed. In fact, the scaling properties of equation (3.3.3), that also hold for the dynamical system (3.3.4), yield that when we rescale $\gamma \rightarrow \delta\gamma$, with $\delta < 1$, the function $\gamma(x)$ becomes effectively steeper due to the rescaling of the spatial-coordinate; when $\delta \downarrow 0$, $\gamma(x)$ becomes, in a sense, infinitely small and infinitely steep.

We are now interested in the behavior of the hetero-clinic orbits as a function of v_g . A hetero-clinic trajectory corresponding to the domain-wall exists, provided that the outgoing (unstable) manifold of FP0, which we will refer to as $W_0^{(out)}$, intersects the ingoing (stable) manifold of FP1, to be referred to as $W_1^{(in)}$ (see figures 3-2 and 3-3). $W_0^{(out)}$ and $W_1^{(in)}$ have to be calculated, respectively, for $\gamma = \gamma_{max}$ and $\gamma = \gamma_{min}$. The question of existence of a domain-wall has thus been reduced to checking whether $W_0^{(out)}$ and $W_1^{(in)}$ intersect.

This is illustrated in the figures 3-2 and 3-3, where we have plotted, for $\gamma_{min} = -0.1$ and $\gamma_{max} = 0.1$, these two manifolds for a range of values of the group-velocity. The point of intersection has by definition $x = 0$, and so from these figures we can read off the values of χ and χ' at $x = 0$ as a function of v_g . The point of intersection of $W_0^{(out)}$ and $W_1^{(in)}$ shifts towards FP0 when v_g is decreased. As a consequence, the location of the domain-wall, i.e. the value of x where $\chi = \pi/8$, shifts to larger and larger values. In fact, when v_g approaches certain value which we define as v_{crit} , the intersection of $W_0^{(out)}$ and $W_1^{(in)}$ approaches FP0 and the location of the domain-wall, that corresponds to the hetero-clinic orbit, diverges to infinity (see figure 3-4).

Below we will find that $v_{crit} = -2\sqrt{|\gamma_{min}|}$. Note that the square-root dependence follows from the scaling properties; only the numerical factor -2 needs to be determined. There are two complementary methods for the determination of critical velocity. The

first method involves analytically solving the flow-line equations of the dynamical system (3.3.4), and the second method involves an inspection of the geometry of the flow-lines. After a description of these two methods we discuss the validity of v_{crit} for inhomogeneities that are not of the form (3.3.5).

Analytic expression for the flow-lines.

The manifolds $W_0^{(out)}$ and $W_1^{(in)}$ can be found exactly when γ is piecewise constant, because the flow-line equation for the dynamical system (3.3.4) can be solved explicitly in this case. To obtain the equation for the flow-lines, we divide equation (3.3.4b) by equation (3.3.4a), which yields for constant γ :

$$\frac{d\psi}{d\chi} = -v_g \cos(2\chi) + \frac{\gamma}{4\psi} \sin(4\chi). \quad (3.3.6)$$

To solve equation (3.3.6), we first perform a coordinate transformation by introducing $\zeta := \frac{1}{2} \sin(2\chi)$, which yields

$$\frac{d\psi}{d\zeta} = -v_g + \gamma \frac{\zeta}{\psi}. \quad (3.3.7)$$

This ordinary differential equation is homogeneous, and by defining $\lambda = \psi/\zeta$ and some rewriting, we find

$$\frac{1}{\zeta} d\zeta = \frac{1}{-v_g + \gamma/\lambda - \lambda} d\lambda. \quad (3.3.8)$$

The manifold $W_0^{(out)}$ corresponds to the case that λ is a constant, which occurs for $-v_g + \gamma/\lambda - \lambda = 0$. By transforming this solution back to the χ, ψ coordinates we obtain for $W_0^{(out)}$:

$$\psi = \lambda_0/2 \sin(2\chi), \quad (3.3.9)$$

where λ_0 satisfies $-v_g + \gamma/\lambda_0 - \lambda_0 = 0$, and $\gamma = \gamma_{max}$.

The manifold $W_1^{(in)}$ is found by a straightforward integration of equation (3.3.8), which yields the unpleasant equation

$$\ln(\zeta) = \frac{v_g \operatorname{arctanh} \frac{v_g + 2\lambda}{\sqrt{4\gamma + v_g^2}}}{\sqrt{4\gamma + v_g^2}} - \frac{\ln(-\lambda + v_g\lambda + \lambda^2)}{2} + K, \quad (3.3.10)$$

where K is an arbitrary constant of integration, and $\gamma = \gamma_{min}$. K has to be chosen so that the trajectory is passing through the point FP1, where $(\zeta, \lambda) = (\frac{1}{2}, 0)$. Although we do not have explicit expressions for the manifolds in terms of the original variable χ , we can find from equations (3.3.9) and (3.3.10) under which conditions the manifolds $W_0^{(out)}$ and $W_1^{(in)}$ intersect. The intersection point can be found by substituting $\lambda = \lambda_0$ into the

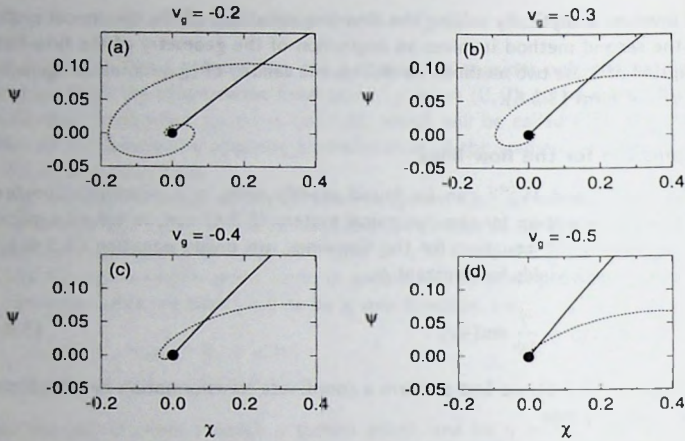


Figure 3-3. The behavior of $W_0^{(out)}$ (bold curve) and $W_1^{(in)}$ (dashed curve) around FP0 (black dot) for a range of values for the group-velocity. In this case we have taken $\gamma_{min} = -0.1$, which yields a critical velocity $v_{crit} \approx 0.632$.

equation for $W_1^{(in)}$ (3.3.10). Simply solving the ensuing equation numerically yields that $W_1^{(in)}$ and $W_0^{(out)}$ intersect only (apart from the intersection at FP0 itself) when

$$v_g > v_{crit} := -2\sqrt{-\gamma_{min}}, \quad (3.3.11)$$

where it should be noted that v_g is assumed to be negative.

This means that if the group-velocity v_g , which is responsible for the non-variational effects in this model, is below the threshold $-2\sqrt{-\gamma_{min}}$, there can not be a stationary domain-wall. It should be noted that we have focused here on the domain-wall that has a single-mode state for negative x and a bimodal state for positive x . When we reflect x , and study a domain-wall of opposite chirality, i.e., going from a bimodal state at $x \rightarrow -\infty$ to a single-mode state at $x \rightarrow +\infty$, according to symmetry (iii) the critical velocity changes sign. When $\gamma(x)$ goes from negative values for $x < 0$ to positive values for $x > 0$, the ensuing stationary domain-walls can not exist for sufficiently large positive v_g . We will encounter domain-walls of both chiralities in the numerical simulations presented below.

Geometrical interpretation.

A simple geometric interpretation of the threshold is illustrated in the figures 3-2 and 3-3.

As is illustrated in the phase-portraits (see Figures 3-2a and 3-2b), $W_1^{(in)}$ intersects $W_0^{(out)}$ for all positive v_g , and therefore we will concentrate now on the case of negative v_g . The central point is that for negative v_g and negative γ , FP0 is a spiral when $v_g > v_{crit}$,

and a saddle when $v_g < v_{crit}$. Therefore, the motion of $W_1^{(in)}$, for which $\gamma = \gamma_{min} < 0$ in the neighborhood of FP0 is spiral-like when $v_g > v_{crit}$; this is not visible on the scale of figure 3-2 but can be seen in figure 3-3.

As long as $W_0^{(out)}$ spirals around FP0, it has to intersect $W_1^{(in)}$, which means that there is a hetero-clinic orbit and therefore a stationary domain-wall. When v_g approaches v_{crit} , this spiraling motion becomes less prominent, and consequently, the intersection of $W_0^{(out)}$ and $W_1^{(in)}$ shifts to FP0 (see figure 3-3). As a consequence, the position of the domain-wall shifts to large values of x .

When v_g has crossed the critical value v_{crit} , FP0 is a saddle and it turns out that $W_0^{(out)}$ and $W_1^{(in)}$ only intersect in FP0 itself (see Figure 3-2d); this corresponds to a domain-wall that is shifted to infinity.

Validity of v_{crit} .

There are two different assumptions involved in the calculation of v_{crit} . First of all, γ needs to be small, in order for the perturbation equation (3.3.3) to hold. Secondly, we used for $\gamma(x)$ a step-function. We will now discuss the validity of v_{crit} when $\gamma(x)$ is of more general form.

The latter assumption is, due to the scaling properties of equation (3.3.3), not crucial, as we have indicated above. When we rescale $\gamma \rightarrow \delta\gamma$, with $\delta < 1$, we can compensate for this by rescaling the spatial coordinate; effectively, the function $\gamma(x)$ becomes steeper then. When $\delta \downarrow 0$, $\gamma(x)$ becomes infinitely small and infinitely steep. Therefore, the results that are obtained when γ is a step-function, are still valid when $\gamma(x)$ is an arbitrary monotonically decreasing function, provided that $|\gamma|$ is small.

It is tempting to try to extend the phase-space analysis to the non-perturbative case, i.e., when γ is not small. In that case we can not use the perturbation equation, and instead have to analyze the stationary version of the full coupled NLDE's (3.3.1), which can be written as a four-dimensional dynamical system. The equations for the trajectories can not be solved in this case, but we can inspect the eigenvalues of the fixed points that correspond to the single-mode and bimodal states. The latter fixed point always has two positive and two negative eigenvalues. The fixed point corresponding to the single-mode state changed from a saddle to a spiral at $v_g = v_{crit}$ in the perturbative case, and something similar happens in the four-dimensional system. The eigenvalues of this fixed point are given by the expressions $\frac{1}{2}(v_g \pm \sqrt{v_g^2 + 8})$ and $\frac{1}{2}(v_g \pm \sqrt{v_g^2 + 4\gamma_{min}})$. One can readily find that, when $v_g = -2\sqrt{-\gamma_{min}}$, this fixed point changes from being a saddle (two negative and two positive eigenvalues) to a fixed point with one positive, one negative and two complex conjugated eigenvalues. This is very similar to what we observed for the fixed points in the two-dimensional dynamical system (3.3.4) The thing that we lack here is a precise understanding of the four-dimensional flow, but the linear analysis is at least an indication that the previously obtained value v_{crit} is also valid when γ and v_g are not small.

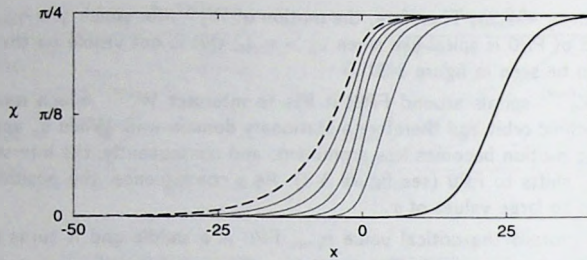


Figure 3-4. The function $\chi(x) = \arctan(B/A)$ corresponding to the domain-wall solutions for various choices of the group-velocity v_g . The domain-walls were obtained by direct simulations of the coupled NLDE's (3.3.1). The inhomogeneity was a step-function for these simulations, and γ goes from 0.1 to -0.1 at $x = 0$. The dashed curve corresponds to the domain-wall for $v_g = 0.6$, while the fat curve corresponds to $v_g = -0.6$. The domain-walls in between correspond to $v_g = 0.4, 0.2, 0, -0.2$ and -0.4 , respectively; the domain-wall shifts to the right when v_g is decreased towards v_{crit} .

3.3.2 Numerical simulations.

To test the validity of the perturbation equation (3.3.3) and to verify our predictions, we have performed numerical simulations of the coupled NLDE's (3.3.1) in a periodic system of size $L = 400$. Because of the periodicity of the system, there are two domain-walls but we will, as before, focus attention on the domain-wall near $x = 0$ that connects a single-mode state ($B = 0$) to the left with a bimodal state to the right. The results reported here were obtained by using a pseudo-spectral code with the time step 0.05 and, typically, 256 modes; runs with a higher number of modes up to 1024 were performed to check the results. The code was such that A and B could be chosen to be either real or complex-valued, in order to simplify the comparison between the results for the NLDE's and the RGLE and CGLE later on.

When $v_g \rightarrow v_{crit}$, the intersection point of the manifolds approaches FP0, and consequently the position of the domain-wall shifts to $+\infty$. In this limiting case, a single-mode state intrudes into the domain with $g < 1$, where it is unstable. Therefore, one might expect that the domain-wall turns unstable when v_g is still slightly above v_{crit} . We find below that this is the case indeed, and we will denote the value of the group-velocity where the domain-wall turns unstable by v_i .

The simulations carried out below focus on three items. First of all, we check that the stationary domain-walls that are predicted by the analysis of the perturbation equation exist and are stable when v_g is not too close to v_{crit} . Subsequently, we determine, for various choices of the inhomogeneity, the value of v_g where the domain-wall turns unstable, and compare it with v_{crit} . Finally, we investigate the dynamical states that occur when v_g is decreased beyond v_i .

Stationary states.

In this section we present the results of the simulations of the NLDE's for $|v_g| < |v_{crit}|$ and the step-like γ . Most of the phase-space analysis presented above was based on the assumption that γ is small and we therefore take $\gamma(x) = 0.1$ at $x < 0$, and -0.1 at $x > 0$; in this case, the critical value of the group-velocity is $v_{crit} = -2\sqrt{-\gamma_{min}} \approx -0.632$.

We have found that for $|v_g| \lesssim 0.6$ the system relaxes to a stationary domain-wall. The domain-walls that were obtained by numerical simulations with 1024 modes are shown in Figure 3-4. The numerical simulations clearly demonstrate that the stationary domain-walls are stable when v_g is not very close to v_{crit} ; this fact can not be derived from the phase-space analysis alone.

Comparing the domain-walls obtained from direct simulations of the NLDE's with those obtained by numerical integration of the ordinary differential equation $d\chi/dx = \psi$ along the analytically obtained flow-lines, we found that the shape of the domain-wall is predicted very well for all values of v_g that we consider here.

The main difference that occurs between the solutions of the full and perturbation equations is the position of the domain-wall; this difference is maximal for $v_g = -0.6$, where it is of order 2. Considering the scale on which the domain-wall occurs (see figure 3-4), this is quite small; for $|\gamma| = 0.1$, the perturbation equation (3.3.3) gives a good description of the domain-walls of the NLDE's.

Instability of the domain-wall

Now that we have checked that the predications that follow from the perturbation theory are correct when v_g is not too close to v_{crit} , we will investigate what happens when $v_g \downarrow v_{crit}$.

The numerical simulations that we will present below reveal that the strength and the steepness of the inhomogeneity, the value of v_g and the initial conditions all may influence the dynamics. To sample the parameter space without going into too much detail, we have eventually restricted ourselves to inhomogeneities of the form

$$g(x) = 1 + \Delta g \tanh(s(x - 0.25L)) \tanh(s(x + 0.25L)) , \quad (3.3.12)$$

where s stands for the steepness of the inhomogeneity and L is the size of the system. The middle part of the system is where the bimodal state exists. We have shifted the inhomogeneities away from $x = 0$ because this makes the pictures for the time evolution of A and B that are presented below more clear.

We take values of the inhomogeneity strength Δg of 0.05, 0.1, 0.2 and 0.3 in order to obtain information on the dependence of the dynamics on the strength of the inhomogeneity. For the steepness s , two different values were selected: 0.1 for a smooth inhomogeneity, and 10 for a steep inhomogeneity; for the numerical simulation presented below, this last value is almost equivalent to a step-like inhomogeneity.

As can be seen in figure 3-4, the location of the domain-wall shifts to larger values of x when v_g approaches v_{crit} , in agreement with the phase-space analysis. In this case, a large patch of the unstable single-mode state intrudes in the $g < 1$ domain. Eventually,

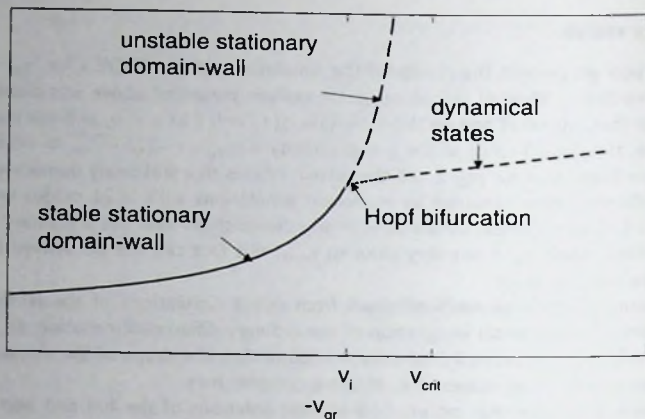


Figure 3-5. Schematic representation of the bifurcation structure as a function of the group-velocity for weak inhomogeneities. The vertical axis symbolizes the position of the domain-wall. When v_g is decreased (this corresponds to moving to the right on the vertical axis) towards values close to v_{crit} , the position of the domain-wall diverges (bold curve). For $v_g = v_i$, the domain-wall turns unstable via the occurrence of a Hopf bifurcation. When v_g is decreased even further, various dynamical states occur (dotted curve). For $|v_i| < |v_g| < |v_{crit}|$, there is, according to the phase-space analysis, a stationary, but unstable domain-wall (dashed curve); for v_g beyond v_{crit} , there is no stationary domain-wall.

this renders the domain-wall state unstable, and we define v_i as the group-velocity for which this instability occurs (see figure 3-5).

We found that the primary instability indeed occurs when v_g has approached v_i within a few percent. The large patch of unstable single-mode state turns then convectively unstable, but the total domain-wall state is absolutely stable. This means that noise, which is mainly due to the discretization of space and time in the numerics, is amplified in the region where we have the unstable single-mode state. Due to the group-velocity, these fluctuations are advected towards the stable bimodal state (mode A) or the stable single-mode state (mode B), where they are dissipated.

To monitor where this instability occurs, we have followed the time evolution of the norm $\int dx A$ as a function of the group-velocity. When the instability of the domain-wall state occurs, the norm starts to oscillate with well-defined frequency. From this we conclude that the domain-wall turns unstable via a forward Hopf-bifurcation. However, the fact that in this case the system is still absolutely stable, yields that hidden line plots of the domain-wall hardly show a clear dynamic state. When v_g is close the v_i , one can observe the instability best in the norm $\int dx A$.

We have measured v_i for $s = 10$ and various values of Δg , and the results are listed

below.

$\Delta g = \gamma_{min} $	v_i	v_{crit}	v_i/v_{crit}
0.05	-0.43	-0.447	0.96
0.1	-0.62	-0.632	0.98
0.2	-0.87	-0.894	0.97
0.3	-1.06	-1.095	0.97

The error-bar on the measurements of v_i is of order 0.01. The most important conclusion that we can draw from this measurements is that v_i is very close to v_{crit} , and that this is independent of the value of γ .

Dynamical states.

In this section we investigate the fate of the domain-wall when v_g is decreased below v_i .

It is important to emphasize that, unlike many other transitions to dynamical behavior, there is, according to our phase-space analysis, no stationary albeit unstable state when $|v_g| > |v_{crit}|$. Thus, the single-mode and bimodal states are stable, each in its own domain, but there is no *stationary* domain-wall to connect these two asymptotic states.

We study again inhomogeneities of the form (3.3.12), and take the group-velocity 1.1, 1.2, 1.5 and 2 times the critical value v_{crit} . As initial conditions, we always took

$$A(x) = 0.85 + 0.15 \tanh((x - 0.15L)/10) \tanh((x + 0.25L)/10), \quad (3.3.13a)$$

$$B(x) = 0.35 - 0.35 \tanh((x - 0.15L)/10) \tanh((x + 0.25L)/10), \quad (3.3.13b)$$

which is close to the stationary state for $v_g = 0.9v_{crit}$.

Most of the dynamic states fall into two distinct types of behavior. For the weak inhomogeneities, the domain-wall moves irregularly back and forth around an average position. We will investigate whether this dynamics is chaotic. For stronger inhomogeneities, we often found that traveling kinks connecting states with the opposite signs of the amplitude B were generated in the bimodal regime.

We will describe in detail the dynamics that are found for the inhomogeneity with the steepness $s = 10$, which is the value of s that we will focus on; the other value of s will merely serve to explore the generality of the behavior found for $s = 10$.

At $\Delta g = 0.05$, we observe a disordered moving domain-wall, and this is also the case for $\Delta g = 0.1$. We will focus now on $v_g = 1.1v_{crit}$ and $\Delta g = 0.1$. The dynamics of the amplitudes A and B and the quantity $N := \int_{-\infty}^{+\infty} dx A / \langle \int_{-\infty}^{+\infty} dx A \rangle$ are shown in Figure 3-6. As is clearly seen in this figure, an essential dynamical degree of freedom is the position of the domain-wall that moves irregularly around a certain mean position. This mean position shifts to the right when v_g decreases. By extending the simulations to longer time intervals we have checked that the motion remains disordered.

To inspect whether the dynamics are chaotic, we have studied effects of small perturbations in the initial conditions. We have performed two runs, one (the unperturbed run) starting from initial conditions obtained as the final state of previous simulations in the disordered regime; for the perturbed run, the initial profile of $A(x)$ was unaltered, but

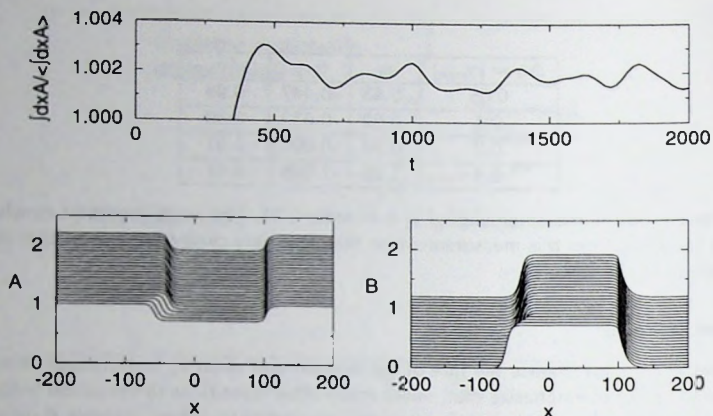


Figure 3-6. The upper panel shows the disordered fluctuations of $\int_{-\infty}^{+\infty} dx A / \langle \int_{-\infty}^{+\infty} dx A \rangle$, where the average is over the entire time of the simulation. The plots of A and B for this state are shown in the lower panels. Subsequent snapshots have a time difference of 80 and are shifted in the upward direction by a distance of 0.05. We used an inhomogeneity of the form (3.3.12) with $s = 10$ and $\Delta g = 0.1$, and set the group-velocity v_g to $1.1v_{crit}$. The left domain-wall at $x \approx -40$ is seen to fluctuate whereas the right domain-wall at $x \approx 110$ is completely stationary. The distance of the left domain-wall from the corresponding inhomogeneity in γ is 60.

the value of B at $x = 0$ was diminished by 10^{-5} . The data pertaining to the perturbed run will be distinguished by a prime. For the motion to be chaotic, we need to find an *exponential* divergence between A and A' for some time-interval. A close inspection of the dynamics for A and A' reveals that this is *not* the case; A and A' diverge but not exponentially. Therefore, we suspect the disordered motion of the domain-wall to be due to the convectively amplified discretization noise. This scenario is somewhat similar to the dynamics described in [57].

When the strength of the inhomogeneity is increased, a different type of behavior is observed. As an example, we will consider what happens at $\Delta g = 0.2$, although qualitatively the same behavior occurs at larger Δg . The motion that occurs at $v_g = 1.1v_{crit}$ is shown in Figure 3-7. A close inspection of the data reveals that, to the left of the domain-wall, where B is very small, zeroes of the function $B(x)$ are generated periodically. Each of them is then convected and amplified, leading to generation of a traveling kink. We have found that the frequency of the kink generation goes approximately linearly with v_g , and that it is nonzero at $v_g = v_i$. The velocity of the kinks is slightly smaller than the group-velocity. This can be understood as follows: associated with the kink in B is a small "bump" in A (see Figure 3-7). Without this bump, the kink would travel with precisely the group-velocity of B , but since the group-velocity of A is opposite to that of B , the

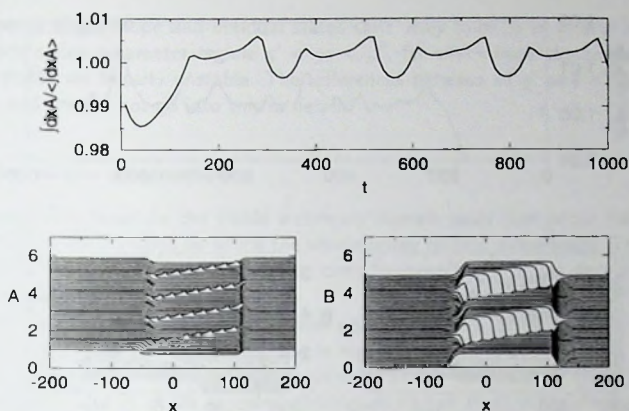


Figure 3-7. The upper panel shows the periodic fluctuations of $\langle \int_{-\infty}^{+\infty} dx A \rangle$. The plots of A and B for this periodic traveling kink state are shown in the lower panels. Consecutive snapshots have a time difference of 20 and are shifted in the upward direction by a distance of 0.1. We used an inhomogeneity of the form (3.3.12) with $s = 10$ and $\Delta g = 0.2$, and took the group-velocity $v_g = 1.2v_{crit}$.

small bump somewhat lowers the velocity of the kink.

Taking a smoother inhomogeneity ($s = 0.1$) suppresses the generation of kinks, and if they are still generated, this process is mixed with the irregular motion of the domain-wall, as is shown in Figure 3-8. The generation of kinks can even become irregular. Although there is no intimate connection, this propagation of kinks is reminiscent of the work described in [58].

In conclusion, when v_g is beyond v_i , the dynamical state may be represented by the disordered oscillating domain-wall, regularly generated and traveling kinks, or a mixture between disordered domain-walls and irregularly generated kinks.

3.4 The RGLE's with the group-velocity.

In this section we relax the condition that the order parameters A and B are real, and briefly study the behavior of a domain-wall in a system of two coupled RGLE's with the group-velocity terms:

$$\partial_t A + v_g \partial_x A = A + \partial_x^2 A - (|A|^2 + (1 + \gamma(x))|B|^2)A, \quad (3.4.1a)$$

$$\partial_t B - v_g \partial_x B = B + \partial_x^2 B - (|B|^2 + (1 + \gamma(x))|A|^2)B. \quad (3.4.1b)$$

The main question here is to see whether the results obtained for the NLDE's are relevant for the RGLE's.

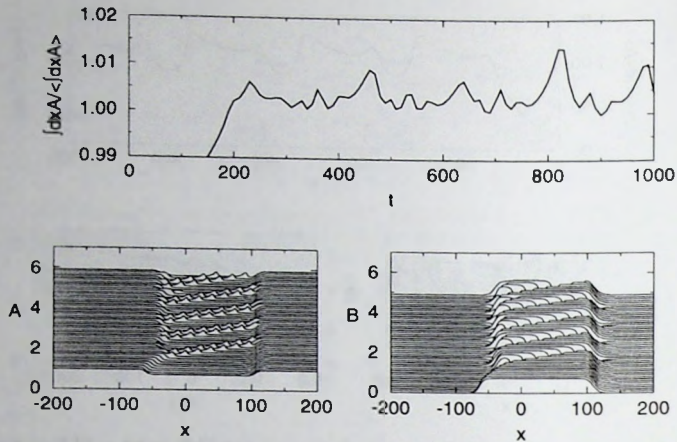


Figure 3-8. Mixture of a disordered oscillating domain-wall and traveling kinks in the NLDE's.

The complex order parameter leads to the question of the wavenumber selection, and the possibility of nonzero wavenumbers constitutes the main difference with the NLDE's. We have found that, for the stationary states, the wavenumbers often, but not always, relax to zero when the initial conditions have nonzero wavenumbers. When the wavenumbers of A and B are zero, the NLDE's can be used to describe the stationary states; when the wavenumbers are nonzero but constant, modified NLDE's describe the stationary domain-walls, as we will discuss below. In the dynamical regime, i.e., when $|v_y| > |v_x|$, small wavenumbers are generated starting from initial conditions with zero wavenumbers.

Note that the usual Eckhaus band of stable wavenumbers for a single RGLE [24] will be affected by the coupling between the two RGLE's. In particular, since for $\gamma \rightarrow 0$ both the single-modes and the bimodal states with zero wavenumber are only marginally stable, one may expect that the size of the band of stable wavenumbers is directly related to γ ; and that for $\gamma \rightarrow 0$ the band of stable wavenumbers closes. We have not pursued this question further.

On the other hand, the wavenumbers of A and B , which we refer to as q_A and q_B , also have an influence on the stability borders of the single and bimodal states. When $q_A = q_B$, the crossover between single and bimodal states occurs at $g_2 = 1$, just as when $q_A = q_B = 0$. This can be shown by substituting plane-wave solutions with equal wavenumbers in the RGLE's and performing a rescaling of x , t and the amplitudes, similar to the rescaling that is used to scale out the growth-rate ε (see equations (1.4.14) and (1.4.16)). Apart from this scale transformation, the equations for zero wavenumber and equal wavenumber are equivalent. When $q_A \neq q_B$, the stability borders for both the

homogeneous single-mode and bimodal states shift away from $g_2 = 1$, and in particular there exists a tiny parameter regime $g' < g_2 < g''$, for which both the single-mode and bimodal states are linearly unstable. The differences between of g' and g'' and 1 are of order q^2 , and we will not go into this in detail.

Relaxation of the wavenumber.

In this section we focus on the stable stationary domain-walls that occur for $|v_g| < |v_i|$ and explore the mechanisms by which the wavenumber relaxes numerically. The values of v_i that we found in the simulations are very close to those found in the simulations of the NLDE (we will come back to this below).

The simulations of equations (3.4.1) were performed for a periodic system of size 400. The inhomogeneity was of the form given in equation (3.3.12) with $s = 10$. The initial conditions were chosen to be like a domain-wall, similar to equation (3.3.13), but the wavenumbers q_A and q_B of the complex variables $A(x)$ and $B(x)$ in the initial states were allowed to be nonzero but constant, to study the wavenumber relaxation.

In the variational case ($v_g = 0$) the system (3.4.1) has a Lyapunov functional \mathcal{L} with a minimum at $q_A = q_B = 0$. Such states can not always be reached, since the periodic boundary conditions lead to conservation of the total phase difference across the system, as long as the amplitude remains nonzero. The wavenumber of, e.g., the mode $B(x)$ can be relaxed through the so-called phase-slips occurring at the points where $B = 0$ vanishes [25]. When B is not close to zero, generation of such a phase-slip may lead to a significant increase of \mathcal{L} , which is forbidden. It is then possible for the system to end up in a *local* instead of a *global* minimum of \mathcal{L} .

When $v_g \neq 0$, the system (3.4.1) is no longer variational, but for the stationary domain-walls the tendency to evolve to states with zero wavenumber is still present. We found that, the wavenumber of the B mode always relaxes to zero, while for the A mode, the wavenumber occasionally remains nonzero.

The B mode is approximately zero in the single-mode region of x . Phase slips can easily occur in this regime, and we have observed that q_B always relaxes to zero, both for $v_g = 0$ and $v_g \neq 0$. For $v_g = 0$, the local wavenumber diffuses, and for $v_g \neq 0$, the wavenumber is advected to the single-mode region, where it relaxes. When the initial q_B is large, the phase-slips of B occasionally occur in the double-mode region, but this is only a transient.

The A mode has nonzero amplitude in both the single-mode and bimodal region of x . Two different mechanisms for the relaxation of q_A are observed. In the simplest case, the phase slips occur close to the domain-wall, until q_A falls to a level ~ 0.1 . For long enough times, we find numerically that in this case q_A is independent of x . In some cases, the phase-slips lead to a single-mode state consisting of alternating patches with $A \approx 0$ and $B \approx 0$. In that case, both q_A and q_B relax to zero. We have found that, for fixed values of v_g , both mechanisms seem to occur, depending on the initial conditions; the non-variational effects that the group-velocity terms introduce, do not affect the tendency of the system to minimize the wavenumbers, at least for stationary states.

The stationary domain-walls of the coupled RGLE's are very similar to those of the NLDE's. When $q_A = q_B$, we can show this by substituting plane-waves of the form $A = |A| \exp(iqx)$ and $B = |B| \exp(iqx)$ into the RGLE's, which yields that the RGLE's are similar to the NLDE, up to the coefficient $(1 - q^2)$ in front of the linear term. By the aforementioned scaling we can scale this factors out, and this yields the NLDE's for $|A|$ and $|B|$. Therefore, when $q_A = q_B$, the stationary domain-walls produced by the RGLE's can be described by the NLDE's. The critical value of the group-velocity where the position of the domain-wall diverges is then also precisely given by the value of v_{crit} obtained for the NLDE's. The effect of nonzero wavenumber on v_i can in principle be more subtle, but in practice we could not find a difference between the values of v_i for the NLDE's and the RGLE's with $q_A = q_B$.

When $q_A \neq q_B$, we cannot scale out the wavenumbers. Substituting plane-waves of the form $A = |A| \exp(iq_A x)$ and $B = |B| \exp(iq_B x)$ into the RGLE's, yields two NLDE-like equations where the first terms of the right-hand side A and B are replaced by $(1 - q_A^2)A$ and $(1 - q_B^2)B$. Only one of these pre-factors can be scaled out, so the ordinary NLDE's (3.1.1) are not correct. However, since the difference of q_A and q_B that occurs in stationary domain-walls is of order 0.1 at most, and the effect on the RGLE's is of order q^2 , the NLDE's are still valuable to give a lowest order description of the ensuing domain-walls. In principle, one could carry out the geometrical analysis for the equations with the $(1 - q_A^2)A$ and $(1 - q_B^2)B$ terms; we will not give all the details here, but it can be shown that v_{crit} is perturbed by terms of order q^2 . This is consistent with the numerically observed increase of the value of v_i with q_A (when $q_B = 0$); this value increases at most a few percent when $q_A = 0.1$.

Dynamical states for $v_g > v_i$.

To investigate the dynamical states that occur when $v_g > v_i$, we used the same inhomogeneities and values of v_g as for the NLDE's. The same initial conditions were used, so we concentrate on initial states with zero initial wavenumbers. For a steepness $s = 10$, we have found, for almost all Δg and v_g beyond v_i , a disordered fluctuating domain-wall state. The mean position of the domain-wall shifts to the right with decreasing v_g ; this effect becomes weaker when Δg becomes larger. A slightly different state was observed for $\Delta g = 0.1$ and $v_g = 2v_{crit}$, when the oscillations of the domain-wall have a strong periodic component, but are nevertheless disordered; the reason for this is not clear. We found that when Δg is increased, the fluctuations of the position of the domain-wall decrease in general.

The phase of A remains zero in the dynamical state. The phase of B departs from zero, and B slowly develops wavenumbers ~ 0.01 . At longer times, these wavenumbers often remain constant in space and time. A clear exception is the aforementioned state with $\Delta g = 0.1$ and $v_g = 2v_{crit}$, where periodic modulations of the wavenumber persist.

For smoother inhomogeneities ($s=0.1$) and small Δg , the wavenumber generation is suppressed, and a traveling kink state is observed. This state is similar to the states produced by the NLDE's, in the sense that the phase difference across such a kink is π . However, the generation of kinks is now no longer periodic. When $\Delta g > 0.1$, these kinks

are not produced, and the local wavenumber is generated instead, just as in the case of the steeper inhomogeneity.

In conclusion, both the stationary states and the critical values of v_g for the RGLE's are almost the same as for the NLDE's, while the dynamical states are somewhat different. The main mechanisms that play a role for the domain-walls of the RGLE's can be described by the NLDE's.

3.5 The CGLE's.

In this section we will study the coupled CGLE's:

$$\begin{aligned} \partial_t A + v_g \partial_x A &= A + (1 + ic_1) \partial_x^2 A - \\ &\quad (1 - ic_3) |A|^2 A - g_2(x) (1 - ic_2) |B|^2 A, \end{aligned} \quad (3.5.1a)$$

$$\begin{aligned} \partial_t B - v_g \partial_x B &= B + (1 + ic_1) \partial_x^2 B - \\ &\quad (1 - ic_3) |B|^2 B - g_2(x) (1 - ic_2) |A|^2 B. \end{aligned} \quad (3.5.1b)$$

These are the generic amplitude equations for left- and right-traveling waves, and the group-velocity terms appear here naturally (see chapter 1). The nonlinear dispersion coefficients c_2 and c_3 are, in general, not equal, and we will find below that their difference will be a crucial parameter for the domain-walls. The behavior of a single CGLE is already incredibly rich [4], and the situation for the coupled CGLE's is of course not simpler. As a function of the coefficients c_i , typical states in homogeneous coupled CGLE's include single and bimodal phase-winding solutions, periodic solutions and spatio-temporal chaotic solutions [27, 59]. For fixed values of the coefficients, different states can coexist.

In the following we will restrict ourselves to describing some of the interesting states that occur in the numerical simulations of the coupled CGLE's.

The numerical simulations were carried out similarly to the RGLE's, in a periodic system of size 400. The inhomogeneity was of the form given in equation (3.3.12), and we focus on the case $s = 0.1$, although we have performed some runs with $s = 10$. It turns out that only the details of the dynamics are different for this larger value of s . We fix Δg which determines the strength of the inhomogeneity (3.3.12) at a value of 0.1.

As initial conditions we use, as before, the stationary state that is obtained when $v_g = c_1 = c_2 = c_3 = 0$. This means in particular that the critical value for g_2 is 1; it has been shown by Sakaguchi [59], that for periodic or disordered states the transition between single and bimodal behavior can occur for values different from 1.

Even with these restrictions, the parameter-space of the CGLE's is too large to warrant a complete overview of the dynamical behavior. The nonlinear dispersion is essential for the fate of the domain-wall, and to restrict the search in parameter-space, we restrict ourselves to three different cases: (A) $c_2 = c_3$, (B) $c_2 = -c_3$, (C) $c_2 = 0$. The role of the group-velocity and c_1 is discussed briefly for each case.

Below we will show that in many cases, the homogeneous single and bimodal states are invaded by periodic or chaotic states that nucleate from the initial domain-wall. A more systematic exploration is left for a further work.

3.5.1 The case $c_2 = c_3$.

When the nonlinear dispersion coefficients c_2 and c_3 are equal, the nonlinear term of equation (3.5 1a) (similar for (3.5 1b)) can be written as $(1 - ic_2)(|A|^2 + g(x)|B|^2)A$. Just as in the RGLE's, $(|A|^2 + g(x)|B|^2)$ differs only slightly from the value 1 for a domain-wall state, so the nonlinear dispersion acts similar to the linear dispersion. The main effect of the dispersion is then to shift the wavenumber of the B -mode, but apart from this, the behavior of the CGLE's is qualitatively similar to that of the coupled RGLE's.

When $q_B \neq 0$, $|B|$ is smaller than $|A|$ in the bimodal regime, and as a result, v_i is observed to increase (see the discussion on the effect of nonzero wavenumber on v_i for the RGLE's). For example, when $c_2 = c_3 = 0$ and $c_1 = \pm 1$, the selected wavenumber of B is close to 0.1, and $|B|$ is a few percent smaller than $|A|$. The critical value of the group-velocity is then increased by a few percent. When both c_1 and $c_2 = c_3$ are different from zero, the wavenumber of B can be large enough to shift the critical group-velocity substantially. For $c_1 = -1$ and $c_2 = c_3 = 0.5$, the wavenumber of B is close to 0.2, and the amplitude of B is approximately 20 percent smaller than that of A . The group-velocity v_i is then found to be between -0.84 and -0.85 . Although this is quite different from the case where the wavenumbers are zero, the essence of the transition to the dynamical domain-walls is still given by the analysis for the NLDE's. When the difference between c_2 and c_3 is small, we find qualitatively the same behavior as for $c_2 = c_3$.

3.5.2 The case $c_2 \neq c_3$.

The oscillatory behavior shown in Figure 3-9a and in more detail in Figure 3-10 arises from a feedback mechanism between local wavenumbers and amplitudes. When $c_2 \neq c_3$, gradients of $|A|$ and $|B|$ generate local wavenumber (see Figure 3-10b), and this local wavenumber suppresses, via the diffusive term, the amplitudes. As a result of this feedback mechanism, the domain-wall becomes oscillatory. When we take $c_2 = -c_3$ and $c + 1 = v_g = 0$, the frequency of the oscillations appears to be approximately linear in the strength of the nonlinear dispersion.

The strength of the aforementioned feedback mechanism grows with the nonlinear dispersion, and above a certain threshold, we find that the oscillations do not stay confined around the domain-wall, but spread out into the single-mode region. For instance, for $c_3 = -c_2 = 0.2$ we found that a periodic state is generated (Figure 3-9b), that is similar to the periodic state described recently by Sakaguchi [59]. The domain-wall itself becomes disordered. It should be noted that for these values of the coefficients, there are asymptotic single and bimodal phase-winding solutions that are linearly stable.

Finally, the nonlinear dispersion can become so large that also the bimodal state becomes periodic. The disorder seen in Figure 3-9c may be either a transient behavior or an established state; our simulations were not conclusive, and we leave this for further work. Here the coefficients of the CGLE's are such, that homogenous phase-winding solutions are unstable, and that even in homogeneous systems, i.e., for γ fixed at ± 0.1 , periodic states arise. The domain-wall here is disordered, and so this state shows the competition between linearly stable periodic states and a disordered domain-wall.

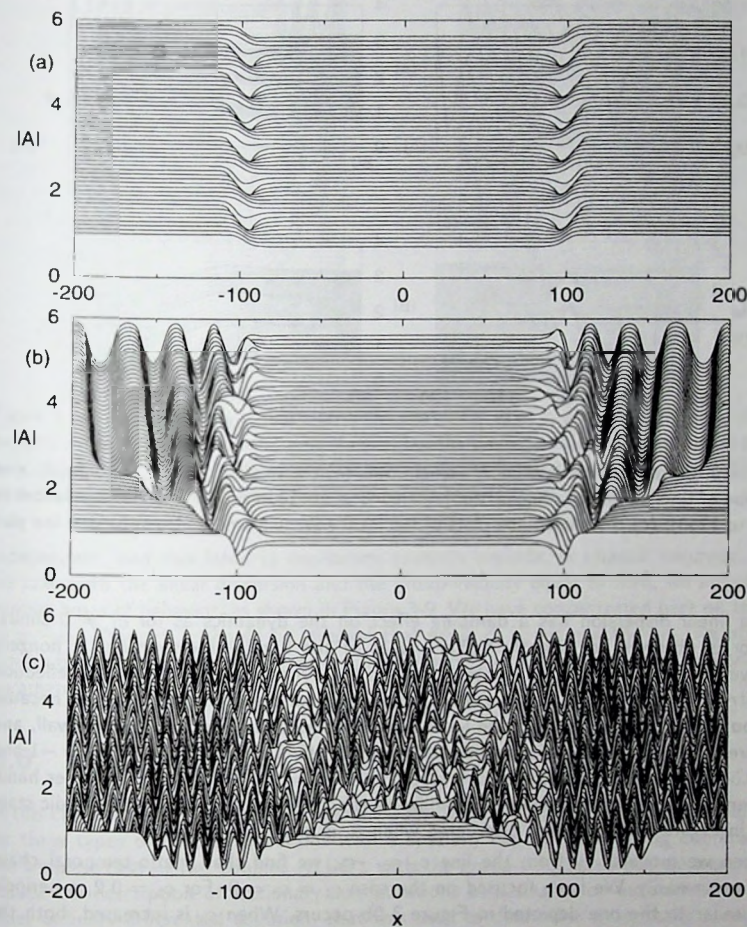


Figure 3-9. Three examples for the dynamics for $v_g = c_1 = 0$ and $c_2 = -c_3$, all for the time interval 2500. Separate sets have a time difference 50. (a): $c_3 = 0.02$, an oscillatory state; (b): $c_3 = 0.2$, the domain-wall becomes disordered and nucleates a periodic state, that becomes stationary at longer times; (c): $c_3 = 1$, the case when the bimodal state becomes unstable; it is not clear whether the system settles in a stationary periodic state or not.

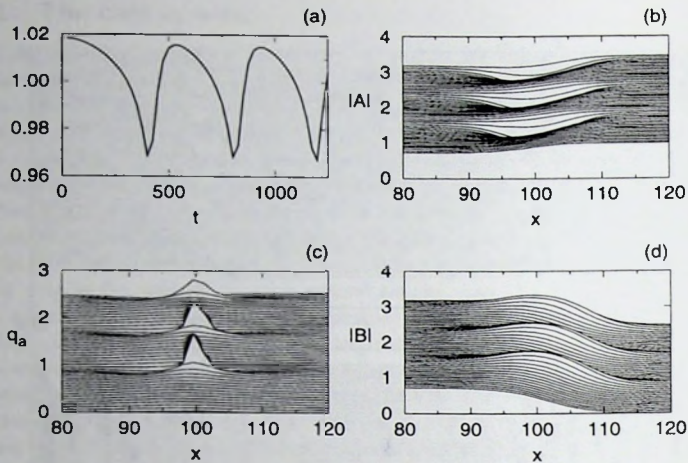


Figure 3-10. Close-up of the oscillatory domain-wall: (a) the value of $\int dx|A| / \langle \int dx|A| \rangle$ as a function of time; (b) hidden-line plot of $|A|$ around $x = -100$ for the first three oscillations (t from 0 to 1250); (c) the hidden-line plots of the local wavenumbers of A ; (d) hidden line plot of $|B|$.

The linear dispersion has a damping effect on the dynamics as for $c_1 \neq 0$ similar behavior is observed for slightly higher values of the nonlinear dispersion. A nonzero group-velocity has a more complicated effect on the dynamics, as it breaks the reflection symmetry. The oscillations that occur for small nonlinear dispersion are damped, because the group-velocity terms advect the local wavenumbers away from the domain-wall, and therefore they suppress the aforementioned feedback effect. For instance, for $c_1 = -1$ and $v_g = 0.5$, we have observed stationary states up to $c_3 = -c_2 = 0.1$. On the other hand, the symmetry breaking can have a destabilizing effect on the dynamics: the periodic state shown in Figure 3-9b becomes disordered when v_g is nonzero.

When we move away from the line $c_2 = -c_3$, we find that spatio-temporal chaos occurs quite easily. We have focused on the case $c_1 = c_2 = 0$. For $c_3 = 0.2$, a periodic state similar to the one depicted in Figure 3-9b occurs. When c_3 is increased, both the periodic and the bimodal states become gradually disordered (Figure 3-11a and 3-11b).

When $v_g = 0$, the chaotic state consists of more or less stationary, irregularly growing and decaying pulses, but when $v_g \neq 0$, this quasi-stationary character is destroyed. We have checked that in the disordered regime, two slightly different initial conditions diverge throughout the whole domain, which indicates that these states are an example of spatio-temporal chaos.

When c_2 is sufficiently different from c_3 , the nonlinear dispersion is no longer spatially

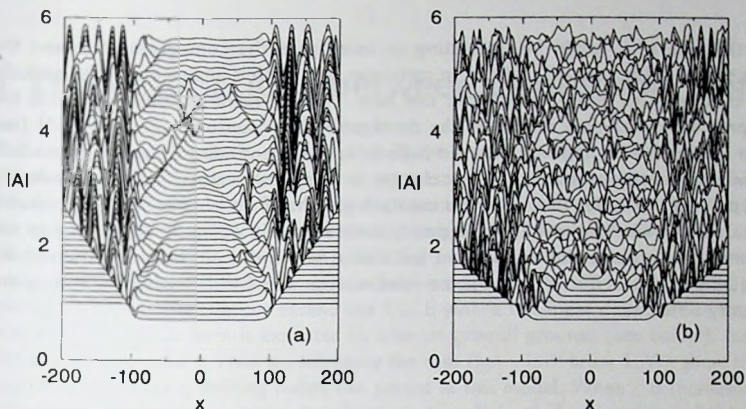


Figure 3-11. Two examples of spatio-temporal chaos, for $v_g = c_1 = c_2 = 0$: (a) $c_3 = 0.5$, the periodic single-mode state has become chaotic, but the single-mode state seems rather passive, only disturbed by ingoing perturbations generated by the fluctuating domain-wall; (b) $c_3 = 1$, both the single and bimodal state have become spatio-temporally chaotic.

independent, and this leads to oscillatory, spatially periodic or chaotic behavior. When we take both the linear dispersion and the group-velocity equal to zero, we already find various types of behavior, as shown in Figure 3-9. We have concentrated here on the case $c_2 = -c_3$, although it should be stressed that when c_2 is not exactly $-c_3$, we observed similar behavior. The choice $c_2 = -c_3$ merely serves to limit ourselves in exploring the parameter-space.

3.6 Conclusion and outlook.

In this chapter we have considered domain-walls between single-mode and bimodal states for three types of coupled equations with a spatially dependent coupling coefficient. In the simplest case of two coupled NLDE's with the group-velocity terms, we were able to reduce the description of stationary configurations to a single non-autonomous second-order ordinary differential equation, that was used to determine analytically a necessary condition for the existence of a stationary domain-wall in terms of the group-velocity. We have found that our prediction for the destabilization of such a stationary domain-wall is in good agreement with numerical simulations, and we have found a disordered oscillating domain-walls in the case when the group-velocity is beyond the corresponding threshold. For two coupled RGLE's we have found a similar scenario. Finally, for the coupled CGLE's, we have found that, the stationary domain-walls are unstable, even when the group-velocity is zero, and spatio-temporal disordered states often occur in this

model.

In the future, it would be interesting to investigate the competition between the various states of the coupled CGLE's. In particular, not much is known about the periodic states that seem to play an important role here. Possible research subjects include the development of analytical solutions, the development of counting arguments [11] (see chapter 1) and the competition between periodic and phase-winding solutions. The effect of an inhomogeneity as studied in this chapter on the various states may be a valuable tool in probing the states that occur for constant g_2 . The effect of nonzero group-velocity on the domain-walls in the CGLE's is poorly understood; it would be interesting to see whether the divergence and subsequent instability of the domain-wall, as observed for the NLDE's and CGLE's, still has some relevance for the CGLE's when c_2 and c_3 are sufficiently different.

4 The interactions between pulses and fronts.

The work in this chapter has grown out of the desire to verify a conjecture on the apparent stability of pulses that drift in an unstable ($\varepsilon > 0$) background state [60]. This phenomenon occurs in binary liquid convection, which we briefly describe below. The quintic CGLE (1.4.22) is often used to model this system, and we will discuss the essential properties of the fronts and pulses that occur as solutions to this equation. The pulses in binary liquid convection drift with a velocity that is different from the group-velocity, and to model this, we extend the CGLE with a nonlinear derivative term of the form $s\partial_x A|A|^2$. Such term is expected to arise on general grounds (see below), but only with a small pre-factor s . Here we will study the case that s is of order 1. We show that for positive growth-rate ε , drifting pulses can persist in this model. When ε is increased, two different destabilization scenarios are observed. In sufficiently large systems, fluctuations grow out to form multiple pulses. In small systems, an increase in ε eventually leads to a competition between fronts and pulses that results in a sharp transition to a state where the drifting pulse leaps forward in an incoherent fashion. Finally, we discuss the possibility of similar behavior in other systems.

4.1 Convection in binary liquids.

If one uses instead of a pure fluid a mixture of two fluids in the convection experiment, new phenomena appear. The important new feature is that apart from a concentration flow induced by ordinary diffusion, temperature differences also induce a concentration flow. The hydrodynamic equations (1.2.3a) - (1.2.3c) have to be supplemented by equations for the concentration c of one of the components:

$$\partial_t c = -\vec{\nabla} \cdot \vec{J}_c, \quad (4.1.1a)$$

$$\vec{J}_c = -D_c(\vec{\nabla}c + \psi\vec{\nabla}T) + c\vec{u}, \quad (4.1.1b)$$

where D_c is the diffusion coefficient of the component in question. The coupling between temperature and concentration flow is known as the Soret effect and the dimensionless coefficient which measures the strength of this effect, ψ , is called the separation ratio; ψ can be both positive and negative, depending on the average concentration of the mixture. One can imagine that this effect is important in convection; if the sign of ψ is such that the heavier fluid component flows to relatively hotter regions it has a stabilizing effect, whereas if the heavier component flows to colder regions it has a destabilizing effect. Another possible coupling between concentration and temperature is known as the Dufour effect and this is the coupling between concentration gradient and the heat current. For convection of binary liquids this effect can be neglected [4].

Since the dynamics of the concentration is in general on a different time scale than the dynamics of fluid-motion, the resulting behavior can be quite rich. The ratio of time

scales is given by the Lewis number D_c/κ which is typically very small (10^{-2}) for liquids. The important point is that for negative separation ratios, the onset of convection occurs via a Hopf bifurcation, so the roll pattern is time dependent, and consists of traveling waves.

This system is historically one of the first realizations of the CGLE, and therefore Rayleigh-Bénard convection in binary fluids has been the object of intense study in the last few years. There are two major problems, however, with the amplitude approach for this system. Due to the smallness of the Lewis number it turns out that an amplitude expansion can only be valid for very small amplitudes of the pattern [4]. Moreover, the bifurcation turns out to be subcritical (g_0 is negative), so small amplitudes are quite exceptional and in general a perturbative approach is not valid. On the other hand, the subcritical bifurcation gives rise to rich behavior, and we will outline some of the interesting features of both binary liquid convection and the quintic CGLE below.

4.2 Pulses.

A few years ago, localized or confined traveling wave states were discovered in convection experiments in binary liquids [60, 39, 61, 62, 63, 64, 65]. These are states of which the region where the convection occurs does not fill the total experimental cell, but instead attains a well-defined width. The discovery of these states has inspired a considerable amount of theoretical work on pulse solutions of amplitude equations [4, 11, 35, 22, 66, 67]. It is by now well established that in experiments in annular geometries, a localized traveling wave state drifts slowly when the inhomogeneities of the convection cell are sufficiently small [62]. This drift velocity v_p is quite different from the group-velocity v_{gr} and this can be contributed to a slow concentration field [35, 67] that "traps" the pulse in its own concentration gradient. The existence of localized states and much of their behavior can be understood in terms of pulse-shaped solutions of a complex Ginzburg-Landau amplitude equation [11, 66]. The fact that the pulse velocity v_p differs so much from v_{gr} can, however, only be obtained from a more detailed analysis of the coupling of the convection to the slow concentration field [35, 67].

We will now describe the main results for the existence of pulses (see figure 1-6) in the quintic CGLE (1.4.22). Perturbation expansions about both the relaxational limit ($c_i \rightarrow 0$) and the Hamiltonian limit ($c_i \rightarrow \infty$) [11] have shown that there exist stable pulse solutions which move with the group-velocity in large subcritical ($\varepsilon < 0$) ranges of the $\varepsilon, c_1, c_3, c_5$ parameter space. A counting argument [11] shows that the pulses come in discrete sets, in contrast to for instance plane-waves, that come in continuous families.

Pulse solutions of the quintic CGLE propagate with the group-velocity of the traveling waves; in principle, if one considers an amplitude expansion near a weakly subcritical bifurcation (meaning that the pre-factor of the real part of the destabilizing cubic term is small), nonlinear gradient terms of the form $\partial_x A |A|^2$ and $\partial_x |A|^2 A$ will arise. In fact, these terms are of lower order in ε than the quintic term $|A|^4 A$, and they lead to a drift velocity of the pulses that is slightly different from the group-velocity. Experimentally, however, pulses are found to have a drift velocity much smaller than the group-velocity

[62]. This can be accounted for on an ad-hoc basis by adjusting the coefficients of the nonlinear gradient terms to be large. Although recent work [35, 64] demonstrates that ensuing single amplitude equation can not account for all phenomena observed in the experiments, the essential difference in v_{gr} and v_p and the periodic boundary conditions are captured in this model. We will follow the model equation approach and study the simplest extension of the standard quintic CGLE that has a difference between group-velocity and pulse velocity. Since this is only a model, we will only include one of the possible nonlinear derivative terms. The model that we study is

$$\partial_t A = \varepsilon A + (1 + ic_1)\partial_x^2 A + (1 + ic_3)A|A|^2 - (1 - ic_5)A|A|^4 + s(\partial_x A)|A|^2. \quad (4.2.1)$$

and is sometimes referred to as the quintic derivative Ginzburg-Landau equation [4, 11]. Note that we have written this equation in the frame of the group-velocity of linear waves; the nonlinear gradient term $s(\partial_x A)|A|^2$ breaks left-right symmetry and causes pulses to drift. We fix the parameters $c_1 = 1.4$, $c_3 = -1$ and $c_5 = -1$ since pulses are stable then (See section 4.2 of [11]), and fix $s = -1$. For these parameters, a pulse drifts to the right and its velocity is measured to be $v_p \approx 1.5 \varepsilon + 0.373$ for small ε .

A more fundamental analysis by Riecke [35] attributes the small drift velocity of pulses to the coupling of the amplitude A to the slow concentration field. This represents a correction to the amplitude expansion due to the existence of an extra slow variable. This model, which we will study briefly at the end of this chapter, is

$$\partial_t A = \varepsilon A + (1 + ic_1)\partial_x^2 A + (1 + ic_3)|A|^2 A - (1 - ic_5)|A|^4 A + fCA, \quad (4.2.2a)$$

$$\partial_t C = v_g \partial_x C + a_c C + d_c \partial_x^2 C + h \partial_x |A|^2. \quad (4.2.2b)$$

C is the real valued concentration field. The disadvantage of such model is its large number of adjustable parameters, which makes in particular numerical exploration quite a task, since the coefficients corresponding to the concentration field are not known.

4.3 Fronts.

The subject of front-propagation is one of the classics in the theory of pattern formation [28, 29]. It deals with the following elementary question. Suppose that we study a spatially extended system near a bifurcation, such as the CGLE around $\varepsilon = 0$. We now want to describe the dynamical process by which the $A = 0$ state evolves to a nonlinear state when ε is increased from a negative to a positive value. Intuitively, it is clear that after such an increase of ε , fluctuations of the $A = 0$ state will grow, initially with a growth-rate determined by ε . Gradually the nonlinearities will start to play a role, saturating the growth, and so the fluctuations grow out to a patch of nonlinear state (for instance a traveling wave) in a background of unstable $A = 0$ state. The crossover region between the nonlinear state and the unstable linear state is called a front. Suppose for definiteness, that we have $A \rightarrow 0$ to the right of the front, and the nonlinear state to the left. One may expect that to the far right of the front, $|A|$ decays exponentially. This exponential

"leading edge" will grow according to the linearized equation, and consequently, the front appears to propagate to the right. The nonlinear state invades the unstable linear state. One can easily see, that different spatial decay-rates of the front (k^\dagger , see below) give rise to different velocities of the front. It turns out, however, that for sufficiently localized initial conditions only one front velocity is selected. The question that plays the central role in the theory of front propagation is to determine this velocity.

For general equations, there is no algorithm yet to determine what the selected front velocity will be. There is, in particular around a supercritical bifurcation, a good candidate, and that is the linear marginal stability (LMS) velocity, denoted by v^* . This velocity can be calculated simply from the dispersion relation as follows. Write the exponential profile of the front as $\exp(-i\omega t + ikx)$, where both ω and k may be complex. If we denote their real and imaginary parts by superscripts r and i respectively, the LMS velocity is given by the equations [28, 29]

$$v^* = \frac{\omega^i}{k^i} = \frac{\partial \omega^i}{\partial k^i}, \quad \frac{\partial \omega^r}{\partial k^r} = 0. \quad (4.3.1)$$

The usual statement is now that this velocity is selected (for sufficiently localized initial conditions), unless there exists a particular nonlinear front solution [29], with a faster velocity v^\dagger and larger decay-rate κ than the LMS front. There are many examples known where the LMS framework gives the exact and correct velocity, but also examples where the selected front velocity is larger than v^* are well documented [29, 68]. In particular, in the vicinity of a subcritical bifurcation, the nonlinear front often plays a role. In general, it is not known under what conditions v^* is the selected velocity. The LMS velocity v^* is believed to be an exact lower bound [11].

However, the dynamics of fronts in the CGLE is relatively well understood and front propagation has been studied in great detail [11] for the quintic equation (1.4.22) for both $\varepsilon > 0$ and $\varepsilon < 0$. It turns out that an exact nonlinear front solution can be found, whose dynamics plays an important role in the selection of patterns.

Together with a set of rules and conjectures a picture of the stability of pulses and of the dynamics of fronts has been emerged. The three structures that these rules focus on are pulses and LMS and nonlinear fronts. The framework can be discussed most easily by fixing the c_i 's in the CGLE, and discussing the various types of behavior when ε is increased.

- For sufficiently negative ε , both pulses and fronts decay back to the stable $A = 0$ state.
- For $\varepsilon_2 < \varepsilon < \varepsilon_3 \leq 0$ pulses are the selected solutions. The lower bound on ε , ε_2 , can not be determined analytically, but the upper bound, ε_3 is obtained by the condition that $v^\dagger(\varepsilon_3) = 0$. It should be noted that ε_3 is never positive, although it can be zero for certain regions in the parameter-space of the CGLE.
- For $\varepsilon > \varepsilon_3$, fronts are the selected solutions. Suppose that the c_i 's are such that a nonlinear front exists, and denote the value of ε where $v^* = v^\dagger$ by ε^\dagger . The nonlinear

front is then selected for $\varepsilon_3 < \varepsilon < \varepsilon^\dagger$, and the LMS front is selected for $\varepsilon > \varepsilon^\dagger$. Note that, since LMS fronts only propagate for positive values of ε , ε^\dagger is never negative.

So, according to these rules, pulse solutions become unstable by splitting into two fronts which move apart when $\varepsilon > \varepsilon_3$. The long time properties of each front are then given by that of a single front.

This framework is developed for the CGLE without nonlinear derivative terms, i.e., for pulses that move with the group-velocity. As we have indicated in the discussion on pulses, this is not true in the experiments in binary liquid convection. Therefore we will study below the effect of a pulse velocity different from the group-velocity on the interaction of pulses and fronts. Since the experiments we are interested in were carried out in an annular geometry, we will use periodic boundary conditions.

4.4 Coherent and incoherent drifting pulse dynamics.

In the experiments in an annular geometry [60, 61, 64], the localized traveling wave states surprisingly persist in a regime where the conducting state ($A = 0$) is unstable ($\varepsilon > 0$). This persistence of pulses in an unstable background is usually explained as follows. Since an annular cell is periodic and since the pulse drifts with a velocity v_p different from the velocity v_{gr} with which the fluctuations propagate, the maximum time interval during which a fluctuation can grow before interacting with the pulse is finite and of order $L/|v_{gr} - v_p|$, where L is the circumference of the cell. Glazier and Kolodner [63] observed that small wave packets that collide with a pulse are annihilated, so it is conceivable [60] that when the growth-rate ε is sufficiently small, fluctuations in a finite cell do not grow strong enough to destroy the pulse state: it is as if the moving pulse sweeps the system clean.

Most theoretical work on pulses is based on perturbation expansions around integrable limits of Ginzburg-Landau amplitude equations and assumes an infinite domain [11, 66]. Such an analysis is insensitive to the instability of the background state that occurs when $\varepsilon > 0$; this instability is usually implemented ad hoc by simply assuming that a pulse can not persist for positive ε .

Below, we want to go beyond such an ad hoc approach, and study the pulse dynamics when $\varepsilon > 0$ in some detail for the model amplitude equation 4.2.1 that captures the two main experimental ingredients, i.e., periodic boundary conditions and the difference between v_p and v_{gr} . Our findings can be summarized in the phase-diagram of Figure 4-1, which labels the various types of asymptotic states that arise as a function of the system size L and ε , when the initial state is a single pulse. Our main interest will be the sharp transition from single coherent pulse motion in regime I to incoherent pulse motion in regime III, which we show to be the result of a competition between pulse and front propagation.

We use a pseudo-spectral method to numerically solve the amplitude equation (4.2.1) with periodic boundary conditions, with a time step of 0.05 and 256 Fourier modes. The

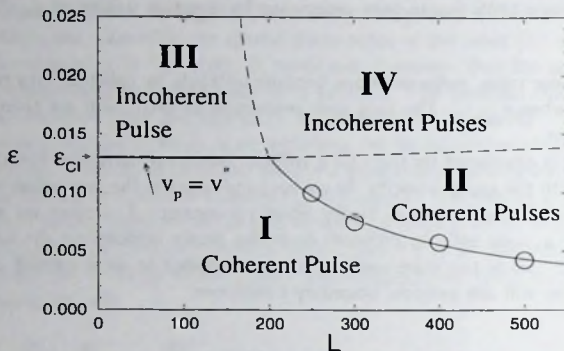


Figure 4-1. Tentative phase-diagram showing the various states that arise as a function of ε and L . In regime I and III there are single pulses, that either propagate coherently (I) or incoherently (III). Multiple-pulse states are observed in regimes II (coherent) and IV (incoherent). The thin full line marks the transition between these two regimes, and is given by $\varepsilon(L - 50) = \text{const.}$; the open dots indicate some of the numerical measurements of this transition. The CI-transition between the single coherent and incoherent pulses is denoted by a fat line; it occurs at a value ε_{CI} given by equation (4.4.1). The exact location of the transitions between regimes III and IV and between regimes II and IV, indicated by dashed lines, has not been determined.

main role of fluctuations is to excite the modes that grow from the linearly unstable state $A = 0$. We will not systematically study the effect of an additive noise-term, which would amount to getting an extra parameter in the phase-diagram, since the discretization noise alone is sufficient to excite the unstable modes, but we have checked that neither the inclusion of a stochastic noise term in the amplitude equation (4.2.1) nor a change in the number of modes qualitatively alters our conclusions. The phase-slips that occur even for $\varepsilon < \varepsilon_{CI}$ in a finite system in the region where front and back side of the pulse merge, appear to be another source of fluctuations. We will proceed by describing the various states that are listed in the phase-diagram.

Regime I corresponds to the scenario sketched earlier: the drifting pulse annihilates the fluctuations, and the system behaves the same as for $\varepsilon < 0$; this state is the analogue of the pulses that persist in the experiments for $\varepsilon > 0$. The norm $\mathcal{N} := \int dx |A|$ converges to a value close to the norm of a single pulse in the $\varepsilon < 0$ regime.

In regime II the fluctuations grow out to form new pulses before they can be absorbed by the initial pulse. If L and ε are not too deep into regime II, the system ends up in a state with two pulses. The maximum time interval during which fluctuations can grow without meeting a pulse is then reduced, and therefore the double-pulse state can be stable. The norm converges then to a constant that is approximately twice as big as

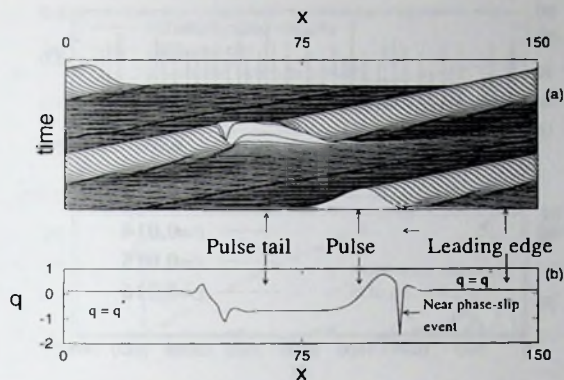


Figure 4-2. (a) Space-time plot of $|A|$ of a forward leap event that occurred for $\varepsilon = 0.018$ in a system of size 150. Time increases upwards, and every curve in this hidden line plot is separated by a time interval of 5; the whole picture occurs over a time interval of 500. The fat curve marks the position in the leading edge of the LMS front where $|A| = 0.01$, and propagates with v^* . (b) A plot of the local wave-vector q of A for the initial state of the hidden line plot.

it is for a single pulse state. When L and ε are further increased, states consisting of more pulses are formed, that were observed to persist in some cases. Similar behavior was observed by Kolodner [60]. Since the fluctuations grow as $e^{\varepsilon t}$, their maximum strength is roughly determined by the growth-rate and the maximum time for which they can grow; in a single-pulse state this time is roughly $(L - W)/|v_g - v_p|$, where W is a measure for the width of the pulse which is of order 50 for our choice of parameters. The transition to multiple pulses seems to occur when the fluctuations grow above a certain critical strength, and since v_p depends only weakly on ε , the transition curve is expected to be given approximately by $(L - W) \sim 1/\varepsilon$ [60], which is the dashed line in Figure 4-1. This is in reasonable agreement with our numerics. The inclusion of an additive noise source shifts the transition curve to lower values of L and ε , as one would expect, but there remains a region where the single coherent pulse persists.

The surprise occurs when we cross the border between coherent and incoherent behavior (CI) and enter region III; the motion of the pulse then becomes an irregular mixture of coherent drift and forward leaps. Peaks of the norm as shown in Figure 4-3a (which we will refer to as "spikes") correspond to a forward leap of the pulse like the one shown in Figure 4-2a. The average time interval $\langle \Delta t \rangle$ between subsequent spikes strongly depends on the distance from the CI-transition. This transition can be understood when a connection with the theory of front propagation is made.

For the parameters that we have chosen, there are no nonlinear front solutions that can overtake the LMS fronts [11], so fronts propagate with the LMS velocity v^* . For

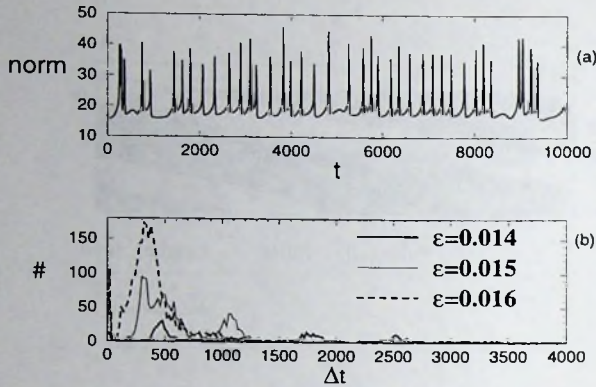


Figure 4-3. (a) Typical plot in regime III of the norm \mathcal{N} as a function of time for $\epsilon = 0.018$ and $L = 150$. (b) Histogram showing the distribution of the time intervals between two spikes, Δt , for $\epsilon = 0.014, 0.015$ and 0.016 . The system size is 160, and the total duration of each run 10^6 . We have defined the spike to occur when the norm passes through a value of 20 from below, and used a bin of 20 on the time axis.

the amplitude equation (4.2.1) the LMS velocity is given by $v^* = 2 \sqrt{\epsilon(1 + c_1^2)}$ (see equation (4.3.1)), and q^* , the local wavenumber in the leading edge of the front, is given by $c_1 \sqrt{\epsilon/(1 + c_1^2)}$ [11, 28, 29]. For our choice of c_1 , c_3 and c_5 , the nonlinear state behind a front is disordered (similar to Figure 20 of [11]).

When v^* is comparable to the pulse velocity, pulse and front propagation strongly compete, and indeed within our numerical error we find that the CI transition occurs *exactly* at an L -independent value ϵ_{CI} where the front and pulse velocity coincide,

$$v_p(\epsilon_{CI}) = v^*(\epsilon_{CI}). \quad (4.4.1)$$

For our parameters, this gives $\epsilon_{CI} \simeq 0.0130$.

We will now describe our understanding of this result and our evidence supporting our view that this marks the exact CI transition. Consider again Figure 4-2, where we show a space-time plot of $|A|$ to illustrate the dynamics of the single pulse in the incoherent regime III, together with a plot of the local wavenumber q in the initial state of the space-time plot. After a transient time the fluctuations organize themselves into the structure labeled "leading edge" that propagates ahead of the pulse. Note that "trailing" and "leading" edge refers to the behavior in the frame moving with the group-velocity, not to the experimental lab frame.

The local wavenumber of this structure is seen from Figure 4-2b to be close to the theoretical prediction for q^* , which for $\epsilon = 0.018$ yields $q^* \simeq 0.11$. This fact, together with the fact that this structure only builds up when $v^* > v_p$, shows that this structure is the

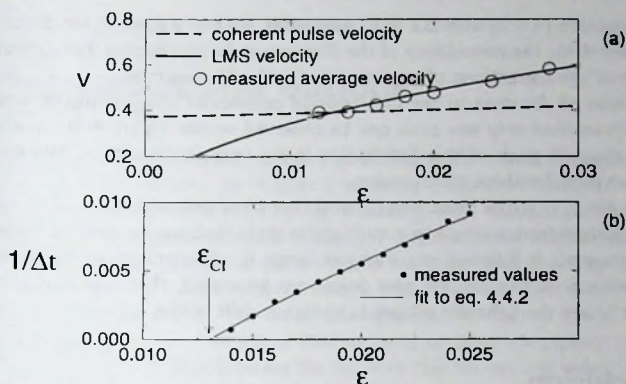


Figure 4-4. (a) The LMS velocity v^* (full line), the coherent pulse velocity v_p (dashed line), and the measured average pulse velocity $\langle v \rangle$ (circles). (b) The average time between two subsequent spikes is seen to diverge as ϵ approaches ϵ_{CI} .

leading edge of an LMS front. The evolution of this front is illustrated in Figure 4-2a by the fat line, which marks the point where $|A| = 0.01$; this point propagates with velocity v^* , and as close inspection of the plot shows, it outruns the pulse: $v^* > v_p$. After a certain time interval the rear of the LMS front grows out to a nonlinear structure that merges with the pulse. Effectively, the pulse temporarily broadens (leading to a spike in the norm N) and then leaps forward to absorb the rear of the LMS structure, while leaving most of the leading edge intact (as evidenced by the absence of appreciable perturbations of the fat line). Then this whole process repeats itself, so that viewed on a long time scale, the motion of the pulse can be characterized as a mixture of coherent drift and incoherent forward leaps.

The oscillations that are visible where the right side of the pulse matches onto the LMS front, are caused by phase-slips that occur because there is a mismatch between the frequency and wavenumber of the pulse profile and the LMS front. At the initial time shown in the lower panel, such a phase-slip event had just occurred. By monitoring singularities in the local wavenumber, such phase-slips can also be observed in the region where the back side of the pulse connects to the leading edge of the LMS front.

A forward leap of the pulse does not seem to affect the leading edge of the LMS front, and so when we are not too deep into the incoherent regime III, the leaps serve to keep the average pulse velocity $\langle v \rangle$ in pace with the front: $\langle v \rangle = v^* \langle \partial \epsilon / \partial t \rangle$ — see Figure 4-4a. When we denote the distance of a forward leap by Δx , then $v^* = \langle v \rangle = v_p + \langle \Delta x / \Delta t \rangle$. If we assume that Δx is a constant we then obtain

$$1 / \langle \Delta t \rangle = (v^* - v_p) / \Delta x. \quad (4.4.2)$$

When we use the aforementioned expressions for v_p and v^* and fit our data points for

$1 / \langle \Delta t \rangle$ to equation (4.4.2) with Δx as fit parameter, we find a good fit for $\Delta x \simeq 14.8$ as shown in Figure 4-4b; the consistency of the divergence Δt as ε approaches ε_c provides further evidence of the correctness of our scenario for the CI transition.

The distribution of Δt close to the CI-transition consists of multiple peaks, whereas far from the CI-transition only one peak can be observed — see Figure 4-3b; moreover, the location of the first peak of this distribution is not very sensitive to ε . We have at present no explanation for these observations.

It should be noted that the leaps also occur as transient behavior when $v^* < v_p$. For instance, the evolution from a single to a multi-pulse state that can be observed when an initial single pulse state is followed in parameter range II, often starts out by the single pulse leaping forward. In this process new pulses are generated, that also may perform some leaps, but finally the behavior relaxes to coherent drift in this regime.

4.5 Conclusion.

The competition between pulses and fronts in our model leads to complicated behavior. Behavior similar to the oscillations of the leading edge of the pulse has been observed in experiments by Glazier and Kolodner [63], and is very briefly mentioned by Riecke [35]. The oscillations of the leading edge of the pulse are also similar in appearance to the oscillations of pulses that were observed by Deissler and Brand [69] in the quintic complex Ginzburg-Landau equation. We have conducted numerical simulations that show that oscillation pulses, similar to those of Deissler and Brand, seem to occur when the nonlinear marginal stability velocity [29] is close to zero! This hints that the interaction between a *nonlinear* front and a pulse may lead to these oscillating pulses, and that the oscillations they observe are, in that sense, connected with the phase-slips we observe. So the rule that pulses become unstable when v^\dagger becomes positive, needs refinement.

Since the two ingredients of our scenario, i.e. the existence of pulses and the linear marginal stability mechanism, are robust, we expect the CI-transition to be rather general. In order to verify this, we have briefly studied the aforementioned model (4.2.1) proposed by Riecke [35] to describe pulses in binary fluid mixtures. We have taken the c 's as before and take $f = -0.3$, $a_c = -0.02$, $d_c = 0.1$ and $h_2 = -0.2$. Regimes I, II and IV can easily be verified to exist. We have found that for $v = 0$ and $v = 0.1$ the CI-transition occurs at values of ε given by equation (4.4.1), and that the average speed adjusts to v^* . However, for increasing v , Δx decreases so that regime III shrinks; when $v \gtrsim 0.3$, ε_{CI} becomes so large that the pulse destabilizes via a different mechanism. This illustrates that the CI-transition is not restricted to Eq. (4.2.1), although the detailed dynamics in the incoherent regime may depend on the model. The fact that the amplitude and wavenumber structure observed numerically is very reminiscent of that seen experimentally, is another indication of the robustness of our scenario.

Conclusion and outlook

In this thesis, we have used various approaches to the amplitude equations to understand nonequilibrium patterns. In chapter 2 we apply established methods to obtain the amplitude equations for a rotating Rayleigh-Bénard system. Our calculations for the coefficients of the amplitude equations predict that this system can be used to study spatio-temporal chaos in a controlled experiment. In chapter 3, on the other hand, the amplitude equations are used as a toy model to study certain aspects of the dynamics of spatially extended nonequilibrium systems. The amplitude equations in chapter 4 are, in a sense, between these two approaches; the model that we focus on does not capture all of the experimental features, but it does describe the features that we are interested in. We would like to conclude by sketching prospects for further studies.

In chapter 2 we calculated, for a rotating Rayleigh-Bénard system, the coefficients of two coupled complex Ginzburg-Landau equations, starting from the fluid equations. These calculations, although tedious, are simpler than the calculations that are carried out in many other branches of physics; yet they have only been performed for a very small number of physical systems. In particular for patterns consisting of traveling waves that are described by complex Ginzburg-Landau equations, the behavior depends completely on the coefficients of the amplitude equations, so there is an obvious need for more calculations of these coefficients. Although the amplitude equations have proven to be a valuable tool in the understanding of many nonequilibrium patterns [4], a real theory of patterns should not rely on adjustable parameters that are known only in principle. Moreover, once the precise form of the amplitude equations for a certain experimental system have been calculated, the comparison between theory and experiment can be made more precise. We expect that, in analogy with the convection experiments in binary liquids, discrepancies between theory and experiment will occur, and understanding these can lead to a new insights.

In chapter 3 we have studied the spatial juxtaposition of single and bimodal states in inhomogeneous, coupled amplitude equations. During this study it became apparent that, in particular for the coupled complex Ginzburg-Landau equations, many questions are open. Even the most simplest states in these coupled amplitude equations deserve a more thorough investigation. For instance, even in homogeneous systems, spatially periodic states (as can be seen in figures 3-9 and 3-11) occur quite generally when the cross-coupling coefficient is sufficiently large. Although some work has been carried out [59], the dynamics of such states is poorly understood.

In a single homogeneous CGLE, the group-velocity term can be transformed away, but in coupled equations this is no longer true. Since the group-velocity terms are generally of lower order in ε than the other terms in the amplitude equations, their importance can be enormous. This question is related to more general questions about the validity of amplitude equations, as discussed at the end of chapter 1. A question that we intend

to study in the near future, concerns the states that connect patches of left- and right-traveling waves in coupled CGLE's. These states seem to be poorly understood, and non-adiabatic effects, i.e., mixing of the slow and fast scales seem to play a role here [36].

In chapter 4 we described the interactions between pulses and fronts in a particular, symmetry broken single complex Ginzburg-Landau equation. In this system we could describe a complicated dynamical state in terms of simpler coherent structures. These structures seem to occur also in more general states, and an important issue is understanding if and how the local structures can be used as building blocks from which the dynamics of more complicated states can be understood. This question is particularly interesting in the study of spatio-temporal chaos. Since describing all the details of such disordered states is not feasible, a major goal in the study of spatio-temporal chaos is obtaining a statistical theory for the large scale behavior. An intuitively appealing route to obtain such a description is using the local (coherent) structures as the fundamental entities of a statistical theory. In such a way we may extract from the infinite number of degrees of freedom of a spatially extended system, only the ones that carry relevant information. Although attempts to obtain statistics along this line of reasoning have been made [70], no systematic knowledge of the properties of such reduced descriptions is available. The validity of reduced descriptions in the context of spatio-temporal chaos will be central to the research that I will pursue as a post-doc in the near future.

References

- [1] H. Nishimori and N. Ouchi, *Phys. Rev. Lett.* **71**, 197 (1993).
- [2] O. L. Sivashinsky, *Annu. Rev. Fluid Mech.* **15**, 179 (1983).
- [3] S. Chandrasekhar, *Hydrodynamic and Hydromagnetic Stability*, Clarendon Press, Oxford (1961).
- [4] M. C. Cross and P. C. Hohenberg, *Rev. Mod. Phys.* **65**, 851 (1993).
- [5] D. Bensimon, B. I. Shraiman and V. Croquette, *Phys. Rev. A* **38**, 5461 (1988).
- [6] T. Passot and A. C. Newell, *Physica D* **74**, 301 (1994); P. Manneville, *Dissipative structures and weak turbulence*, Academic Press, New York (1990); Y. Kuramoto, *Chemical oscillations, waves and turbulence*, Springer, Berlin (1984); P. Collet and J. P. Eckmann, *Instabilities and fronts in extended systems*, Princeton university press, Princeton (1990).
- [7] A. C. Newell and J. A. Whitehead, *J. Fluid Mech.* **38**, 279 (1969).
- [8] P. Manneville, *J. Phys. (Paris)* **44**, 563 (1983).
- [9] Y. Tu and M. C. Cross, *Phys. Rev. Lett.* **69**, 2515 (1992).
- [10] E. Bosch and W. van de Water, *Phys. Rev. Lett.* **70**, 3420 (1993); T. Bohr, E. Bosch and W. van de Water, *Nature* **372**, 48 (1994); H. Chaté, *Physica D* **86**, 238 (1995); H. Chaté and P. Manneville, *Physica A* **224**, 348 (1995); D. A. Egolf and H. S. Greenside, *Phys. Rev. Lett.* **74**, 1751 (1995).
- [11] W. van Saarloos and P. C. Hohenberg, *Physica D* **56**, 303 (1992); **69**, 209 (1993) [Errata].
- [12] P. G. Daniels and C. F. Ong, *J. Fluid Mech.* **215**, 503 (1990).
- [13] M. Schnaubelt and F. H. Busse in *Nonlinear evolution of spatio-temporal structures in dissipative continuous systems*, Plenum Press, New York (1990).
- [14] J. B. Swift and P. C. Hohenberg, *Phys. Rev. A* **15**, 319 (1977).
- [15] J. D. Crawford, *Rev. Mod. Phys.* **63**, 991 (1991); D. K. Arrowsmith and C. M. Place, *An introduction to Dynamical Systems*, Cambridge University Press, Oxford (1990).
- [16] G. C. Paquette, L.-Y. Chen, N. Goldenfeld and Y. Oono, *Phys. Rev. Lett.* **72**, 76 (1994); G. C. Paquette and Y. Oono, *Phys. Rev. E* **49**, 2368 (1994).

- [17] V. L. Ginzburg and L. D. Landau, *Zh. Eksp. Teor. Fiz.* **20**, 1064 (1950).
- [18] M. W. Hirsch and S. Smale, *Differential equations, dynamical systems and linear algebra*, Academic Press, New York (1974).
- [19] R. Montagne, E. Hernández-García and M. San Miguel, to appear in *Physica D*.
- [20] R. Graham and T. Tél, *Europhys. Lett.* **13**, 715 (1990).
- [21] A. C. Newell, *Rocky Mountain J. Math.* **8**, 25 (1978); Y. S. Kivshar and B. A. Malomed, *Rev. Mod. Phys.* **61**, 763 (1989).
- [22] S. Fauve and O. Thual, *Phys. Rev. Lett.* **64**, 282 (1990).
- [23] T. B. Benjamin and J. E. Feir, *J. Fluid Mech.* **27**, 417 (1967); J. T. Stuart and R. C. DiPrima, *Proc. Roy. Soc. Lond. a* **362**, 27 (1978).
- [24] W. Eckhaus, *Nonlinear Stability Theory*. Springer-Verlag, Berlin (1965).
- [25] L. Kramer and A. Baratoff, *Phys. Rev. Lett.* **38**, 518 (1977); L. Kramer and R. Rangel, *J. Low temp. Phys.* **57**, 391 (1984).
- [26] P. Marcq, H. Chaté and R. Conte, *Physica D* **73**, 305 (1994).
- [27] P. Coullet, A. T. Frisch and F. Plaza, *Physica D* **62**, 75 (1993).
- [28] E. Ben-Jacob, H. R. Brand, G. Dee, L. Kramer and J. S. Langer, *Physica D* **14**, 348 (1985).
- [29] W. van Saarloos, *Phys. Rev. A* **37**; 211 (1988); **39**, 6367 (1989).
- [30] B. I. Shraiman, A. Pumir, W. van Saarloos, P. C. Hohenberg, H. Chaté and M. Hohenberg, *Physica D* **57**, 241 (1992).
- [31] N. Bekki and K. Nozaki, *Phys. Lett. A* **110**, 133 (1985).
- [32] S. Popp, O. Stiller, I. Aranson, A. Weber and L. Kramer, *Phys. Rev. Lett.* **70**, 3880 (1993).
- [33] J. Lega, B. Janiaud, S. Jucquois and V. Croquette, *Phys. Rev. A* **45**, 5595 (1992).
- [34] W. Eckhaus, *ICIAM 91: Proc. 2nd Int. Conf. Ind. Appl. Math.* (R.E. O'Malley ed.) 83-98 (1992); W. Eckhaus, *J. Nonlinear Sci.* **3** 329-348 (1993).
- [35] H. Riecke, *Phys. Rev. Lett.* **68**, 301 (1992); *Physica D* **61**, 253 (1992); H. Herrero and H. Riecke, *Physica D*, in print.
- [36] R. Alvarez, private communication.
- [37] F. Zhong, R. Ecke and V. Steinberg, *Phys. Rev. Lett.* **67**, 2473 (1991).

- [38] L. Ning and R. E. Ecke, *Phys. Rev. E* **47**, 3326 (1993).
- [39] R. Heinrichs, G. Ahlers, and D. S. Cannell, *Phys. Rev. A* **35**, 2761 (1987); E. Moses, J. Fineberg, and V. Steinberg, *Phys. Rev. A* **35**, 2757 (1987); P. Kolodner, D. Bensimon and C. M. Surko, *Phys. Rev. Lett.* **60**, 1723 (1988).
- [40] E. Y. Kuo and M. C. Cross, *Phys. Rev. E* **47**, 2245 (1993).
- [41] W. Schöpf and W. Zimmerman, *Phys. Rev. E* **47**, 1739 (1993).
- [42] R. E. Ecke, F. Zhong and E. Knobloch, *Europhys. Lett.* **19**, 177 (1992).
- [43] H. F. Goldstein, E. Knobloch, I. Mercader and M. Net, *J. Fluid Mech* **248**, 583 (1993); **262**, 293 (1994).
- [44] J. C. Buell and I. Catton, *Phys. Fluids* **26**, 892 (1983).
- [45] R. M. Clever and F. H. Busse, *J. Fluid Mech.* **198**, 345 (1981).
- [46] P. P. Niiler and F. E. Bisshopp, *J. Fluid Mech.* **22**, 753 (1965).
- [47] P. Kolodner, J. A. Glazier and H. Williams, *Phys. Rev. Lett.* **65**, 1579 (1990)
- [48] L. Kramer, E. Ben-Jacob and A. H. Brand, *Phys. Rev. Lett.* **49**, 1891 (1982); H. Riecke and A. H. G. Paap, *Europhys. Lett.* **14**, 433 (1991).
- [49] B. A. Malomed, *Phys. Rev. E* **47**, R2257 (1993).
- [50] B. A. Malomed, *Phys. Rev. E* **50**, 4249 (1994).
- [51] F. Busse, *Rep. Progr. Phys.* **41**, 1930 (1979).
- [52] V. S. Gertsberg and G. I. Sivashinsky, *Progr. Theor. Phys.* **66**, 1219 (1981).
- [53] B. A. Malomed, A. A. Nepomnyashchy, and M. I. Tribelsky, *Phys. Rev. A* **42**, 7244 (1990).
- [54] R. B. Hoyle, *Phys. Rev. E* **51**, 310 (1995).
- [55] P. Couillet, S. Fauve and E. Tirapegui, *J. Phys. (Paris) Lett.* **46**, L-787 (1985), and references therein.
- [56] B. A. Malomed, *Phys. Rev. E* **50**, R3310 (1994).
- [57] J. M. Chomaz, P. Huerre and L. G. Redekopp, *Phys. Rev. Lett.* **60**, 25 (1988).
- [58] G. T. Dee and W. van Saarloos, *Phys. Rev. Lett.* **60**, 2641 (1988).
- [59] H. Sakaguchi, "Localized solutions to the coupled complex Ginzburg-Landau equations", preprint (1995).

- [60] P. Kolodner, Phys. Rev. A **44**, 6448 (1991).
- [61] J. J. Niemela, G. Ahlers and D. S. Cannel, Phys. Rev. Lett. **64**, 1365 (1990).
- [62] P. Kolodner, Phys. Rev. Lett. **66**, 1165 (1991).
- [63] J. A. Glazier and P. Kolodner, Phys. Rev. A **43**, 4269 (1991).
- [64] P. Kolodner, Phys. Rev. E **50**, 2731 (1994).
- [65] E. Kaplan, E. Kuznetsov and V. Steinberg, Europhys. Lett. **28**, 237 (1994).
- [66] O. Thual and S. Fauve, J. Phys. (Paris) **49**, 1829 (1988); B. A. Malomed, Physica D **29**, 155 (1987); C. Elphick and E. Meron, Phys. Rev. A **40**, 3226 (1989); Phys. Rev. Lett. **65**, 2476 (1990); V. Hakim, P. Jakobsen and Y. Pomeau, Europhys. Lett. **11**, 19 (1990); B. A. Malomed and A. A. Nepomnyashchy, Phys. Rev. A **42**, 6009 (1990).
- [67] W. Barten, M. Lücke, W. Hort and M. Kamps, Phys. Rev. Lett. **63**, 376 (1989).
- [68] W. van Saarloos, M. van Hecke and R. Holyst, Phys. Rev. E **52**, 1773 (1995).
- [69] R. J. Deissler and H. R. Brand, Phys. Rev. Lett. **72**, 478 (1994) and Phys. Rev. Lett. **74**, 4847 (1995).
- [70] M. Rost and J. Krug, Physica D **88**, 1 (1995).

Samenvatting

De natuur om ons heen vertoont een grote verscheidenheid aan patronen. Aan de ene kant bestaan er min of meer ordelijke patronen, zoals bijvoorbeeld watergolven in een rustige vijver en zandribbels op het strand, aan de andere kant zijn er zeer grillige patronen zoals zeegolven in de branding en het weersysteem op aarde. Het interessante aan deze patronen is dat, voor een bepaald systeem (denk bijvoorbeeld aan de zee met daarover blazende wind), ze in een enorme verscheidenheid kunnen optreden.

Dit proefschrift houdt zich bezig met een bepaald soort beschrijving, de zogenaamde *amplitude vergelijkingen*, voor patronen die bij benadering regelmatig (periodiek) zijn. In deze samenvatting zal allereerst, in zo eenvoudig mogelijke termen, de basisbegrippen uiteen worden gezet die ten grondslag liggen aan deze theorie. Vervolgens zal een beknopte samenvatting gegeven worden van de inhoud van de diverse hoofdstukken van dit proefschrift.

De natuurwetten die de verschijnselen in onze wereld beschrijven zijn relatief simpel in vergelijking met die verschijnselen zelf. Bijvoorbeeld, de wiskundige vergelijkingen die vloeistoffen zoals water beschrijven, zijn al meer dan een eeuw bekend onder de naam Navier-Stokes vergelijkingen. Betekent dit nu dat de natuurkunde voor vloeistof systemen af is? Geenszins! Het probleem is dat de *oplossingen* van de Navier-Stokes vergelijkingen in het algemeen niet te geven zijn, en dit heeft tot gevolg dat veel fenomenen die optreden in vloeistof stromingen niet goed begrepen zijn. De onmogelijkheid algemene oplossingen te vinden wordt in belangrijke mate veroorzaakt door de niet-lineariteiten in deze vergelijkingen.

Om te illustreren wat lineariteit en niet-lineariteit betekent zullen we nu een gedachten experiment uitvoeren. Stel u zich voor dat, van geringe hoogte, een klein steentje in een stilstaande plas water wordt gegooid. De kringvormige golven die ontstaan in het wateroppervlak komen overeen met simpele oplossingen van de vloeistof vergelijkingen. Als we deze oplossing eenmaal gevonden hebben, dan kunnen we ook berekenen wat er gebeurt als we een twee keer zo groot steentje in het water gooien: we vinden dan dezelfde kringvormige golf, maar twee keer zo sterk. Ook als we twee steentjes naast elkaar in het water gooien, is de resulterende oppervlakte golf simpel de som van twee kringvormige golven. Het feit dat we hier oplossingen kunnen construeren door diverse simpele oplossingen op te tellen, heet het superpositie beginsel, en dit is een essentieel kenmerk van lineaire systemen.

Echter, de vloeistof vergelijkingen zijn alleen maar (bij benadering) lineair als de vloeistof snelheden klein zijn, en als de vloeistof snelheid toeneemt, dan worden de niet-lineaire effecten belangrijker. In dat geval kunnen oplossingen niet zomaar bij elkaar opgeteld worden, en kan zich dus essentieel nieuwe gedrag voordoen. Om hier een idee van te krijgen, volstaat het een baksteen met een hoge snelheid in een plas water te gooien. De spetters die in het rond vliegen kunnen niet beschreven worden in termen van

de kleine (lineaire) golfjes, en zijn een gevolg van de niet-lineariteiten. Merk op, dat als de spetters weer terug in de vijver zijn gevallen, we wel degelijk weer een cirkelvormige golf waarnemen; dat aspect van de vloeistof stroming is redelijk te beschrijven met de lineaire versie van de vloeistof vergelijkingen.

Omdat het geven van algemene oplossingen van de Navier-Stokes vergelijkingen (of van andere in de natuurkunde voorkomende systemen) een hopeloze taak is, heeft men allerlei manieren bedacht om toch, vanuit de vloeistof vergelijkingen, te komen tot *effectieve* theorieën die een deel van de experimenteel waargenomen verschijnselen kunnen beschrijven en verklaren. In dit proefschrift zullen we ons bezighouden met zo'n theorie die bij benadering periodieke patronen waarbij de niet-lineariteiten relatief zwak zijn, beschrijven.

We zullen dit illustreren aan de hand van het experimentele systeem dat een zeer belangrijke rol speelt in dit proefschrift: Rayleigh-Bénard convectie. Men neme een aan bovenzijde gekoelde en afgesloten container die we geheel vullen met een vloeistof, en deze plaatsen we op een verhittings element. Als we de onderzijde van de vloeistof niet verhitten, dan gebeurt er natuurlijk niets, maar als we de verhitting aanzetten, dan zal, analoog aan een pan water op een vuurtje, de vloeistof in beweging komen. Dit roept natuurlijk meteen een aantal vragen op. Waarom beweegt de vloeistof? Hoe groot moet het temperatuur-verschil tussen de onder en bovenkant van het bakje zijn voor dat de vloeistof gaat bewegen? In wat voor patroon beweegt de vloeistof? Hoe hangt dit patroon af van het eerder genoemde temperatuur-verschil?

De eerste van deze vragen kan als volgt beantwoord worden: Als vloeistof verwarmd wordt zet zij uit. Dat betekent, dat warme vloeistof lichter is dan zware vloeistof, en in het bovenstaand experiment hebben we dus de situatie dat relatief zware, koude vloeistof bovenop relatief lichte vloeistof ligt. Ten gevolge van de zwaartekracht wordt de zware vloeistof naar beneden getrokken. Ten gevolge van de wrijving (viscositeit) kan de vloeistof in rust blijven, maar als het temperatuur-verschil maar groot genoeg is, wordt de stationaire toestand instabiel, en komt de vloeistof in beweging. Dit wordt convectie genoemd. Aangezien op een bepaalde plaats de koude vloeistof niet naar beneden kan bewegen terwijl de lichte vloeistof naar boven beweegt, ontstaat er een *patroon* waarin de vloeistof beweegt. In het allersimpelste geval beweegt de vloeistof zich in regelmatige rollen, zoals gellustreerd in figuur 1-1. Het temperatuur-verschil tussen de onder- en bovenplaat waarbij deze rollen ontstaan kan succesvol worden berekend uit de vloeistof vergelijkingen, evenals de grootte van de rollen bij dit kritieke temperatuur-verschil. Hier gebruiken we dat de vloeistof snelheid heel klein is bij het kritieke temperatuur-verschil, zodat we de niet-lineaire termen kunnen verwaarlozen.

Als het temperatuur-verschil verhoogd wordt, dan neemt men experimenteel waar dat de rollen vervormd worden en meer en meer grillige patronen ontstaan. Voor voldoende sterke verhitting, worden de rollen zelfs helemaal vernietigd, en krijgen we een soort turbulente stroming. Dit zijn typisch de patronen die men waarneemt als men een pan water aan de kook brengt; het is nog behoorlijk lastig om de verhitting precies zo af te stellen dat zich een regelmatig patroon vormt.

Voor meer algemene systemen vinden we een soortgelijk gedrag: Als een homogeen,

ruimtelijk uitgebreid systeem uit evenwicht gebracht wordt (zoals door verhitting in het convectie experiment), ontstaan er patronen. De eerste patronen die waargenomen worden zijn periodiek in ruimte en/of tijd. Wordt het systeem verder uit evenwicht gebracht, dan gaan de niet-lineariteiten een rol spelen en wordt het periodieke basispatroon vervormd.

De amplitude vergelijkingen kunnen, uitgaande van het regelmatig patroon, kleine en langzame veranderingen in dit patroon beschrijven. In dit geval zijn dat de patronen die ontstaan als het temperatuur-verschil net boven de kritieke waarde ligt. Het komt er op neer dat we het regime beschouwen waar de niet-lineariteiten zwak maar niet verwaarloosbaar zijn.

Het kan worden aangetoond dat in dit regime de veranderingen van het periodieke patroon langzaam, en over grote afstanden plaatsvinden. Er zijn dus in feite twee schalen van belang; de snelle schaal van het regelmatige basispatroon dat uit de gelineariseerde vergelijkingen volgt, en de langzame schaal waarop het basispatroon vervormd wordt. De wiskundige afleiding van de amplitude vergelijkingen weerspiegelt dat ook. We schrijven het patroon als het produkt van een regelmatig (periodiek) patroon (zoals bijvoorbeeld de rollen) en een amplitude functie, die langzaam varieert. Uit de onderliggende bewegings vergelijkingen (bijvoorbeeld de Navier-Stokes vergelijkingen), leiden we dan een bewegings vergelijking voor de amplitude af, en dit is dan de amplitude vergelijking.

Het mooie van deze amplitude vergelijkingen is dat in natuurkundig zeer diverse systemen, dezelfde amplitude vergelijkingen optreden; in die zin geven de amplitude vergelijkingen een universele beschrijving van ruimtelijke systemen uit evenwicht.

Er zijn slechts een beperkt aantal universele modellen dicht bij de eerste vorming van patronen. Welke van deze amplitude vergelijking er optreedt wordt alleen bepaald door het soort periodiciteit; in het proefschrift concentreren we ons op basispatronen die zowel periodiek in ruimte als in de tijd zijn; de amplitude vergelijking is dan de *complex Ginzburg-Landau vergelijking*.

Opgemerkt dient te worden, dat deze vergelijking nog enige coëfficiënten bevat die afgeleid kunnen worden uit de onderliggende fysische wetten. Echter, de amplitude vergelijking is veel simpeler dan de volle bewegings vergelijkingen; de prijs die men betaalt is dat alleen zwak niet-lineaire patronen kunnen worden beschreven. De meest opmerkelijke eigenschap van de complexe Ginzburg-Landau vergelijking is dat, als een functie van de coëfficiënten, zowel ordelijke als wanordelijke patronen kunnen optreden. Dit wanordelijke gedrag wordt aangeduid met de term *spatio-temporele chaos*, en beschrijft een zwak soort turbulentie van de patronen. Voorbeelden van spatio-temporele chaos zijn te zien in figuren 1-7, 1-8 en 3-11.

Hoofdstuk 1 geeft een uitgebreide inleiding in het gebruik van amplitude vergelijkingen. De techniek voor het afleiden van zo'n vergelijking komt aan de orde, en voor een simpel model systeem, de zogenaamde Swift-Hohenberg vergelijking, leiden we de amplitude vergelijking daadwerkelijk af. We bediscussiëren enige simpele oplossingen van de amplitude vergelijkingen en hun stabiliteit. Vervolgens geven we voorbeelden van de spatio-temporele chaos zoals die voorkomt in de complexe Ginzburg-Landau vergelijking. We eindigen dit hoofdstuk met een discussie van de geldigheid van de amplitude vergelijkingen.

In hoofdstuk 2 leiden we de amplitude vergelijkingen af voor een Rayleigh-Bénard convectie systeem in een roterende ring. In het bijzonder berekenen we de coëfficiënten van de gekoppelde complexe Ginzburg-Landau vergelijkingen als functie van de systeem parameters. We vinden dat voor een juist gekozen vloeistof (met een ratio van temperatuurdiffusie en viscositeit van ongeveer 0.15), de rotatie snelheid van de ring gebruikt kan worden om de coëfficiënten van de amplitude vergelijking te veranderen over een groot gebied. In het bijzonder voorspellen we dat de rotatie snelheid kan bepalen of er ordelijke dan wel chaotische patronen optreden. Opgemerkt dient te worden dat er niet veel systemen zijn waarvoor de coëfficiënten van de amplitude vergelijkingen echt zijn uitgerekend als functie van fysische parameters. Voorzover ons bekend is er geen enkel ander systeem waar de coëfficiënten zo eenvoudig over een zo groot gebied kunnen worden veranderd.

In hoofdstuk 3 spelen de amplitude vergelijkingen meer de rol van een "toy model", dat wil zeggen, we bekommeren ons hier niet zozeer om hun fysische rechtvaardiging, maar bestuderen een puur theoretische vraag. Wat gebeurt er als we door middel van een inhomogeniteit in de koppelings term van twee gekoppelde amplitude vergelijkingen twee kwalitatief verschillende oplossingen naast elkaar hebben? We vinden dat een dergelijke oplossing niet kan bestaan boven een zekere waarde van de groepssnelheid (een van de coëfficiënten van de amplitude vergelijkingen), en bestuderen de dynamische toestanden die dan ontstaan.

In hoofdstuk 4 bestuderen we het gedrag van puls-vormige oplossingen van de complexe Ginzburg-Landau vergelijkingen als de links-rechts symmetrie gebroken is. Hierdoor gaan de pulsen bewegen met een snelheid die afwijkt van de groepssnelheid, precies zoals is waargenomen in convectie experimenten in vloeistof mengsels. In deze experimenten blijken de pulsen te blijven bestaan terwijl ze bewegen in een instabiele achtergrond toestand. We verifiëren dat dit ook het geval is in ons model. Als de achtergrond toestand meer instabiel wordt gemaakt, dan ontstaat er een interessante dynamische toestand, waar de pulsbeving onregelmatig wordt. We tonen aan dat dit te maken heeft met de propagatie van zogenaamde fronten, en dat, voor een bepaald parameter regime, de gemiddelde snelheid van de onregelmatig voortbewegende puls gelijk is aan die van het front.

List of publications

This thesis was based on the following papers:

- M. van Hecke, P. C. Hohenberg and W. van Saarloos, *Amplitude equations for pattern forming systems*, in *Fundamental problems in statistical mechanics VIII*, edited by H. van Beijeren and M. H. Ernst, Elsevier (1994).
(chapter 1).
- M. van Hecke, E. de Wit and W. van Saarloos, *Coherent and incoherent drifting pulse dynamics in a complex Ginzburg-Landau equation*, Phys. Rev. Lett. **75**, 3830 (1995).
(chapter 4).
- M. van Hecke and B. Malomed, *A domain wall between single-mode and bimodal states and its transition to dynamical behavior in inhomogeneous systems*, submitted to Physica D.
(chapter 3).
- M. van Hecke and W. van Saarloos *Rayleigh-Bénard convection in a rotating annulus*, in preparation.
(chapter 2).

Other papers to which the author has contributed:

- M. van Hecke, W. van Saarloos and P. C. Hohenberg, *Comment on "Absolute and convective instabilities in nonlinear systems"*, Phys. Rev. Lett. **71**, 2162 (1993).
- W. van Saarloos, M. van Hecke and R. Holyst, *Front Propagation into unstable and metastable states in smectic-C* liquid crystals: Linear and nonlinear marginal-stability analysis*, Phys. Rev. E **52**, 1773 (1995).

[The following text is extremely faint and illegible, appearing to be a list of references or a table of contents.]

Curriculum Vitae

Op 18 juni 1967 ben ik geboren te Amsterdam. In 1985 heb ik mijn VWO diploma gehaald aan het St. Nicolaas Lyceum te Amsterdam. Daarna heb ik van 1985 tot 1992 natuurkunde gestudeerd aan de Universiteit van Amsterdam, alwaar ik in april 1992 ben afgestudeerd (met lof) in de theoretische natuurkunde op een scriptie over tijdomkeer symmetrieën.

In september 1992 ben ik als assistent in opleiding aangesteld aan het Instituut-Lorentz voor theoretische natuurkunde. Ik heb geassisteerd bij het geven van het werkcollege 'Statistische Fysica' en bij het geven van diverse demonstratie-colleges over niet-lineaire dynamica; ook heb ik een scriptie-student meebegeleid. In het najaar van 1993 bezocht ik de Universiteit van Bayreuth, alwaar ik met prof.dr. L. Kramer en dr. I. Aranson heb gewerkt aan de beweging van spiralen in de twee-dimensionele complexe Ginzburg-Landau vergelijking. Uiteraard bezocht ik diverse cursussen en zomerscholen.

Het tijdens de afgelopen 4 jaar gedane onderzoek is beschreven in dit proefschrift. Vanaf 1 oktober 1996 zal ik, gefinancierd door de NWO, voor een periode van een jaar als postdoc verbonden zijn aan het Niels Bohr Instituut te Kopenhagen.

Stellingen behorende bij

THE AMPLITUDE DESCRIPTION OF NONEQUILIBRIUM PATTERNS

Martin van Hecke

1. Rayleigh-Bénard convectie in een roterende annulus geeft, voor een juiste keus van de convectievloeistof, een experimentele realisatie van de cubische complexe Ginzburg-Landau vergelijking, waarbij de rotatiesnelheid bepaalt of zich ordelijke danwel deterministisch chaotische patronen zullen vormen.

Dit proefschrift, hoofdstuk 2.

2. In quintische Ginzburg-Landau modellen met gebroken reflectie symmetrie, wordt de propagatie van pulsen onregelmatig zodra zich fronten vormen die sneller bewegen dan de pulsen.

Dit proefschrift, hoofdstuk 4.

3. Dat de oscillerende pulsen in de quintische Ginzburg-Landau vergelijking zijn gerelateerd aan niet-lineaire fronten, blijkt onder meer uit hun gebied van existentie in de parameter ruimte, dat dicht ligt bij de curve waar de niet-lineaire frontsnelheid nul is.

R. J. Deissler en H. R. Brand, Phys. Rev. Lett. 72, 478 (1994).

4. Het gebruikelijke argument voor het zogenaamde lineaire-marginale-stabiliteits-criterium voor frontpropagatie, verduistert de essentiële maar grotendeels onbekende rol die de niet-lineariteiten spelen in de selectie van de frontsnelheid.

W. van Saarloos, Phys. Rev. A 39, 6367 (1989).

5. Om de dynamica van locale structuren in dissipatieve spatio-temporele chaotische of turbulente toestanden te begrijpen, is de kennis van de interactie van enkele geïsoleerde locale structuren volstrekt onvoldoende.

6. De door Gunaratne *et. al* voorgestelde differentiaaloperator die een maat voor de wanorde in twee-dimensionele patronen zou zijn, is niets anders dan de Laplaciaan in vermomming.

*G. H. Gunaratne, R. E. Jones, Q. Ouyang and H. L. Swinney,
Phys. Rev. Lett. 75, 3281 (1995).*

7. De experimenteel waargenomen propagatiesnelheid van coherente structuren tussen links- en rechtslopende golven, kan niet beschreven worden door amplitude-vergelijkingen, aangezien golfgetal en frequentie van het onderliggende patroon de snelheid van deze structuren bepalen.

*M. Dubois, F. Daviaud, O. Ronsin and P. Berge,
Physica D 61, 140 (1992).*

R. Alvarez, private communications.

8. Om de sneller dan lineaire groei van oppervlaktestructuren in coarsening-experimenten te begrijpen, zal men de interactie tussen bulk- en oppervlaktestructuur beter moeten doorgronden.

*A. Cumming, P. Wiltzius, F. S. Bates en J. H. Rosedale,
Phys. Rev. A 45, 885 (1992).*

9. Het goede geluid van oude analoge synthesizers in vergelijking met dat van moderne digitale synthesizers is een gevolg van de niet-lineariteiten van de eerstgenoemde soort.

10. Zonder turbulentie geen spraak.

Martin van Hecke
3 september 1996